



ISSN 1028-8546

Volume XXI, Number 4

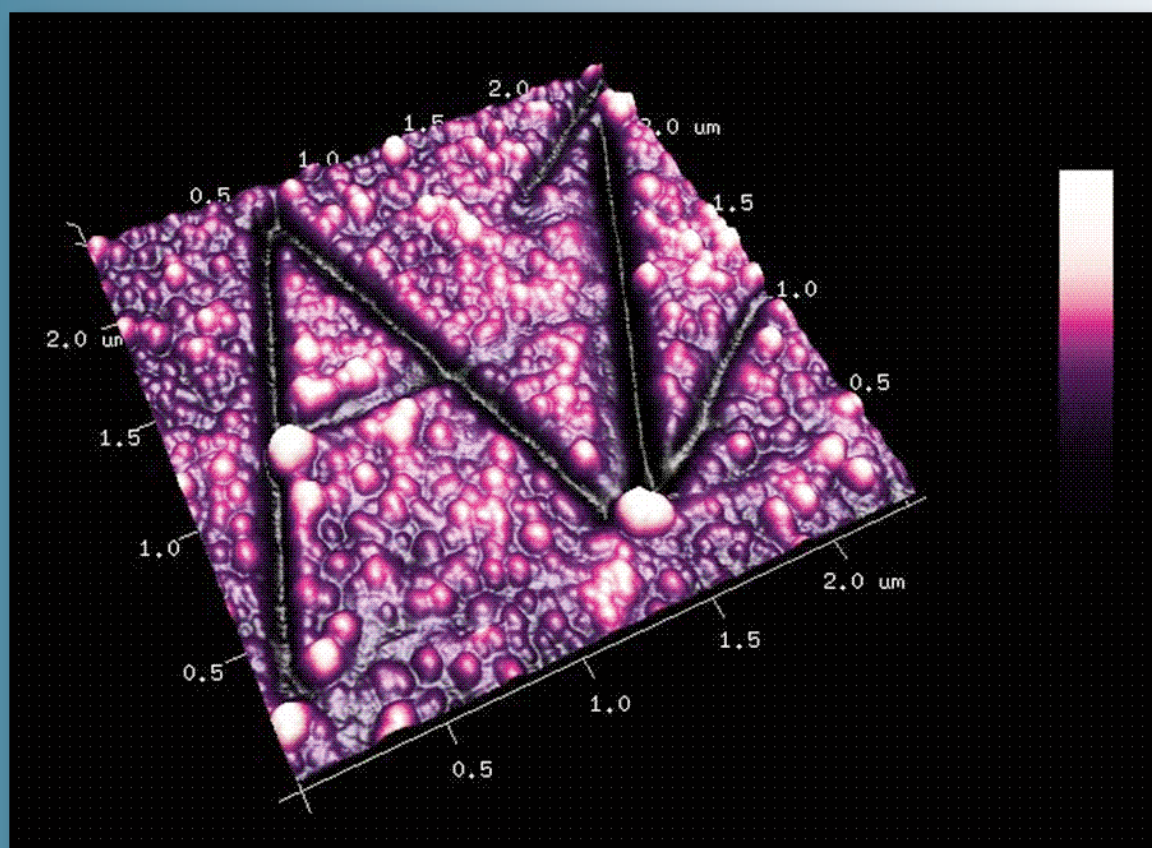
Section: En

December, 2015

# Azerbaijan Journal of Physics

# Fizika

[www.physics.gov.az](http://www.physics.gov.az)



G.M. Abdullayev Institute of Physics  
Azerbaijan National Academy of Sciences  
Department of Physical, Mathematical and Technical Sciences

Published from 1995  
Ministry of Press and Information  
of Azerbaijan Republic,  
Registration number 402, 16.04.1997

**ISSN 1028-8546**  
vol. XXI, Number 04, 2015  
Series: En

## *Azerbaijan Journal of Physics*

# *FIZIKA*

*G.M.Abdullayev Institute of Physics  
Azerbaijan National Academy of Sciences  
Department of Physical, Mathematical and Technical Sciences*

### **HONORARY EDITORS**

Arif PASHAYEV

### **EDITORS-IN-CHIEF**

Nazim MAMEDOV

Chingiz QAJAR

### **SENIOR EDITOR**

Talat MEHDIYEV

### **INTERNATIONAL REVIEW BOARD**

Ivan Scherbakov, Russia  
Kerim Allahverdiyev, Azerbaijan  
Mehmet Öndr Yetiş, Turkey  
Gennadii Jablonskii, Buelorussia  
Rafael Imamov, Russia  
Vladimir Man'ko, Russia  
Eldar Salayev, Azerbaijan  
Dieter Hochheimer, USA  
Victor L'vov, Israel  
Vyacheslav Tuzlukov, South Korea

Majid Ebrahim-Zadeh, Spain  
Firudin Hashimzadeh, Azerbaijan  
Anatoly Boreysho, Russia  
Mikhail Khalin, Russia  
Hasan Bidadi, Tebriz, East Azerbaijan, Iran  
Natiq Atakishiyev, Mexico  
Maksud Aliyev, Azerbaijan  
Arif Hashimov, Azerbaijan  
Javad Abidinov, Azerbaijan  
Bagadur Tagiyev, Azerbaijan

Tayar Djafarov, Azerbaijan  
Talat Mehdiyev, Azerbaijan  
Vali Huseynov, Azerbaijan  
Ayaz Baramov, Azerbaijan  
Tofiq Mammadov, Azerbaijan  
Salima Mehdiyeva, Azerbaijan  
Shakir Nagiyev, Azerbaijan  
Rauf Guseynov, Azerbaijan  
Almuk Abbasov, Azerbaijan  
Yusif Asadov, Azerbaijan

### **TECHNICAL EDITORIAL BOARD**

Senior secretary Elmira Akhundova, Nazli Guseynova, Sakina Aliyeva,  
Nigar Akhundova, Elshana Aleskerova, Rena Nayimbayeva

### **PUBLISHING OFFICE**

131 H.Javid ave, AZ-1143, Baku  
ANAS, G.M.Abdullayev Institute of Physics

Tel.: (99412) 539-51-63, 539-32-23  
Fax: (99412) 447-04-56  
E-mail: [jophphysics@gmail.com](mailto:jophphysics@gmail.com)  
Internet: [www.physics.gov.az](http://www.physics.gov.az)

It is authorized for printing:

Published at "SƏRQ-QƏRB"  
17 Ashug Alesger str., Baku  
Typographer : Aziz Gulaliyev

Sent for printing on: \_\_\_\_\_. 201\_  
Printing approved on: \_\_\_\_\_. 201\_  
Physical binding: \_\_\_\_\_  
Number of copies: \_\_\_\_\_ 200  
Order: \_\_\_\_\_

## POLARIZATION PROPERTIES OF $\text{TlGaSe}_2$ LAYERED SEMICONDUCTOR ORIGINATED FROM ELECTRICALLY ACTIVE NATIVE DEEP LEVEL DEFECTS

**MIRHASAN Yu. SEYIDOV<sup>1,2,\*</sup>, FAIK A. MIKAILZADE<sup>1,2</sup>, TALIP UZUN<sup>1</sup>,  
ANDREI P. ODRINSKY<sup>3</sup>, VAFA B. ALIYEVA<sup>2</sup>, TOFIG G. MAMMADOV<sup>2</sup>,  
SARDAR S. BABAYEV<sup>2</sup>**

<sup>1</sup> *Department of Physics, Gebze Technical University, 41400, Gebze, Kocaeli, Turkey*

<sup>2</sup> *Institute of Physics, Azerbaijan National Academy of Sciences, G. Javid av., 131,  
Baku, AZ – 1143, Azerbaijan*

<sup>3</sup> *Institute of Technical Acoustics, National Academy of Sciences of Belarus, Lyudnikov av. 13,  
Vitebsk 210717, Belarus*

*\*Corresponding author. Address: Department of Physics, Gebze Institute of Technology,  
Gebze, 41400, Kocaeli, Turkey. Tel.: +90 262 605 1329; Fax: +90 262 653 8490*

Parameters of electrically active native defect centers in  $\text{TlGaSe}_2$  layered semiconductor were investigated by means of the photo-induced current transient spectroscopy (PICTS). We found six deep defect energy levels in the band gap of  $\text{TlGaSe}_2$ . These deep level traps localize both in the bulk of crystal and on the its surface and can be electrically charged. It has been shown that charged deep defects can be the cause of the electret behavior of  $\text{TlGaSe}_2$ .

Pyroelectric current measurements were applied to provide information on the internal electric fields occurred in the bulk and near-surface layer of  $\text{TlGaSe}_2$  single crystal and reveal the nature of the positive and negative contributions to the pyroelectric response of the pre-polarized  $\text{TlGaSe}_2$ . It was shown that positive pyroelectric signal from  $\text{TlGaSe}_2$  was mainly determined by electrostatic field on the surface layer of sample poled near incommensurate phase above the Curie phase transition temperature; whereas negative pyroelectric response of  $\text{TlGaSe}_2$  was mainly originated from the internal electric fields focused in the bulk of crystal after crystal poling in paraelectric phase at cooling from 300 to ~ 130 K. Discussed the possible origin of internal surface and bulk static electric field in  $\text{TlGaSe}_2$  attributed to bulk and near – surface localized native deep level defects.

The photovoltaic properties of the layered ferroelectric - semiconductor  $\text{TlGaSe}_2$  near the edge absorption region for different contacts positions relative to illumination geometries have been measured in the low temperature range. Obtained results suggest the presence of native thin insulator layer at the surface of  $\text{TlGaSe}_2$  crystal.

**Keywords:** photo - induced current transient spectroscopy, layered ferroelectric – semiconductor, deep levels.

**PACS:** 71.55. Ht, 72.20.Jv, 72.80.Jc, 74.62.Dh, 79.10.-n

### 1. INTRODUCTION

The ternary layered chalcogenide  $\text{TlGaSe}_2$  is an important semiconducting material of the  $A^{\text{III}}B^{\text{III}}C_2^{\text{VI}}$  family. According to publications [1, 2], it has direct and indirect band gaps to vary from 1.83 to 2.13 eV and from 2.00 to 2.23 eV, respectively at 300 K for samples from different technological batches with a high photoconductivity in the visible light region. Nominally undoped  $\text{TlGaSe}_2$  usually reveals  $p$  - type conductivity and are characterized by high resistance.

Native or intrinsic defects in  $\text{TlGaSe}_2$  layered semiconductor are imperfections in the crystal lattice of  $\text{TlGaSe}_2$  that involve only the constituent elements. Native defects in  $\text{TlGaSe}_2$  are known to introduce deep acceptor levels [3]. Native defects can profoundly alter the electronic structure near the band gap and control the electronic and optical properties of  $\text{TlGaSe}_2$  layered semiconductor. Hence, it is very important to understand the kind, the concentration and the electronic parameters of native deep level centers in  $\text{TlGaSe}_2$  for its successful applications in optoelectronic devices. Experimental studies of electronic transport properties of  $\text{TlGaSe}_2$  semiconductor have demonstrated that  $\text{TlGaSe}_2$  is strongly compensated semiconductor in which there is a self - compensation of shallow donors by intrinsic deep - level defects states [4]. That is a reason why  $\text{TlGaSe}_2$  layered semiconductor has a high resistance.

Unlike shallow impurity levels, which control the magnitude and type of conductivity of semiconductors, deep level defects primarily control the charge - carrier life – time. Since transport and optical properties of  $\text{TlGaSe}_2$  are dominantly determined by thermally ionized deep acceptor defects, the influence of shallow defects becomes negligible. Most semiconductor materials have charge trapped on their surface at equilibrium conditions in the dark. Defects at a semiconductor surface can affect the electrical and optical properties of the surface through Fermi level pinning, band bending and carrier recombination. If surface defects have voltage - dependent characteristics they are charged under external bias electric field influence. The surface charge gives rise to the near - surface built - up electric field, which results in a near - surface space charge region. Visualization of the electrostatic effects induced from the surface charged defects using conventional experimental techniques have limits. In this paper we provide a simple method for the surface charged defects monitoring for the first time.

$\text{TlGaSe}_2$  exhibits various types of cooperative electric dipole effects [5-8].  $\text{TlGaSe}_2$  is an improper uniaxial ferroelectric that undergoes the following successive phase transitions: from a paraelectric phase to the intermediate incommensurate phase (the ICN - phase) at  $T_i \sim 120$  K and from the ICN phase to the ferroelectric commensurate (C) phase at the Curie transition temperature,  $T_c \sim 107$  K. The paraelectric phase belongs to the monoclinic space group  $C_{2h}^6$ . The commensurate

phase is characterized by coexistence of ferroelectric and a semiconductor property with spontaneous polarization is along the monoclinic  $b$  axis.

TlGaSe<sub>2</sub> can be considered as an example of native quasi-two-dimensionality material with low density dangling bonds on cleaved surfaces and minimal surface roughness. The absence of free unsaturated electron bonds on the cleavage surface allows obtaining high - quality cleavage surfaces as compared with other semiconductor materials.

Recent studies have shown that TlGaSe<sub>2</sub> undergoes a temperature - induced phase transition near the surfaces at temperatures slightly higher than in the bulk. Surface phase transition in the TlGaSe<sub>2</sub> takes place at  $\sim 135$  K and is accompanied by changing of the surface electrical conductivity and permittivity [9 - 11]. This surface phase transition affects also the optical properties of crystal, giving rise to IR reflectance spectra of TlGaSe<sub>2</sub> [12].

The aim of this work is to study these defects and to determine their influence on the pyroelectric properties of TlGaSe<sub>2</sub>. In this scope, we used Photo - Induced Current Transient Spectroscopy (PICTS) technique. This method allows to determine the microscopic electrical properties of the defects that are the thermal ionization energy and capture cross - section.

Electrical polarization or electrets state from voltage - induced charging of the native deep level defects in TlGaSe<sub>2</sub> which act as the source of permanent internal electric field due to the charge storing properties preserves inside TlGaSe<sub>2</sub> for a long time. To investigate the internal electric fields from voltage - induced charged native deep level defects in TlGaSe<sub>2</sub> pyroelectric current measurements in TlGaSe<sub>2</sub> were utilized. It was found that the electrostatic charging of deep level defects in TlGaSe<sub>2</sub> by applying a potential difference between sample electrodes may be simply investigated from pyroelectric current measurements.

In this paper also, the photovoltaic spectrum of layered TlGaSe<sub>2</sub> was analyzed in two geometries: front and back. In the first case Au contacts replace on the illuminated surface, in the second case - on the opposite surface. Our experimental results predicate that TlGaSe<sub>2</sub> ferroelectric - semiconductor is an inhomogeneous ferroelectric - semiconductor with native thin insulator (dielectric) layer.

## 2. EXPERIMENTAL PROCEDURE

The starting polycrystalline materials were synthesized from elements Tl, Ga and Se of 5 N purity in conical quartz ampoules. The ampoules were charged with quantities of Tl, Ga and Se in the ratio corresponding to the stoichiometry. The charged ampoules were then evacuated to a pressure of  $10^{-3}$  Pa and sealed. The synthesis was carried out in a horizontal furnace at a temperature of 1073 K for 48 h.

Single crystal of TlGaSe<sub>2</sub> was grown by the modified Bridgman method. The samples for the measurements were taken from the middle part of the ingots. Ingots were cleaved perpendicular to the  $c$  - axis using a fine blade, no further polishing and cleaning treatments were required. The electrical resistivity of the ingot was measured to be around  $10^5 \Omega \text{ cm}$  at room temperature. The investigated TlGaSe<sub>2</sub> wafers cut from the ingot had  $\sim 2$  mm thick and  $\sim 20 \text{ mm}^2$  surface area.

The chemical composition of the studied crystal was determined by the energy dispersive spectroscopic analysis using a scanning electron microscope (SEM). The energy dispersive X - ray (EDX) analysis performed at room temperature confirmed the formula composition of the undoped TlGaSe<sub>2</sub>. The SEM inspection also showed that the TlGaSe<sub>2</sub> sample involved an insignificant percentage of background impurities, such as carbon, oxygen and silicon. Results of the EDX analysis are presented in fig. 1.

All electrical measurements were performed using the liquid - nitrogen optical cryostat. The sample was mounted on the cold finger of the cryostat by a non - conducting varnish.

The temperature was controlled by temperature controller with an accuracy of  $\pm 0.1$  K. The photovoltaic spectra of the sample were measured employing a monochromator and Keithley 617 Electrometer to record the short - circuit photovoltaic signals from the crystal. Measurements were carried out using computer interfaced instruments. The incident light was provided by 100 W tungsten halogen lamps. For measurements, two top and two backside gold electrodes were sputtered into the freshly cleaved surfaces by the vacuum deposition method in the *gap* geometry.

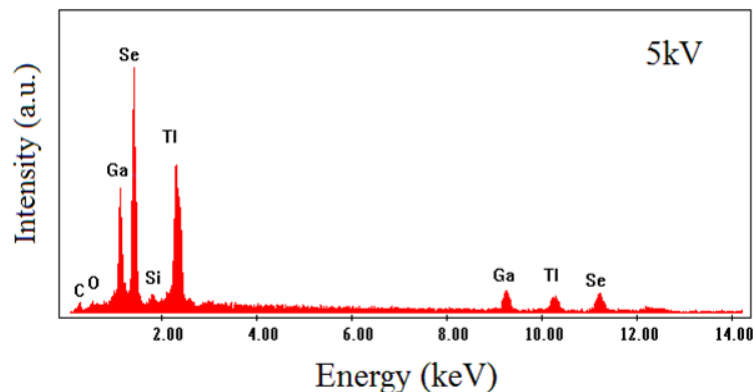


Fig. 1. The results of the EDX analysis of TlGaSe<sub>2</sub> performed in the SEM.

Thin copper wires were attached to the electrodes by high - purity silver paste drop for circuit connection. During front illumination experiments, two top Au - electrodes were always kept in the dark to prevent the influence of any electrical contact photovoltage.

The pyroelectric properties of TlGaSe<sub>2</sub> were studied by quasi - static method in the shorted - circuit regime. Different TlGaSe<sub>2</sub> sample (rectangular in the form with thickness  $\sim 3.2$  mm and surface face area  $\sim 7 \times 5$  mm<sup>2</sup>) with electrode faces perpendicular to the polar [010] axis was used for pyroelectric measurements. The temperature was changed under linear temperature heating with a uniform rate of  $\sim 15$  K/min and pyroelectric current was measured using a high precision digital Keithley - 485 picoammeter coupled to a computer. The electronic grade silver paste was painted onto the surface faces of the sample to form electrodes. Two thin wire terminals were used as external leads to make the sample free and to avoid any stress on it.

The pyroelectric current ( $i_p$ ) measurement consisted of two steps: the polarization procedure and depolarization procedure. In the first step, a sample was electrically polarized under an applied bias electric field  $\sim 500$  V/cm by cooling in darkness from the room temperature to different an off - temperature ( $T_{off} = 280, 270, 260, 250, 240, 137.5, 135, 130, 127.5, 125, 115, 100$  K) using high voltage power supply. The applied electric field was kept until the sample was cooled to  $T_{off}$ . After cooling to  $T_{off}$ , the applied electric field was released and the sample was cooled down to 77 K. After the polarization procedure, the polarized sample was depolarized by thermal stimulation. The sample was connected to an ammeter and then heated at a constant heating rate. The pyroelectric currents accompanying the depolarization were measured at the heating process.

Photo induced current transient spectroscopy (PICTS) employing sub - bandgap excitation pulses is used for studying defect levels in high - resistivity materials as TlGaSe<sub>2</sub> [13 - 19]. To obtain information about the native deep levels in TlGaSe<sub>2</sub> sample the photo induced current transients are recorded between 77 K and 350 K. From the temperature dependence of the thermal relaxation times, the activation energy ( $E_t$ ) and the capture cross-section ( $\sigma_t$ ) of the native deep level were calculated. TlGaSe<sub>2</sub> sample with a parallel contacts geometry was used. Both contacts were on the lateral sides of the sample and the region between the contacts was illuminated to produce the photoconductive response. The indium contacts were soldered to the lateral sides of the sample. The metallic contacts were ohmic ones. The spacing between two indium electrodes was about 2 mm. The measuring circuit was typical for photocurrent investigation. A bias voltage of 50 V was applied across the sample contacts.

The registration of photoresponse decays was performed over the temperature range of 77 – 350 K in a temperature step of 1 K on heating. The sample was mounted in vacuum inside a liquid – nitrogen - cooled cryostat with a transparent entrance window. The sample was placed on massive aluminum cold finger of the cryostat. The Hell 700 temperature sensor is attached to the sample holder near the sample for monitoring its

temperature, and also connected to a temperature controller. A heater attached to the sample holder enables temperature control from 77 to 350 K using a programmable heating rate. The heating rate was 2 K / min. The measurement is based on the fact that during the light pulse empty carrier traps are filled with generated photocarriers, leaving an increase in majority carrier concentration and resulting in an increase in conductivity. Thermally stimulated processes then cause emission of the trapped minority carriers, which induces a decay of the photocurrent. Current transients are recorded at various temperatures and analyzed in a way similar to that used in deep level transient spectroscopy to obtain the trap release kinetics.

A Xenon lamp was used as the light source. Light from a Xenon lamp was monochromated before being irradiated on the sample. The sample excitation was provided by monochromatic light with wavelength 1051 nm that corresponding to a photon energy  $h\nu \sim 1.36$  eV (less than the fundamental absorption edge of TlGaSe<sub>2</sub>) with the scan range  $\Delta h\nu = \pm 0.03$  eV. Photon with energy  $h\nu \sim 1.36$  eV is not completely absorbed near the sample surface and this excitation is uniform throughout the bulk of TlGaSe<sub>2</sub>. Thus photo - excitation pulse corresponds to a good detectable photoelectrical response of the TlGaSe<sub>2</sub> crystal. The photon flux density was  $10^{15}$  cm<sup>-2</sup>s<sup>-1</sup> at the sample surface. The frequency of pulse excitation was equal to 20 Hz with light-to-dark duration in the ratio of 1:5. The duration of excitation pulse was 30  $\mu$ s.

The illumination light was perpendicular to the layer plane of the crystal. The light beam is tightly focused on the optical chopper to minimize the cut - off time of the light beam. The transient signal from the sample during the dark interval is captured at each selected temperatures and processed online using data acquisition and control software. The photocurrent transients were normalized with respect to the photocurrent amplitude at the end of the light pulse. The experimental setup was described in [20].

A home - made data acquisition system with preliminary processing and registration of transient data on a personal computer was used. Point wise accumulation and averaging were carried out across 64 realizations of photoresponse decay containing 2000 samplings located at a fixed time interval  $\Delta t = 62$   $\mu$ s. Taking into account the ferroelectric nature of the crystal the photo response transient was monitored and recorded also. A conventional Deep Level Transient Spectroscopy (DLTS) technique was applied for the photoresponse transient analysis using a rectangular lock - in weighting function. The data registration allowed the characterization of relaxation times in the range of 0.2 to 20  $\mu$ s with regard to the selected conditions.

### 3. RESULTS

#### 3.1. PICTS. Principles and Theoretical Background.

PICTS was originally proposed to determine the trap energy level and capture cross section of deep defects in high - resistivity materials [13-21]. The principle of PICTS technique have been reported in numerous studies [13-21]. It is the variant of DLTS method [22], where the



light excitation is used to creation of defects filling by non-equilibrium charge carriers. In this technique, a voltage is applied between two ohmic contacts on the sample. Electron - hole pairs were generated in the entire depth (by choosing the appropriate wavelength of the light) of the sample by a light pulse. During this illumination time period the defects (electron and hole traps) will be filled by carriers generated by light, this process is called the filling process of the traps. Immediately after removal of the optical pulse at  $t = 0$ , electrons and holes trapped in the defects will now emit and drift in the electric field when  $t > 0$ . The process is called the emission of the charge carriers from the traps. A rapid decrease in the current flowing through the sample owing to the recombination of free photocarriers is observed followed by a slower current transient owing to the thermally stimulated release of carriers from traps. This current transient is the source of the PICTS signal [13-21].

As a result the investigation of electrical activity of defects in high - resistivity or semi insulating materials is allowed. Under the investigation of semiconductors with ferroelectric properties it is important that light impulse with suitable photon energies can change the defects charge state without significant perturbation of crystal domain structure. The last case take place under applying the conventional DLTS technique of defects filling by using electrical field or current impulses that is not applicable for our study.

To obtain information about the deep levels of a semiconductor with PICTS, the thermal relaxation times  $\tau_i$  must be calculated from the time dependence of the photoinduced current transient  $I(t)$  [21-23]:

$$I(t) = I_0 + \sum_{i=1}^n \gamma_i \frac{e^{-t/\tau_i}}{\tau_i}, \quad (1)$$

where  $n$  is the number of distinct deep levels,  $I_0$  denotes the dark current and the coefficient  $\gamma_i$  specifies the contribution of each level to the photo-induced current.

When the light excitation is switch off, the thermal emission of trapped carriers from the defects is governed by the physical process of thermal detrapping, with a characteristic time constant that depends strongly on the temperature. The temperature dependence of the thermal relaxation times is inversely proportional to the emission rate  $e_t$  which is given by [21]:

$$e_t(T) = \frac{1}{g} \sigma_t v_{th} N_c \exp(-E_t/kT) = \sigma_t T^2 B \exp(-E_t/kT), \quad (2)$$

where  $g$  is degeneracy factor;  $v_{th}$  is thermal velocity;  $N_c$  is effective density of states in the conduction band;  $\sigma_t$  is the apparent capture cross - section of the trap levels;  $B$  is a temperature independent factor;  $E_t$  is the activation energy of the recharging defect,  $k$  is Boltzmann constant,  $T$  is the absolute temperature. From equation (1) the activation energy  $E_t$  and capture cross - section  $\sigma_t$  can be extracted by applying the conventional procedures of

DLTS analyze [22] to the set of collected transient data. Namely, the slope of the Arrhenius plot was used for an estimation of  $E_t$ . Estimation of effective capture cross - section was determined from the intersection point of the Y - axis and extrapolated Arrhenius plot. The  $T^2$  correction was used in accordance with equation (1).

Thus for each of the deep level traps detected in TiGaSe<sub>2</sub> the temperature dependence of the thermal emission rate was drawn and fitted with the Arrhenius formula.

### 3.2. Characterization of Traps

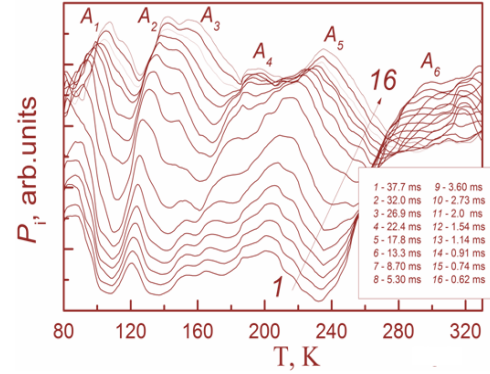


Fig. 2. PICTS spectra of TiGaSe<sub>2</sub> corresponding to the listed characteristic relaxation times. The spectra are normalized to the height of the maximal peak and shifted along Y - axis.

Fig. 2 shows the PICTS spectra of the higher resistivity undoped TiGaSe<sub>2</sub> sample in the temperature range from 80 to 330 K corresponded to different characteristic relaxation times, where six major peaks labeled as A1 - A6 are present.

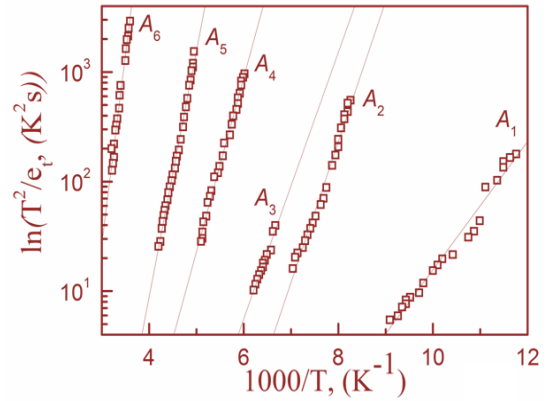


Fig. 3. Rate of charge carrier emission from deep level traps in TiGaSe<sub>2</sub> as function of temperature by taking into account  $T^2$  correction. Solid lines represent the fitting to experimental data.

The Arrhenius plots ( $\ln(e_t/T^2)$  versus  $10^3/T$ ) of the six traps are shown in fig. 3 and the resulting activation energy and the apparent capture cross section of traps

A1 - A6 are reported in table 1. While evaluating  $\sigma_t$  the effective mass of holes was taken 0.14  $m_0$  [24]. The error associated to the activation energy has been calculated from a chi - squared fitting procedure to

each data set of the Arrhenius plot and resulted to be approximately 4%. Also, the temperature ranges  $\Delta_0 T$  for

detected signals from traps are presented in the first column of the Table 1.

Table 1.

Trapping parameters of TiGaSe<sub>2</sub> layered crystal

Defect	$\Delta_0 T$ K	$E_t$ eV	$\sigma_t$ cm <sup>2</sup>
A <sub>1</sub>	65-110	0.12	$1.5 \cdot 10^{-16}$
A <sub>2</sub>	120-140	0.26	$2.8 \cdot 10^{-13}$
A <sub>3</sub>	150-160	0.27	$1.1 \cdot 10^{-13}$
A <sub>4</sub>	165-195	0.31	$1.2 \cdot 10^{-14}$
A <sub>5</sub>	200-240	0.45	$3.8 \cdot 10^{-13}$
A <sub>6</sub>	280-310	0.68	$2.3 \cdot 10^{-12}$

It is worth noting that, PICTS measurements have also revealed the presence of signal from trap located at  $T \geq 320$  K. The last defect signal signature is not considered in the present study, because we have focused our attention on an analysis of the carrier traps which emit at 80 – 300 K temperature, as these are the native deep levels which mostly affect the electrical properties of TiGaSe<sub>2</sub>.

The position of maximum of deep trap levels A<sub>1</sub> and A<sub>2</sub> on the temperature scale of PICTS spectra corresponds to the temperatures of phase transition temperatures in C and INC – phases, respectively [4 - 11]. The shift at the temperature position of the maximum in the set of spectra, which corresponds to various characteristic relaxation times, is good when compared to the thermal activation of emission from the defects that are filled under photo excitation. It should be noted that, it is not possible to determine the signs of the carriers trapped by centers (electrons or holes) in PICTS technique. We proposed that the detected defects are the traps of majority carriers since such trap centers are mostly observed in highly - resistive semiconductors having a wide band gap [14].

### 3.3 Pyroelectric Response from the TiGaSe<sub>2</sub> crystal

The spontaneous polarization of ferroelectrics changes with temperature most rapidly in the vicinity of the phase transition point, so for monodomain samples the sharp maximum observed in the temperature dependence of the pyroelectric current is associated with the Curie temperature,  $T_c$ . The basic formula for pyroelectric current ( $i_p$ ) measurements is [25]:

$$i_p(T) = \gamma S \frac{dT}{dt}, \quad (3)$$

where  $\gamma$  is the pyroelectric coefficient,  $S$  the electrode area, and  $dT/dt$  is the heating rate.

Assuming a second order phase transition [26], with a continuous temperature decreasing of the spontaneous polarization (it becomes zero at the transition temperature), then the temperature variation of the pyroelectric coefficient is [27]:

$$\gamma = - \frac{1}{2 \sqrt{\left(\frac{\alpha}{\beta}\right)(T_c - T)}}, \quad (4)$$

where  $\alpha$  and  $\beta$  are the coefficients of the free energy polynomial expansion in the Ginzburg – Landau theory of ferroelectric phase transitions [26]. According to eq. (3) and (4), the pyroelectric current will have a discontinuity at the ferroelectric phase transition temperature.

Pyroelectric current measurements were performed in a temperature range covering the phase transition temperatures in TiGaSe<sub>2</sub>. The results are presented in fig. 4-7. All curves presented in fig 4-7 can be divided in three parts.

The temperature dependence of pyroelectric current for TiGaSe<sub>2</sub> together with a background  $i_p(T)$  corresponding to unpoled sample (after the zero field cooling) are seen in fig. 4. This is a first part of the results. Fig. 5 shows that the pyroelectric response of TiGaSe<sub>2</sub> is nearly the same for unpoled regime and for the sample poled by applied bias from room temperature to 280 and further up to 250 K.

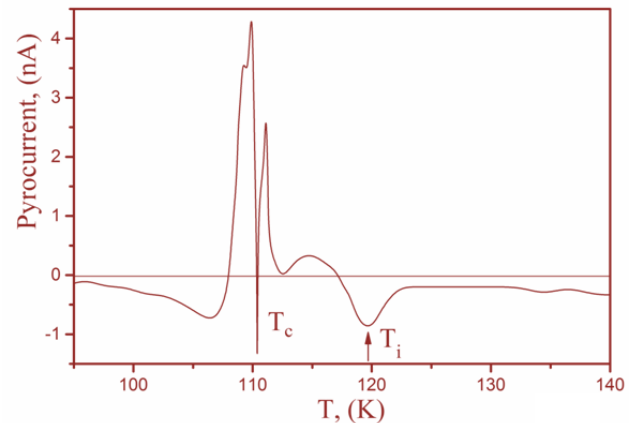


Fig. 4. Temperature dependence of the depolarization current of TiGaSe<sub>2</sub> for unpoled sample.

As a whole the positive pyroelectric signal with small sharp negative piece in the vicinity of  $T_c$  in heating runs is the common characteristic of all first part result. In other words, the post - poling pyroelectric activity of

TlGaSe<sub>2</sub> near  $T_c$  are the same as for unpoled sample. It can be concluded that external electric field applied to crystal at cooling from room temperature up to 250 K was

freeze in the crystals when the poling field is removed from sample.

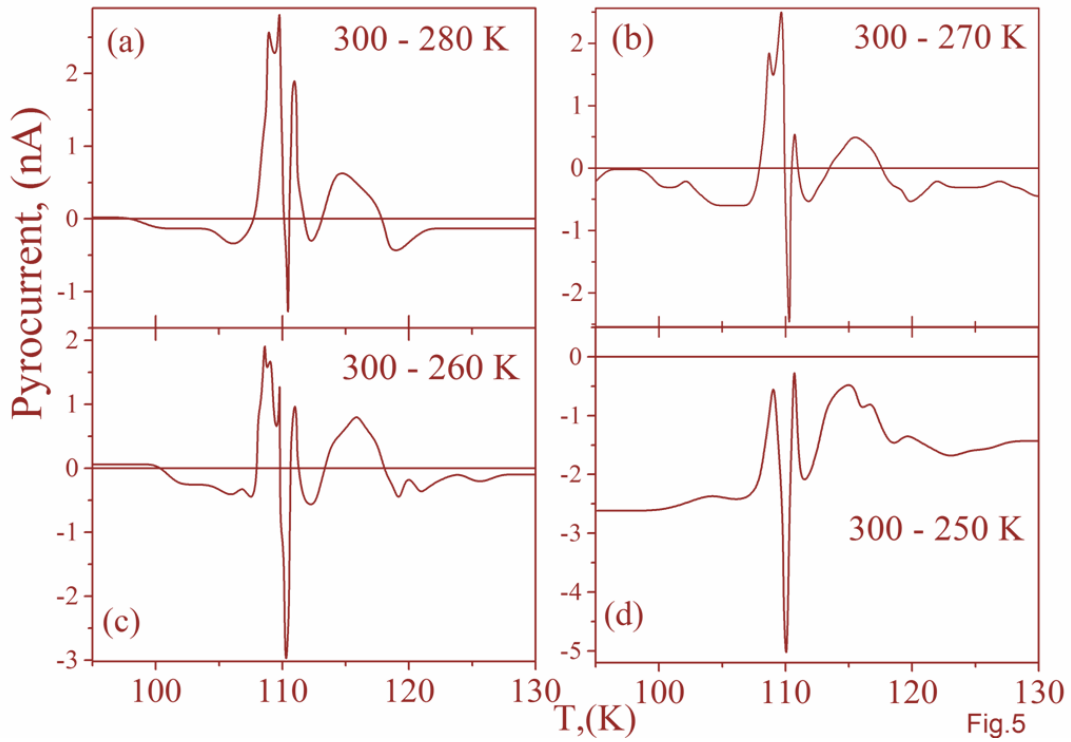


Fig. 5. Temperature dependence of pyroelectric current generated in TlGaSe<sub>2</sub> after sample poling under external electric bias field 200 V/cm at cooling from room temperature to: (a) 280 K; (b) 270 K; (c) 260 K and (d) 250 K. The heating rate was 15 K/min:

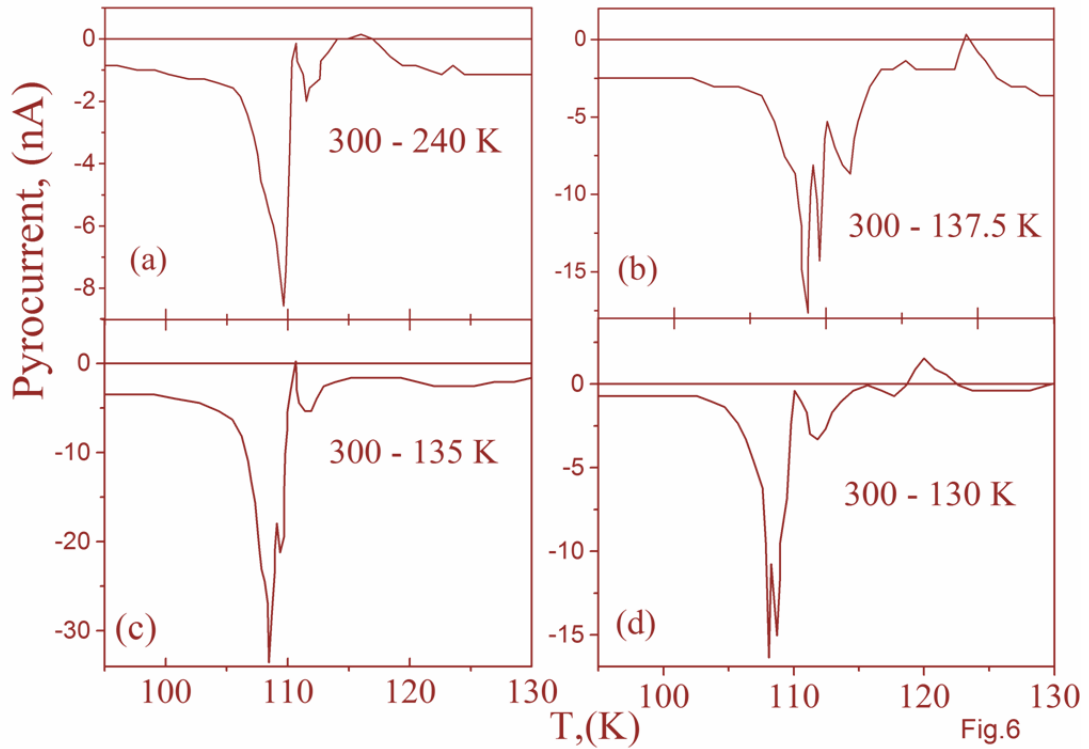


Fig. 6 - Same as Fig. 5, but the sample was poled from room temperature to: (a) 240 K; (b) 137.5 K; (c) 135 K and (d) 130 K.



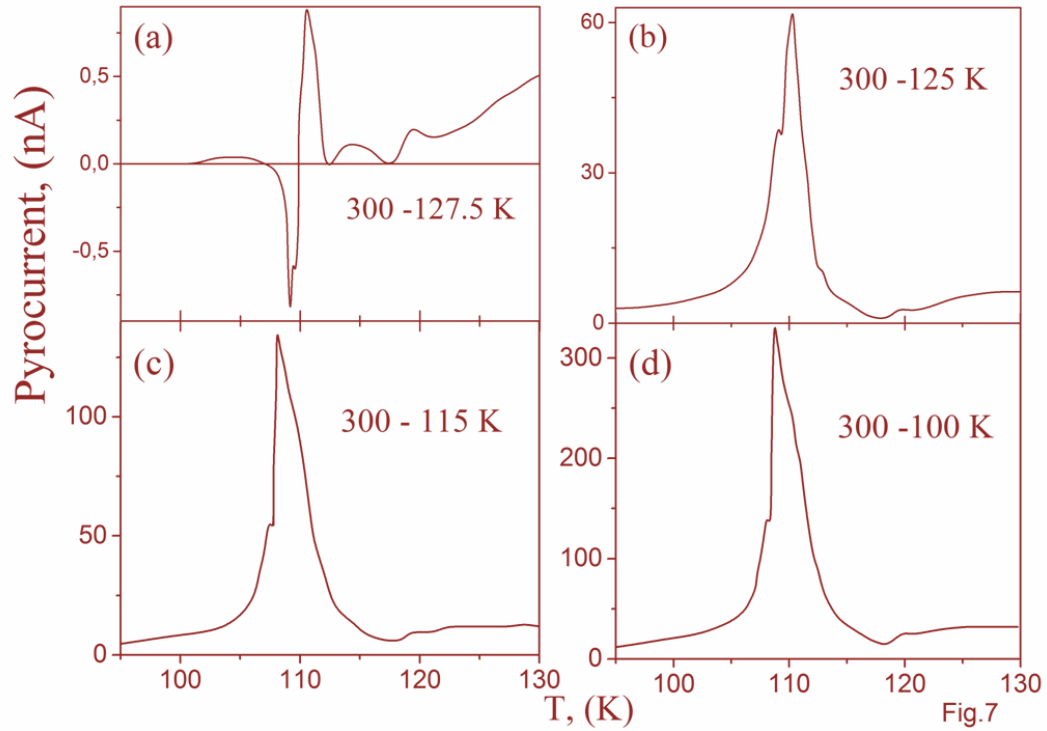


Fig. 7 - Same as Fig. 5, but the sample was poled from room temperature to: (a) 126.5 K; (b) 125 K; (c) 115 K and (d) 110 K..

As the poling process proceeds from room temperature to 240 K and further up to 130 K the pyroelectric response of TlGaSe<sub>2</sub> is completely negative by approaching to the Curie transition temperature in heating regime, as shown in fig. 6. We note, that the monodomain state in TlGaSe<sub>2</sub> was obtained during poling crystal in paraelectric phase, that is temperature regions higher than the Curie temperature. This is a second part of the results.

The variation of  $i_p$  with temperature for third part of results is depicted in fig. 7. This series of the pyroelectric current measurement were carried out for the TlGaSe<sub>2</sub> sample poled by applied bias field from room temperature to 127.5, 125, 115 and 110 K, respectively. The most common feature of these results is the positive sharp and very large pyrocurrent maximum around the Curie transition temperature observed during the heating run.

By short circuiting poled TlGaSe<sub>2</sub> sample with an electrometer and applying to crystal a constant heating rate, we don't expect to find the pyrocurrent sign changing in pyroelectric current measurements. The next questions arise:

1) What is the bias electrostatic field source responsible for the TlGaSe<sub>2</sub> crystal unipolarity in the ferroelectric phase, when the polarizing field was switched off at temperatures more far from the Curie point?

2) Why does a negative pyroelectric signal record when the poling process covers the temperature interval ~ 130 – 240 K only?

Thus, it has been experimentally verified that the pyroelectric response of TlGaSe<sub>2</sub> crystal greatly depends on the poling prehistory. This means, that unipolarity of TlGaSe<sub>2</sub> in the ferroelectric phase is

provided by the internal electrostatic fields built up into crystal over the poling process even if the poling electric field was removed from sample in paraelectric phase that is at temperatures more far from  $T_C$ .

Electroactive materials, which are able to retain electric polarization over a long period of time and to create an internal static electric field, are known as electrets [28, 29]. The term *electrets* was proposed over a century ago to describe a material that is the electrostatic equivalent of a magnet [28, 29]. Electret properties have been reported in insulators and semiconductor materials [28-31]. It is well known that electret behavior of dielectric and semiconductor materials arises from both the dipole orientation and the charge storage.

It is generally accepted that electret states in ferroelectric - semiconductor crystal submitted to an external electric field may be originated from hetero- and homocharges [28-31]. An internal electric field created by temporary residual space charges accumulated in the trap levels in the regions directly adjacent to the electrodes (surface electric field) as well as in bulk region of the crystal [28-31]. An internal electric field created by heterocharges formed near the surface region of crystal has the same direction as the polarity of the voltage applied on the sample. An internal electric field created by homocharges formed in the bulk region of crystal has the direction opposite to the direction of applied polarity.

Suppose the polarity of the poling voltage applied to the sample during electret formation is positive with respect to the ground. If total pyroelectric current is positive, it is produced by heterocharges (with a polarity opposing that of the electrode), and if the pyroelectric current is negative, it is due to homocharges.

The electret states in ferroelectric – semiconductors were found to depend on the deep level defects [30, 31]. The presence of defects promotes the formation of dipoles formed by charging deep level traps. Orientation of dipoles is chaotic without the applied field, while in its presence, quasi dipoles are oriented in the direction of applied field. This built – in internal electret field is far from being completely disappear even after a long time because discharged processes have a low speed at low temperatures.

Self - polarization of  $\text{TiGaSe}_2$  crystal due to charged trapping centers produce the pyrocurrent signal that exhibit anomalies in the region of phase transitions as it is shown in figs. 5 - 7. Note that the poling procedure for normal ferroelectrics always requires application of a strong external electric field inside the ferroelectric phase. Self - polarization of  $\text{TiGaSe}_2$  occurs outside the ferroelectric phase and pretreatment of crystal under high external electric fields within the ferroelectric phase can be avoided. An internal electric field appeared in  $\text{TiGaSe}_2$  sample above  $T_c$  due to charge deep level defects is higher than the coercive field at Curie temperature.

As regards the heterocharges produced in the  $\text{TiGaSe}_2$  sample surface upon application of an electrical field, a property of great importance for this material. As will be shown below, the real  $\text{TiGaSe}_2$  is non - homogeneous sample having different electrical and dielectric properties near the surface region and in the bulk. The two - layer condenser (parallel - plate capacitor) model should be considered in this case, which can lead to the redistribution of the surface and bulk internal electric fields inside  $\text{TiGaSe}_2$  and thus to change the sign of the pyroelectric current during heating.

### 3.4. Photovoltaic response from the $\text{TiGaSe}_2$ crystal

Fig. 8 (a) shows typical representation of spectral distribution of photovoltaic signal in the front illumination geometry of  $\text{TiGaSe}_2$  crystal in the 400 - 700 nm wavelength range. It can be seen from the fig. 8 (a), that the photovoltage shows a broad peak at  $\sim 655$  nm. The observed photovoltaic peak can be attributed to exciton absorption according to existing data [32].

The photovoltaic response of  $\text{TiGaSe}_2$  in the backside illumination geometry plotted against the wavelength of the incident light is shown in fig. 8 (b). Well - defined oscillations over the photo - wavelengths ranging from 400 to 700 nm are observed with periods  $\sim 100$  nm. Oscillations of photocurrent in thin plates of layered semiconductors are well known and can be easily explained taking into account the interference of the light in the thin semitransparent film [33]. However, oscillations shown in fig. 8 (b) cannot be due to interference of light beams reflected from the front and back surfaces of the sample. Really, simple estimations of interference period  $\Delta\lambda$  based on the well - known formula  $\Delta\lambda = \lambda_m \lambda_{m+1} / 2nd$  (where  $n$  is the refractive index of material;  $\lambda$  is the wavelength of light and  $m$  is the order of interference;  $d$  is the thickness of the parallel crystal plate [33]) show that observed period ( $\Delta\lambda \sim 100$  nm) is at least three orders of magnitude larger than the expected value taking into account the real thickness of

the sample  $d$ . Only very thin layer with refractive index,  $n$ , different from that of bulk  $\text{TiGaSe}_2$  can give the interference pattern with such a big period. Taking into account the average values for refractive index of  $\text{TiGaSe}_2$  crystals known from the literature [34], the approximate value for the thickness of proposed thin layer near the surface of the crystals is obtained to be some portions of the micron.

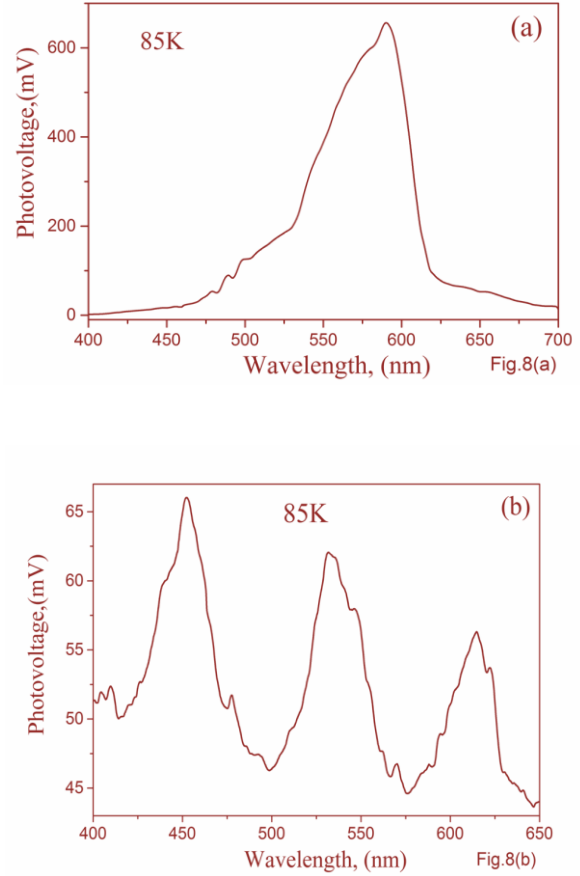


Fig. 8. Open – circuit photovoltaic spectra of  $\text{TiGaSe}_2$  in: (a) the front illumination geometry at room temperatures; (b) the backside illumination geometry at  $T < 130$  K.

So we can propose the existence of some thin layer near the surface of  $\text{TiGaSe}_2$  sample with physical parameters (refractive index, resistivity, dielectric function, conductivity and etc.) different from those for the bulk part of the sample. According to our data, oscillations of photoresponse can be registered only at temperatures lower than  $\sim 130$  K. Described properties of the thin layer are very close to the properties of ferroelectric dead layer discussed in the literature [35, 36]. In our opinion, it is the high quality of the surfaces of layered ferroelectric crystal  $\text{TiGaSe}_2$  that allows registering the dead layer in this crystal in a simple way.

### 4. SPACE CHARGE AND INTERNAL FIELD DISTRIBUTION IN $\text{TiGaSe}_2$

We consider a very simple model location of internal static electric fields in two - layer condenser [37]. Although the model presented here is probably quite artificial, since dielectric medium within of this model is supposed to be consisting of two different parallel

dielectric layers instead of three for dead layer model, there is a good chance to elucidate the salient features and the specific details of our experiments in the framework of the simplest parallel - plate capacitor.

It is necessary to underline that TlGaSe<sub>2</sub> ferroelectric – semiconductor is a native inhomogeneous ferroelectric. Dielectric properties of such inhomogeneous ferroelectric in a radio frequency should be identified in the frame of Maxwell – Wagner relaxation process. In our previous study, we successfully employed a Maxwell – Wagner polarization model for analyzing the dielectric relaxation characterization of TlGaSe<sub>2</sub> ferroelectric - semiconductor over a broad frequency range in the temperature region 140 – 200 K [10, 11].

Let us to consider a parallel plate capacitor with a heterogeneous dielectric medium occupying the entire space between the two parallel fixed electrode plates. A heterogeneous dielectric medium may be presented as set of the bulk dielectric plate having the dielectric constant  $\varepsilon_b$ , conductivity  $\sigma_b$ , the thickness  $h_b$  and surface dielectric layer characterized by dielectric constant  $\varepsilon_s$ , surface conductivity  $\sigma_s$ , and thickness  $h_s$ , respectively. If the capacitor is suddenly excited by a power supply with the source bias voltage  $U_0$ , the electrodes are charged instantaneously and static electric field distribution in two dielectric plates will correspond to the electrostatic requirement of constant flux density.

$$D_s = D_b \quad \text{or} \quad \varepsilon_s E_s = \varepsilon_b E_b \quad (5)$$

where  $E_s$  and  $E_b$  static electric field intensity in surface and bulk dielectric plate.

Expressions for the electrostatic field in two dielectric layers are:

$$E_s = \frac{\varepsilon_b U_0}{h_s \varepsilon_b + h_b \varepsilon_s} \quad \text{and} \quad E_b = \frac{\varepsilon_s U_0}{h_s \varepsilon_b + h_b \varepsilon_s} \quad (6)$$

(the permittivity of free space is equal to 1 as in CGS - units). Noting that in the presence of the source voltage  $U_0$  the voltage distribution between faces of two dielectrics are:

$$U_0 = U_s + U_b = E_s h_s + E_b h_b \quad (7)$$

From (2) one can find that

$$\frac{E_s}{E_b} = \frac{\varepsilon_b}{\varepsilon_s} \quad (8)$$

As a result, the local electrostatic field occurring in surface and bulk dielectric layer is inversely proportional to their dielectric constant at moment, when the heterogeneous dielectric is subjected the power supply.

Next we examine the electrostatic field distribution in surface and bulk dielectric layer when the excited source voltage is applied to the two - layer condenser for the long time. The final distribution of electrostatic fields between layers finds from the condition of current continuity.

$$j_s = j_b \quad \text{or} \quad \sigma_s E_s = \sigma_b E_b \quad (9)$$

From eqs. (3) and (5) it follows that:

$$E_s = \frac{\sigma_b U_0}{h_s \sigma_b + h_b \sigma_s} \quad \text{and} \quad E_b = \frac{\sigma_s U_0}{h_s \sigma_b + h_b \sigma_s} \quad (10)$$

The final (even when the power supply is disconnected from the capacitor) relation between  $E_s$  and  $E_b$  electrostatic field intensity depends on the conductivity of the layers, but it is always the dielectric constant of the layer is proportional to it conductivity (from (2) and (6)).

$$\frac{\varepsilon_s}{\varepsilon_b} = \frac{\sigma_s}{\sigma_b} \quad \text{or} \quad \frac{\varepsilon_s}{\sigma_s} = \frac{\varepsilon_b}{\sigma_b} \quad (11)$$

It can be found from (6), the drastically increase of  $\sigma_s$  in the surface layer region due to, for example, phase transition on the surface will accompany by predominance of  $E_b$  electrostatic field intensity conserved in the bulk of the crystal. We shall discuss this situation next.

It is natural to speculate that TlGaSe<sub>2</sub> is inhomogeneous crystal. At this case we have two types of internal biasing fields of different source and direction, as it follows from the expressions (6) or (10). The internal biasing field is terminated at the thin surface layer of TlGaSe<sub>2</sub> causes to appear of the pyrocurrent signal which is rising in the positive direction. The main source of this field is the heterocharges: both injected from electrodes and accumulated near the electrodes, and the deep trap levels together with their oppositely charged counterparts. These charges create a sufficiently strong local surface internal electric field that causes the polarization of TlGaSe<sub>2</sub> crystal during the cooling to ferroelectric phase. The sample is still fully polarized after crystal poling from room temperature to below  $\sim 130$  K. That means that surface internal field implies the majority role in comparison with the imprinted bulk internal electric field.

The internal bias field frozen in the bulk region of TlGaSe<sub>2</sub> responsible for the unipolarity of sample in the ferroelectric phase can produce a pyrocurrent rising in the negative direction during heating run. During the poling process of TlGaSe<sub>2</sub> at cooling from room temperature to  $\sim 240$  K and further up to  $\sim 130$  K the  $E_b$  becomes larger than  $E_s$ . Thus the negative pyroelectric current is associated with bulk frozen bias field which may be originated from space charge accumulated on deep trapping carries centers, for example intrinsic defects, which should always be present in real crystals.

As we mentioned previously, the eq. (10) defines the final distribution of  $E_s$  and  $E_b$  electrostatic fields after a sufficiently long period of time when the initial voltages is removed from sample and after the short circuit has been applied to the sample. According to the expression (10), the condition  $E_b > E_s$  gives  $\sigma_s > \sigma_b$  (or  $\varepsilon_s > \varepsilon_b$  as it follows from the expression (7)). If we assume that in the temperature region  $\sim 130 - 240$  K the conductivity of surface layer is much higher than that of the bulk of crystal then we can fully interpret our experimental results. We may thus conclude that negative pyrocurrent response of TlGaSe<sub>2</sub> is associated with drastically

increase of surface conductivity (or dielectric constant (11)) of crystal in the temperature region  $\sim 130 - 240$  K.

The reduction of the surface conductivity (or dielectric constant) below  $\sim 130$  K must lead to  $E_s > E_b$ . A steady at very long time internal biasing field in the thin surface layer of  $\text{TiGaSe}_2$  could exist, if it is an unpolarized surface layer. Such unpolarized surface layer doesn't compensate external electrostatic field created by charges injected from electrodes. In the ideal case, this surface layer substance should have zero conductivity or dielectric constant  $\varepsilon = 1$ . Such properties are inherent a dead layer on the ferroelectric surface. Keeping in the mind described phenomena it is possible to assume formation of insulator (deal / depletion) layer at the surface of  $\text{TiGaSe}_2$  crystal in the ferroelectric phase.

## 5. DISCUSSION OF EXPERIMENTAL RESULTS

Analysis of the experimental results enables us to draw the following conclusions. The negative sign of the pyroelectric current peak around the Curie phase transition observed after sample poling in the temperature regions well above  $T_c$  (figs. 5 and 6) indicates that built-in electric field within  $\text{TiGaSe}_2$  are mainly produced by deep level trapping centers A3 – A6. These are native bulk deep level defects which are localized in crystalline regions. The origin and nature of A3 – A6 deep trapping centers is not known to date.

The native A3 – A6 deep level defects can form a complex system of electrical dipoles which are aligned upon poling conditions. Mobile carriers captured by these deep trapping centers generate macroscopic internal electric field inside the  $\text{TiGaSe}_2$  which promote self-poling of the sample in the ferroelectric phase. Thus, deep level trapping centers A3 – A6 impact the negative pyroelectric current profile of  $\text{TiGaSe}_2$  after poling of the crystals in the temperature regions from 300 to 130 K. The pyroelectric response of  $\text{TiGaSe}_2$  originated from A3 – A6 deep level trapping centers is analogous to the influence of homocharges.

It should be mentioned that as for unpoled and poled in a temperature range of 300 – 260 K  $\text{TiGaSe}_2$  the pyroelectric current peak had a part in the positive direction at the Curie temperature as it can see from fig. 4 and fig. 5. In fact, it is rather a combination of pyroelectric current due to the effective internal field localized at the surface and in the bulk of crystal that is from a hetero- and homocharges. This behavior may be explained if we consider that injection of carriers during electret formation in the paraelectric phase (300 – 260 K) will also cause a polarization in areas near the electrodes. An important point to note is that the sign of the charge is the same as that of the corresponding forming electrode, i.e. they are heterocharges. Such physical mechanism of polarization is called space-charge polarization [28-31]. A pyroelectric current peak at  $T_c$  from frozen-in space-charge polarization at the surface of  $\text{TiGaSe}_2$  must have positive direction. Comparison of the experimental data shows that the internal field originated from the injected charges and mainly deposited in the surface or near-surface region close to the electrode boundaries of  $\text{TiGaSe}_2$  during the poling process mentioned above gives

a small contribution in positive value of pyrocurrent peaks at  $T_c$ .

Finally, we discuss the behavior of pyrocurrent shown in fig. 7, where the  $\text{TiGaSe}_2$  sample was polled across temperature region that includes the ICN – phase. Note that the poling procedure for normal ferroelectrics always requires application of an external polling field inside the ferroelectric phase that is below  $T_c$ .

It needs to be pointed out that average polarization inside ICN – phase must be zero because the ICN - phase possesses the center of inversion symmetry [26]. This means that during poling process the external electric field does not induce aligned polarization inside ICN – phase. In contrast, our results support the existence of a coupling between the bias electric field and the aligned polarization inside ICN – phase. We may anticipate that the major contributions in retained polarization of the ICN – phase comes from A2 defects.

The origin and nature of A2 deep trapping center is not known too. However, we would like to briefly discuss the microscopic properties of the A2 deep level defect. It can be seen from fig. 6 that pyroelectric current peak always has positive polarity, without any negative component when the  $\text{TiGaSe}_2$  sample is cooled under the external poling field across the temperature range of ICN – phase. It can be concluded that A2 trapping centers are deep charged defects localized near the surface region of  $\text{TiGaSe}_2$ .

Due to a lack of translational symmetry,  $\text{TiGaSe}_2$  layered crystals within the temperature region of the existence of ICN – modulated phase are the examples of aperiodic or quasiperiodic crystals, i.e. the basic structure with space group symmetry has a periodic modulation with wave vectors not belonging to the reciprocal lattice of the basic structure [26].

As a consequence of the structural distortions, the static dielectric constant of  $\text{TiGaSe}_2$  inside the ICN – phase has the giant ( $\varepsilon \sim 1500$ ) value [38]. It is well known that the ionization energy of the traps is inversely proportional to the dielectric constant of the medium. Thus, a substantial amount of mobile charges can be trapped by A2 deep level traps within the ICN – modulated phase. In the presence of an external electrical field, the dipole moments of the charged A2 deep level traps become aligned in the direction of external electric field and thus the electrets state is established. This built-in internal electrets field is far from being completely disappear even after a long time because discharged processes have a low speed at low temperatures. Self-polarization of  $\text{TiGaSe}_2$  due to A2 trapping centers produce the positive depolarization signal at the Curie temperature as it is shown in fig. 7. Thus, self-polarization of  $\text{TiGaSe}_2$  occurs outside the ferroelectric phase and pretreatment of crystal under high external electric fields within the ferroelectric phase can be avoided. An internal electric field appeared in  $\text{TiGaSe}_2$  sample above  $T_c$  due to charged A2 deep level defects is higher than the coercive field at Curie temperature.

The next questions arise:

1. Why does the pyroelectric current magnitude presented in fig. 7 be in about 40 times more than ones in

figs. 5 and 6, if the  $\text{TiGaSe}_2$  sample was cooled under the same external poling field?

2. Why does the polarity of depolarization current from internal electret field originated from A2 deep level centers be positive, while the polarity of pyroelectric current peak from the internal electric field originated from another deep level traps (A3 – A6) either fully negative or demonstrated the negative component, despite the fact that the  $\text{TiGaSe}_2$  sample was cooled under the same external poling field.

As it was concluded from pyroelectric and photovoltaic measurements reported above, the  $\text{TiGaSe}_2$  layered crystal is non – homogeneous medium with different ratios of thickness, dielectric and conductivity properties near the surface and in the bulk. The presence of native thin insulator layer at the surface of  $\text{TiGaSe}_2$  crystal at  $T < 130 \text{ K}$  was assumed from above - mentioned experimental results. If the  $\text{TiGaSe}_2$  sample is non – homogeneous then the majority part of the external poling voltage will be applied to thin surface layer. Therefore, charged A2 deep level traps will be affected by much strong external applied electric field than ones to A3 – A6 defects localized in the bulk of crystal. Thus, for non - homogeneous  $\text{TiGaSe}_2$  compound, the magnitude of a pyrocurrent peak will strongly depend on the surface thin film thickness where A2 deep level traps are polarized and frozen - in during the poling process.

Under the influence of the very strong surface polarization field more vacancies will transport into the surface regions. Thus, great number isolated vacancies coming into the electret surface region will form heterocharges. After removing external poling field the reordered in the direction of the applied field dipoles at the surface of  $\text{TiGaSe}_2$  will take place. Thus, the higher resistive space charge layer will be induced in the surface or near - surface region of  $\text{TiGaSe}_2$  at the temperature of  $T < 130 \text{ K}$ .

The separation of the charged deep trap centers and vacancies near the surface region of  $\text{TiGaSe}_2$  it is necessary, because of contribution of the carries injection from the electrodes under external poling field in the formation of surface heterocharges is minor.

In our opinion, vacancies in  $\text{TiGaSe}_2$  are the Se – vacancies. A second chemical defects which may be responsible for surface heterocharges after poling the sample at  $T < 130 \text{ K}$  are the oxygen ions migrations from the surface of material to the bulk regions. The presence of the small oxygen content has been revealed in all  $\text{TiGaSe}_2$  samples [9] (see also fig. 1). The concentration of oxygen vacancies at  $T < 130 \text{ K}$  can be significantly increase and thereby increase the surface polarization of  $\text{TiGaSe}_2$  sample from heterocharges.

## 6. CONCLUSIONS

In this study, we report on the formation of an internal electric fields in  $\text{TiGaSe}_2$  and its effect on the pyrocurrent peak at  $T_c$ . We demonstrate that the internal electric field generated by native deep level traps localized both in the bulk and near the surface region of  $\text{TiGaSe}_2$ . The  $\text{TiGaSe}_2$  was also studied by PITCS measurements at different temperatures. Using PITCS measurements, six deep energy trap levels in  $\text{TiGaSe}_2$  were observed. The activation energy of all deep centers and their cross sections were determined.

The contribution of each charged defect in polarized properties of  $\text{TiGaSe}_2$  was identified from the pyroelectric current studies. It was shown that native deep defects A3 – A6 are localized in the bulk of crystal. The negative sign of the pyroelectric current peak observed around the Curie phase transition after sample poling in the temperature regions well above  $T_c$  (in the paraelectric phase) are originated from the self – polarization of  $\text{TiGaSe}_2$  under internal electric fields which were created by these deep level trapping centers.

We demonstrate that the positive pyrocurrent peaks observed at the Curie point are attributed to the self – polarization of  $\text{TiGaSe}_2$  under internal electric field formed from charged A2 native deep level defects which are localized near the surface region of  $\text{TiGaSe}_2$ . A2 native traps have the activation energy and the capture cross section 0.26 eV and  $2.8 \times 10^{-13} \text{ cm}^2$  and active in temperature region of the INC – phase existence. The ICN - phase as a medium with giant and stable dielectric constant can be responsible for the ionization of A2 deep defect.

The unusual photovoltaic spectrum was observed in layered ferroelectric  $\text{TiGaSe}_2$  in ferroelectric phase. According to estimations such spectrum can be due to thin (parts of micron) film lying near the surface of the sample and having physical characteristics different from those of the bulk part of the sample. We suppose that high - resistivity  $\text{TiGaSe}_2$  material is an inhomogeneous ferroelectrics with thin depletion surface layers.

By analyzing the polarity and magnitude of pyrocurrent peak observed at  $T_c$  after crystal poling by cooling from 300 to 127.5, 125 and 155 K we suggest the positive sign of pyrocurrent peak is caused by the positive internal field from A2 surface deep level defects. The fact that we do not observe the negative component in the pyrocurrent peak at the Curie point confirms that mentioned peak was produced by space - charge polarization of surface dipoles from heterocharges. The immobilized space charges (electrons and holes), A2 native deep level charged traps and their oppositely charged counterparts, there can be vacancies or ions which drift toward the surface (or migrates from the surface to the bulk regions) by the strong external electric fields applied to the thin native insulator part on the surface of  $\text{TiGaSe}_2$ .

- 
- |   |   |
|---|---|
| <p>[1] J.A. Kalomiros, N. Kalkan, M. Haniyas, A.N. Anagnostopoulos, K. Kambas. Solid State Commun. 96 (1995).601 - 607</p> <p>[2] S. Ozdemir and M. Bucurgat. Solid State Sciences 33 (2014) 25 - 31.</p> | <p>[3] S.G. Abdullaeva, V.A. Aliev, N.T. Mamadov, and M.K. Sheynkman. Sov. Phys. - Semiconductors 17 (1983) 1787 – 1790.</p> <p>[4] MirHasan Yu. Seyidov, Y Sahin, M. H. Aslan,</p> |
|---|---|



- R. A. Suleymanov. *Semicond. Sci. Technol.* 21 (2006) 1633 – 1638.
- [5] D. F. McMorro, R. A. Cowley, P. D. Hatton, and J. Banis. *J. Phys.: Condens. Matter* 2 (1990) 3699 – 3712.
- [6] W. Henkel, H. D. Hochheimer, C. Carlone, A. Werner, S. Ves. H. G. v. Schnering, *Phys. Rev. B* 26 (1982) 3211 – 3221.
- [7] H. D. Hochheimer, E. Gmelin, W. Bauhofer. *Ch.von. Shnering - Schwarz, H. G.von. Shnering, J. Ihringer, W. Appel, Z. Phys. B.: Condens. Matter* 73 (1988) 257 – 263.
- [8] R. A. Suleymanov, M. Yu. Seyidov, F. M. Salaev, and F. A. Milailov. *Sov. Phys. - Solid State* 35 (1993), 348 – 354.
- [9] MirHasan Yu. Seyidov, E. Coskun, Y. Sahin, R. Khamoev, R.A. Suleymanov. *Semicond. Sci. Technol.* 21 (2006) 171 – 174.
- [10] F. Salehli, Y. Bakis, MirHasan Yu. Seyidov, R.A. Suleymanov. *Semicond. Sci. Technol.* 22 (2007) 843 – 850.
- [11] MirHasan Yu. Seyidov, R. A. Suleymanov, F. Salehli, Y. Bakis, *J. Appl. Phys.* 105 (2009) 043710.
- [12] N. I. Agladze, B.P. Antonyuk, V.M. Burlakov, E. A. Vinogradov, and G. N. Zhizhin, *Sov. Phys. - Solid State* 23 (1981) 3289 – 3298.
- [13] J. W. Farmer, C. D. Lamp, and J. M. Meese. *Appl. Phys. Lett.* 41, (1982) 1063 – 1065.
- [14] J.C. Balland, J.P. Zielinger, C. Noguét and M. Tapiero. *J. Phys. D: Appl. Phys.* 19 (1986) 57 – 70; *J. Phys. D: Appl. Phys.* 19 (1986) 71 – 87.
- [15] J.P. Zielinger, B. Pohoryles, J.C. Balland, J.G. Gross, and A. Coret. *J. Appl. Phys.* 57 (1985) 293 – 301.
- [16] S.D. Brotherton. *J. Appl. Phys.* 55 (1984) 3636 – 3643.
- [17] Yutaka Tokuda, Akira Usami and Yajiro Inoue. *Semicond. Sci. Technol.* 2 (1987) 251 – 254.
- [18] O. Yoshie and M. Kamihara. *Jpn. J. Appl. Phys.* 22, 621 (1983); *Jpn. J. Appl. Phys.* 22 (1983) 621 - 628; *Jpn. J. Appl. Phys.* 22 (1983) 629 – 635; *Jpn. J. Appl. Phys.* 24 (1985) 431 – 440.
- [19] A. Blondeel and P. Clauws, *J. Appl. Phys.* 86 (1999) 940 – 945.
- [20] P. Odrinskii, T.G. Mammadov, MirHasan Yu. Seyidov, V.B. Alieva. *Phys. Solid State* 56 (2014) 1605 - 1609.
- [21] P. Blood, J.W. Orton. *The Electrical Characterizations of Semiconductors: Majority Carriers an Electron States* (Academic Press, London, UK, 1992)
- [22] D.V. Lang. *J. Appl. Phys.* 45 (1974) 3023 – 3032.
- [23] Ch. Hurter, M. Boilou, A. Mitonneau, D. Bois. *Appl. Phys. Lett.* 32 (1978) 821 – 823.
- [24] A.F. Qasrawi, N.M. Gasanly. *Material Research Bulletin* 39 (2004) 1353 – 1357.
- [25] R. Chen and Y. Kirsh. *Analysis of Thermally Stimulated Processes* (Pergamon Press, 1981)
- [26] A. Strukov, A. P. Levanyuk. *Ferroelectric Phenomena in Crystals* (Springer, 1998)
- [27] M.E. Lines, A.M. Glass. *Principles and Applications of Ferroelectrics and Related Materials* (Clarendon, Oxford, 1977).
- [28] G.M. Sessler. *Journal of Electrostatics* 51 – 52 (2001) 137 – 145.
- [29] Electrets, ed. by G. M. Sessler (Topics in Applied Physics v. 33, Springer, 1987)
- [30] V.M. Fridkin. *Ferroelectrics - Semiconductors* (Consultants Bureau, New York, 1980).
- [31] V. M. Fridkin. *Photoferroelectrics* (Springer, Berlin, 1979).
- [32] MirHasan Yu. Seyidov, R.A. Suleymanov, Yasin Sale and Ertan Balaban, *J. Appl. Phys.* 116 (2014) 213702.
- [33] F. Klingshirm. *Semiconductor optics* (Springer, 2012)
- [34] M.M. El - Nahass, M.M. Sallam, Samy A. Rahman, E. M. Ibrahim. *Solid State Sciences* 8, (2006) 488 – 499.
- [35] A.M. Bratkovsky, and A. P. Levanyuk. *Philosophical Magazine* 90 (2010) 113 - 124.
- [36] Li - Wu Chang, Marin Alexe, James F. Scott, J. Marty Gregg, *Adv. Mater.* 21 (2011) 4911 – 4914.
- [37] A.R. V. Hippel, *Dielectrics and Waves* (The MIT Press, Cambridge, 1954).
- [38] V.P. Aliyev, S.S. Babayev, T.G. Mammadov, MirHasan Yu. Seyidov, R.A. Suleymanov. *Sol. St. Comm.* 128 (2003) 25 - 28.

Received: 01.12.2015

## EFFECT OF 2,4 KGRAY ELECTRON IRRADIATION ON ELECTRICAL CHARACTERISTICS OF THE Au/P3HT/n-Si SCHOTTKY DIODE

A. ASİMOV<sup>a</sup>, A. KIRSOY<sup>b</sup>

<sup>a</sup>*Institute of Physics, Academy of Sciences of Azerbaijan,  
G. Javid ave., 131, Baku 1143, Azerbaijan*

<sup>b</sup>*Department of Physics, Faculty of Sciences and Arts, Uludag University,  
16059 Gorukle, Bursa, Turkey*

*Corresponding author: E-mail address: [fizikasimov@gmail.com](mailto:fizikasimov@gmail.com)*

Current-voltage ( $I$ - $V$ ) and capacitance-voltage ( $C$ - $V$ ) characteristics of the unirradiated and irradiated Au/P3HT/n-Si Schottky diode were analyzed. It was seen that the values of the barrier height, the series resistance, and the ideality factor increased after electron irradiation.

The diode parameters such as ideality factor, barrier height, interface state density and series resistance were calculated from the forward  $I$ - $V$  characteristics. The values of the ideality factors for before and after irradiation are calculated as 2.04 and 2.36, respectively. The interface state density  $N_{ss}$  obtained from the forward bias  $I$ - $V$  ranges from  $3.62 \times 10^{11}$  to  $1 \times 10^{12} \text{ cm}^{-2} \text{ eV}^{-1}$  for the unirradiated and  $5.04 \times 10^{11}$  to  $2.07 \times 10^{12} \text{ cm}^{-2} \text{ eV}^{-1}$  for the irradiated situations, respectively.

**Keywords:** Metal semiconductor-structure, conductive polymer, P3HT, electron irradiation.

**PACS:** 68 55 jk.

### 1. INTRODUCTION

The metal-semiconductor (MS) structures are of important applications in the electronics industry. Due to the technological importance of SBDs, a full understanding of the nature of their current-voltage ( $I$ - $V$ ) and capacitance-voltage ( $C$ - $V$ ) characteristics is of greater interest. It is well known that the electrical characteristics of a Schottky diode are controlled mainly by its interface properties [1;2].

Conducting polymers possess chemical and physical properties that exceed those of many other materials. These materials can be used in different condensed matter physics applications, such as organic light-emitting diodes, organic field effect transistors, Schottky diodes, photovoltaic and solar cells. P3HT has been one of the most studied conducting polymers because of its physical and electrical properties, ease and cheapness of fabrication. P3HT has specific properties such as a good mechanical flexibility, high hole mobility and is stable in the atmosphere. The conducting polymer interfacial layer in metal-polymer-semiconductor (MPS) structures play an important role on the determination of the main electrical and dielectric parameters [3-7].

The presence of the polymer interface layer makes them rather sensitive to irradiation. These devices are exposed to high-level radiation, significant changes can occur in their electrical characteristics. Therefore, it is of interest to investigate the damage defect centers introduced by irradiation and to study their effect on the performance of these types of semiconductor devices. In this work, we present results of a study on the effect of irradiation on the electrical characteristics of an Au/P3HT/n-Si Schottky barrier diode (SBD).

The characteristics of the Au/P3HT/n-Si SBD, before and after irradiation, were investigated using current-voltage ( $I$ - $V$ ), capacitance-voltage ( $C$ - $V$ ) measurement techniques.

### 2. EXPERIMENTAL PROCEDURES

n-type Si semiconductor wafer with (100) orientation and 280  $\mu\text{m}$  thickness was used before making contacts, the wafer was chemically cleaned using the RCA cleaning procedure (i.e. 10 min boil in  $\text{H}_2\text{SO}_4 + \text{H}_2\text{O}_2$  followed by a 10 min  $\text{HCl} + \text{H}_2\text{O}_2 + 6\text{H}_2\text{O}$  at  $60^\circ\text{C}$ ). It was immersed in diluted 20% HF for 60 s. The wafer was rinsed in de-ionized water of resistivity 18  $\text{M}\Omega \text{ cm}$  with ultrasonic cleaning in each step. Finally, the sample was dried by exposing the surfaces to high-purity nitrogen. The ohmic contact with a thickness of  $\sim 1500 \text{ \AA}$  was made by evaporating 99.9% purity Au metal on the back surface of the n-Si substrate, then was annealed at  $550^\circ\text{C}$  for 3 min in  $\text{N}_2$  atmosphere. Front surface of samples were coated with a conducting polymer poly(3-hexylthiophene) (P3HT) (fig.1) film by spin coating (VTC-100) with 1200 rpm for 60 s.

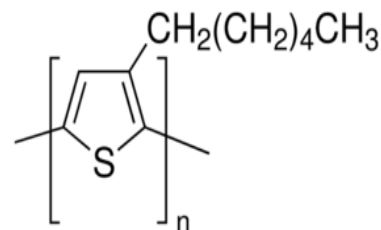


Fig. 1. Molecular structure of P3HT.

After that rectifier Schottky contacts were formed on the other faces by evaporating  $\sim 2000 \text{ \AA}$  thick Au. All evaporation processes were carried out in a vacuum coating unit at about  $5.1 \times 10^{-6} \text{ Torr}$ . Thus, Au/P3HT/n-Si/Au sandwich Schottky barrier type diode was fabricated. The  $I$ - $V$  measurements were performed using a Keithley 6517A electrometer and  $C$ - $V$  measurements were carried out at room temperature with a Keithley HP-4194  $C$ - $V$  Analyzer.

All measurements were controlled by a computer via an IEEE-488 standard interface so that the data collecting, processing and plotting could be accomplished automatically.

### 3. RESULTS AND DISCUSSION

#### 3.1. Current–Voltage Characteristics of Au/P3HT/n-Si Schottky Barrier Diode

The experimental  $I$ – $V$  data are analyzed by the well-known TE equation at forward bias [1,2]:

$$I = I_0 \exp\left(\frac{qV}{nkT}\right) \left[1 - \exp\left(\frac{-q}{kT}V\right)\right] \quad (1)$$

where  $I$  is the measured current,  $V$  is the applied voltage,  $q$  is the electronic charge,  $n$  is the ideality factor that describes the deviation from the ideal diode equation for reverse bias as well as forward bias,  $k$  is the Boltzmann's constant,  $T$  is the absolute temperature in Kelvin,  $I_0$  is the saturation current derived from the straight line intercept of  $\ln I$  at zero-bias and is given by

$$I_0 = AA^*T^2 \exp\left(-\frac{q\Phi_{b0}}{kT}\right) \quad (2)$$

where  $q$  is the electronic charge,  $A$  the effective diode area,  $A^*$  is the effective Richardson constant and equals  $120 \text{ A cm}^{-2}\text{K}^{-2}$  for n-type Si,  $k$  is the Boltzmann constant,  $T$  is the temperature,  $\Phi_{b0}$  ( $I$ – $V$ ) is the zero bias barrier height and  $n$  is the ideality factor. From Eq. (1), ideality factor  $n$  can be written as

$$n = \frac{q}{kT} \left( \frac{dV}{d(\ln J)} \right) \quad (3)$$

$n$  equals to one for an ideal diode. However,  $n$  has usually a value greater than unity.

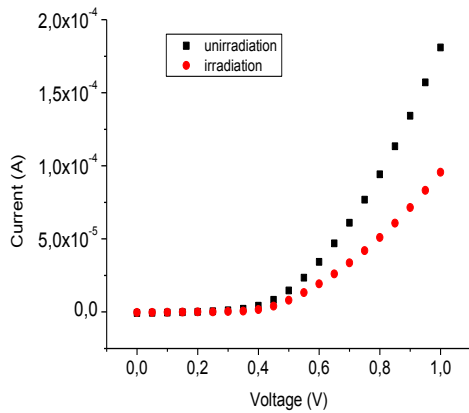


Fig. 2. The current-voltage characteristics of the Au/P3HT/n-Si Schottky diode.

$\Phi_b$  is the zero-bias barrier height (BH), which can be obtained from the following equation

$$\Phi_b = \frac{kT}{q} \ln\left(\frac{AA^*T^2}{I_0}\right) \quad (4)$$

The values of the ideality factor and the barrier heights have been calculated. The values of the barrier heights for before and after irradiation (2.4 kGray) are calculated as 0.77 and 0.80 eV, respectively. Furthermore, the values of the ideality factors for before and after irradiation are calculated as 2.04 and 2.36, respectively. It is seen that the values of the ideality factor has increased after irradiation. Due to electron irradiation, the defects can be created in the crystal lattice and this causes an increase in the ideality factor. The higher values of the  $n$  may be attributed to either recombination of electrons and holes in the depletion region, inhomogeneities of P3HT film thickness or the increase of the diffusion current due to increasing the applied voltage. The irradiation of materials by high-energy particles is known to introduce lattice defects and the semiconductor properties are sensitive to defect concentrations [15,16].

The both forward bias  $I$ – $V$  characteristics of the Schottky diode are linear but deviate considerably from the linearity due to some factors at large voltages, one of the factors is series resistance ( $R_s$ ). The series resistance ( $R_s$ ) of diode are important parameters which influence the performance of the diode. The  $R_s$  values have been calculated by using a method developed by Cheung and Cheung [12]. Cheung's function has been defined as

$$H(I) = V - n \left( \frac{kT}{q} \right) \ln\left(\frac{I_0}{AA^*T^2}\right) \quad (5)$$

$$H(I) = IR_s + n\Phi_b \quad (6)$$

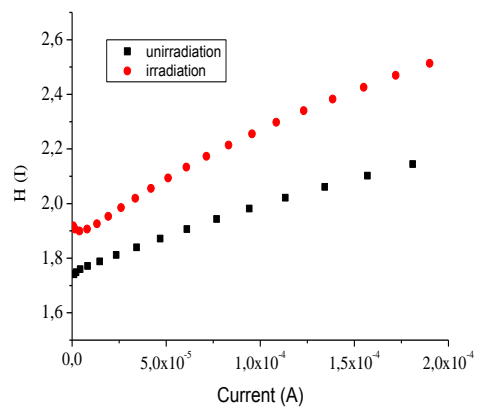


Fig. 3. The  $H(I)$  vs.  $I$  curves of the Au/P3HT/n-Si/Au Schottky diode.

The  $H(I)$  vs.  $I$  curves are shown in fig. 3. The  $R_s$  and  $\Phi_{b0}$  values were calculated from the slope and intercept of  $H(I)$  versus  $I$  plot and were found to be  $2241 \Omega$  and 0.85 eV, respectively. This is considerable higher due to the series resistance and the film properties of conducting polymer P3HT.

Furthermore, Norde proposed an alternative method to determine value of the series resistance. The following function has been defined by the modified Norde's method [13]:

$$F(V) = \frac{V}{\gamma} - \left( \frac{kT}{q} \right) \ln \left( \frac{I}{AA * T^2} \right) \quad (7)$$

where  $\gamma$  is the first integer (dimensionless) greater than  $n$ . That is, according to our results, the value of  $\gamma$  is 4. The  $I(V)$  is the value of current taken from the  $I$ - $V$  curve. Once the minimum of the  $F$  versus  $V$  plot is determined, the value of barrier height can be obtained from Eq. (8).

$$\Phi_b = F(V_0) + \frac{V_0}{2} - \frac{kT}{q} \quad (8)$$

where  $F(V_0)$  is the minimum point of  $F(V)$  and  $V_0$  is the corresponding voltage. Fig. 5 shows the  $F(V)$ - $V$  plots of the device. The value of the series resistance has been obtained from Norde's method by using Eq. (9):

$$R = \frac{kT(\gamma - n)}{qI_0} \quad (9)$$

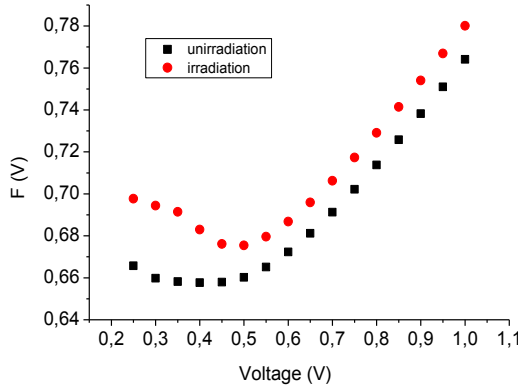


Fig.4.  $F(V)$  vs.  $V$  plots of the Au/P3HT/n-Si/Au Schottky diode for unirradiated and irradiated cases.

From the  $F$ - $V$  plot the values of  $\Phi_b$  and  $R_s$  of the structure were determined as 0.77 eV and  $4.28 \times 10^6$  Ohm for the unirradiated diode, and as 1.01 eV and  $7.77 \times 10^6$  Ohm for the irradiated case, respectively. It was seen that the values of  $R_s$  obtained from both Cheung and Norde methods increased by the applied electron radiation. An increase in series resistance indicates that the reason is either products of the mobility and the free carrier concentration have reduced or the compensation of doping in the semiconductor [15].

The reduction in mobility is due to the introduction of defect centers on irradiation, which act as scattering centers [16].

The interface states between the organic semiconductor compound and inorganic semiconductor play an important role in the determination of the characteristic parameters of the devices. The density of the

interface state proposed by Card and Rhoderick [14] is given by

$$N_{ss}(V) = \frac{1}{q} \left\{ \frac{\epsilon_i}{\delta} [n(V) - 1] - \frac{\epsilon_s}{W_D} \right\} \quad (10)$$

where  $N_{ss}$  is the density of the interface states,  $\delta$  is the thickness of interfacial layer,  $W_d$  is the space charge width, and  $n(V) = (V/(kT/q)) \ln(I/I_0)$  is the voltage-dependent ideality factor  $\epsilon_s = 11.8\epsilon_0$  and  $\epsilon_i = 3\epsilon_0$  are the permittivity of the semiconductor and conducting polymer (P3HT), respectively. In n-type semiconductors, the energy of the interface states  $E_{ss}$  with respect to the bottom of the conduction band at the surface of the semiconductor is given by

$$E_c - E_{ss} = q(\Phi_b - V_D) \quad (11)$$

where  $V_D$  is the applied voltage drop across the depletion layer and  $\Phi_b$  is the effective barrier height.  $N_{ss}$  values are obtained via Eq.(10). The energy distribution profiles of  $N_{ss}$  of Schottky diode were obtained from the experimentally forward bias  $I$ - $V$  measurements before and after irradiation and are given in fig. 5. As can be seen in the figure, exponential growth of the interface state density towards the top of the valance band is very apparent. The interface states,  $N_{ss}$ , have been decreased significantly after electron irradiation. The interface state density  $N_{ss}$  obtained from the forward bias  $I$ - $V$  ranges from  $3.62 \times 10^{11}$  to  $1 \times 10^{12}$   $\text{cm}^{-2}\text{eV}^{-1}$  for the unirradiated and  $5.04 \times 10^{11}$  to  $2.07 \times 10^{12}$   $\text{cm}^{-2}\text{eV}^{-1}$  for the irradiated situations, respectively. These changes have been attributed to the decrease in recombination centre and the existence of polymer layer.

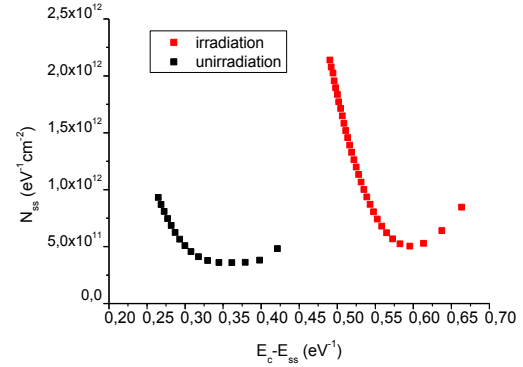


Fig. 5.  $N_{ss}$  vs.  $E_{ss}-E_v$  plots of the Au/P3HT/n-Si Schottky diode for unirradiated and irradiated cases.

### 3.2. Analysis of Capacitance–Voltage Characteristics of Au/P3HT/n-Si Schottky Barrier Diode

Capacitance–voltage ( $C$ - $V$ ) measurement is one of the most popular electrical measurement techniques used to characterize a Schottky type device.  $C$ - $V$  curves of Au/P3HT/n-Si device were plotted at 100 kHz (fig. 6). Figure shows a typical  $C$ - $V$  relation obtained from the measurement at 100 kHz frequency and room temperature before and after irradiation. As shown in fig. 6, the values of capacitance decrease regularly with increasing applied bias voltage.

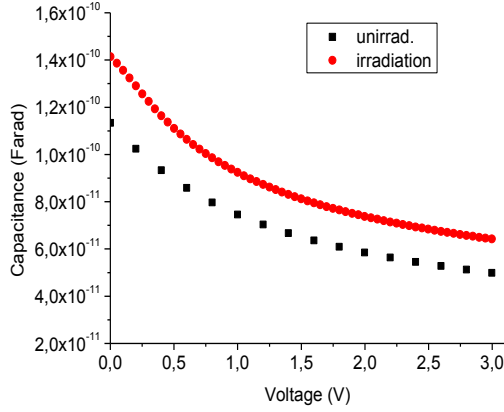


Fig. 6. The forward and reverse bias  $C$ - $V$  characteristics of the Au/P3HT/n-Si Schottky diode for unirradiated and irradiated cases.

In rectifying contacts the depletion layer capacitance is given as follows [2]

$$\frac{dC^{-2}}{dV} = \frac{2(V_d + V)}{q\epsilon_s A^2 N_D} \quad (12)$$

where  $\epsilon_s$  is the dielectric constant of semiconductor,  $A$  is the effective diode area,  $V_d$  is the intercept voltage and is determined from the extrapolation of the linear  $1/C^2$ - $V$  plot to the  $V$  axis,  $\epsilon_s$  is the dielectric constant of the semiconductor ( $11.7 \epsilon_o$  for n-type Si) and  $N_D$  is the donor concentration of the n-semiconductor substrate. The barrier height value can be determined from the relation:

$$\Phi_b(C-V) = V_d + E_F \quad (13)$$

where  $E_F$  is the energy difference between the bulk Fermi level and valance band edge, and is given by

$$E_F = \frac{kT}{q} \ln\left(\frac{N_C}{N_D}\right) \quad (14)$$

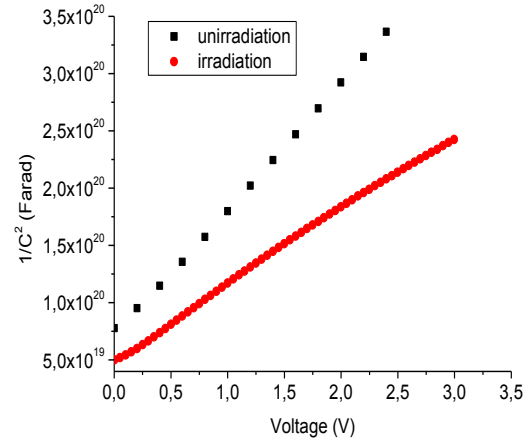


Fig. 7. The reverse bias  $C^{-2}$ - $V$  characteristics of the before and after irradiation at 100 kHz frequency.

In fig. 7, the  $C^{-2}$ - $V$  plot is presented for 100kHz frequency. It can be seen from the reverse bias  $C^{-2}$ - $V$  figures that these curves are linear. The values of  $N_D$  and  $\Phi_b$  for Au/P3HT/n-Si SBD were found as  $2.5 \times 10^{16} \text{ cm}^{-3}$  and 1 eV before irradiation, and  $3.07 \times 10^{15} \text{ cm}^{-3}$  and 0.97 eV after irradiation, respectively. It is clear that, these values were strongly dependent of radiation. The values of the barrier heights extracted from the  $C$ - $V$  curves are higher than that derived from the  $I$ - $V$  measurements. This difference can explained due to nonuniformity of the interfacial P3HT layer thickness or the effect of the image force and the barrier inhomogeneities.

#### 4. CONCLUSION

In conclusion, we have investigated the electrical parameters of the Au/P3HT/n-Si SBDs by using  $I$ - $V$  and  $C$ - $V$  characteristics under irradiation at room temperature. The electronic parameters such as ideality factor, barrier height and series resistance of the Schottky diode were extracted by forward-bias  $I$ - $V$ , Cheung's functions and Norde's functions. The values of the barrier heights for before and after irradiation (2.4 kGray) are calculated as 0.77 and 0.80 eV, respectively. Furthermore, the values of the ideality factors for before and after irradiation are calculated as 2.04 and 2.36, respectively.

- [1] S.M. Sze. Physics of Semiconductor Devices, 2nd ed., John Wiley, New York,(1981).
- [2] E.H. Rhoderick, R.H. Williams. Metal-Semiconductor Contact, Clarendon, Oxford,(1988).
- [3] F. Padinger, R.S. Rittberger, N.S. Sariciftci. Adv. Funct. Mater. 13 (2003) 85.
- [4] F. Yakuphanoglu, M. Shah and W. Aslam Farooq. A. Phys. Polonica A 120 (2011) 3.
- [5] E. Voroshazi, B.Verreet, T.Aernouts, P.Heremans. Solar Energy Mater. Solar Cells 95 (2011) 1303-1307.
- [6] M. Manceau, A.Rivaton, J.-L.Gardette, S.Guillerez, N.Lemaître. Solar Energy Mater. Solar Cells 95(2011)1315-1325.
- [7] O. Güllü, S. Aydoğan, A. Türüt. Microelectron. Eng. 85 (2008) 1647.
- [8] G.A. Umana-Membreno, J.M. Dell, G. Parish, B.D. Nener, L. Faraone, U.K. Mishra. IEEE Trans. Electron Devices 50 (2003) 12.
- [9] S.A. Goodman, F.D. Aurret, M. du, Plessis, W.E. Meyer. Semicond. Sci. Technol.14 (1999) 323.
- [10] S. Gupta, M. Muralikiran, J. Farmer, L.R. Cao, R.G. Downing. J. Mater. Res. 24 (2009) 1498-1512.
- [11] S.K. Cheung, N.W. Cheung, Appl. Phys. Lett. 49 (1986) 85.
- [12] T. Kilicoglu. Thin Solid Films (2008);516:967.
- [13] H. Norde. J. Appl. Phys.(1979);50:5052.
- [14] H.C. Card, E.H. Rhoderick. J. Phys. D: Appl. Phys. 4 (1971) 1589.



- [15] *İ. Dökme, P. Durmuş, Ş. Altındal.* Nuclear Instruments and Methods in Physics Research B 266 (2008) 791–796.
- [16] *Ş. Aydoğan, A.Türüt.* Radiation Physics and Chemistry 80 (2011) 869–875.
- [17] *S. Krishnan, G. Sanjeev, M. Pattabi.* Nuclear Instruments and Methods in Physics Research B 266 (2008) 621–624.

*Received: 22.10.2015*

# NEUTRINO-ANTINEUTRINO PAIRS RADIATION BY TRANSVERSELY POLARIZED ELECTRONS IN STRONGLY MAGNETIZED MEDIUM

RASMIYYA E. GASIMOVA

*Shamakhy Astrophysical Observatory National Academy of Sciences of Azerbaijan,  
Y. Mammadaliyev Settlement, Shamakhy District, AZ5618, Azerbaijan;  
Baku State University, Z. Khalilov 23, AZ 1148, Baku, Azerbaijan;  
Qafqaz University, Baku-Sumgayit Road, 16 km., Khirdalan, Baku, AZ0101, Azerbaijan;  
E-mail: gasimovar@yahoo.co.uk*

It is determined that when the energies of the emitted neutrinos and antineutrinos are extremely close to each other, the neutrino synchrotron radiation by the transversely polarized electrons is amplified and the processes possess the resonance character. When the spins of the initial electrons are oriented along the magnetic field direction, the spectral and angular distribution of the energy loss transported from the unit volume of the medium per unit time does not depend on neutrino flavour and each of the processes  $e^- \rightarrow e^- \nu_e \tilde{\nu}_e$ ,  $e^- \rightarrow e^- \nu_\mu \tilde{\nu}_\mu$  and  $e^- \rightarrow e^- \nu_\tau \tilde{\nu}_\tau$  contributes to the cooling of the strongly magnetized hot stars equally.

**Keywords:** electron, neutrino synchrotron radiation, energy loss, magnetic field, ground Landau level, first Landau level.

**PACS:** 13.15.+g, 13.88.+e.

## INTRODUCTION

In the superstrong magnetic fields with the strengths  $H \geq H_0 = m_e^2 c^3 / e \hbar = 4,41 \times 10^{13} \text{ G}$  electrons are mainly occupy the low Landau levels. In such magnetic fields the energy gained by electrons is in order of the electron rest mass and even higher than its rest mass. In this case it is necessary to take into account the field and spin (polarization) effects. Superstrong magnetic fields are met in strongly magnetized astrophysical objects and processes [1-16]. In terrestrial conditions superstrong magnetic fields are produced in heavy ion collisions [17-23]. Possible existence of the superstrong magnetic fields with the strengths higher than  $\sim 10^{20} \text{ G}$  [24-34] and production of such fields in cosmic objects and phenomena [26-28, 31] are not excluded. Investigation of various interaction processes of high energy particles in intense magnetic fields has great importance for both particle physics and astrophysics. The effective mechanism of transportation of internal energy of strongly magnetized hot stars to surroundings is not realized by photons, but it realized by neutrinos and antineutrinos. One of the main processes taking a great importance in cooling of strongly magnetized hot stars is so called the neutrino synchrotron radiation by electrons [35, 36]. The neutrino synchrotron radiation by electrons is described by the reaction

$$e^- \rightarrow e^- + \nu_i + \tilde{\nu}_i \quad (1)$$

where  $\nu_i$  ( $\tilde{\nu}_i$ ) are the neutrino flavours:  $\nu_i = \nu_e, \nu_\mu, \nu_\tau$  and  $\tilde{\nu}_i = \tilde{\nu}_e, \tilde{\nu}_\mu, \tilde{\nu}_\tau$ . When we have dealings with  $\nu_e$  and  $\tilde{\nu}_e$ , both the neutral and charged currents contribute to the processes (1). However, when we have dealings with  $\nu_\mu$  and  $\tilde{\nu}_\mu$  or  $\nu_\tau$  and  $\tilde{\nu}_\tau$ , the neutral currents only contribute to the processes (1).

The purpose of this work is to investigate the energy

loss per unit time per unit volume by the transversely polarized electrons occupying the first Landau level in the processes (1) in strongly magnetized hot medium with allowance for the temperature and the chemical potential of the medium, to obtain the formula enabling us to calculate the energy loss, to clarify the role of the polarization effects and to determine the astrophysical applications of the obtained results. We investigate the considered processes for the small momentum transferred, i.e. for the case when  $|q_z|^2 \ll m_Z^2$  and  $|q_w|^2 \ll m_w^2$ ,

where  $m_Z$  is the Z - boson mass and  $m_w$  is the W - boson mass. Although the experimental confirmation of neutrino oscillations [37-39] is evident for the existence of the small mass of neutrinos, the estimations indicate the upper boundary of the neutrino mass  $m_\nu < 2 \text{ eV}$  [40].

The value of the neutrino mass is much smaller than the electron mass and the Z - boson (W - boson) mass. At the same time the characteristic energy of neutrinos (antineutrinos) considered here is much greater than the neutrino mass. All these enable us to apply the massless neutrino approximation. Contribution of the electromagnetic interaction of the possible anomalous magnetic moment of a neutrino with the magnetic field can be neglected for the observable strengths of the known magnetized stars. In the presented work we use the pseudo-euclidean metrics with the signature  $(+---)$  and the system of units  $\hbar = c = k_B = 1$ , where  $k_B$  is the Boltzmann constant.

## SPECTRAL AND ANGULAR DISTRIBUTION OF ENERGY LOSS TRANSPORTED FROM UNIT VOLUME OF THE MEDIUM PER UNIT TIME

Using the Feynman rules for weak processes [41] and the method of exact solution of the relativistic wave equations (here we mean the Dirac equation) in a constant uniform magnetic field [42] we obtain the following

formula for the spectral and angular distribution of the energy loss transported from the unit volume of the medium per unit time with allowance for the temperature

$$Q = \frac{d^4 W}{d\omega d\omega' d\Omega d\Omega'} = (2\pi)^{-7} G_F^2 eH \sum_{n=1}^{\infty} \sum_{n'=0}^{\infty} \sum_i \frac{E_i E'_i}{|E'_i p_{zi} - E_i p'_{zi}|} f(1-f') \omega^2 \omega'^2 (\omega + \omega') R_0, \quad (2)$$

where  $G_F$  is the Fermi constant,  $H$  is the strength of the magnetic field which is assumed to be directed along the  $z$ -axis,  $E_i(E'_i)$  and  $p_{zi}(p'_{zi})$  are energy and the third component of the initial (final) electrons, respectively,  $f$  and  $f'$  are the Fermi-Dirac distribution functions of the initial and final electron gases, respectively,  $\omega$  and  $\omega'$  are the energies of the antineutrino and the neutrino emitted by the initial electron, respectively,  $R_0$  is the quantity obtained from the absolute value of the squared amplitude (or squared matrix element) of the considered processes.  $E_i$  and  $E'_i$  are the roots of the equation  $E = E' + \omega + \omega'$  that expresses the energy conservation law.  $p_{zi}$  and  $p'_{zi}$  are the roots of the equation  $p_z = p'_z + k_z + k'_z$  that expresses the conservation law of the third component of momentum.

We are interested in investigation of the considered problem in the cases when the neutrinos and the antineutrinos are emitted in the magnetic field direction (along the field direction and/or opposite to the field direction). We have four cases in this situation: 1)  $\mathcal{G} = 0$ ,  $\mathcal{G}' = 0$  (the antineutrinos and the neutrinos are emitted

and the chemical potential of the medium when the transversely polarized initial electrons occupy the first Landau level

along the magnetic field direction); 2)  $\mathcal{G} = \pi$ ,  $\mathcal{G}' = \pi$  (the antineutrinos and the neutrinos are emitted opposite to the magnetic field direction); 3)  $\mathcal{G} = 0$ ,  $\mathcal{G}' = \pi$  (the antineutrinos are emitted along the magnetic field direction and the neutrinos are emitted opposite to the magnetic field direction); 4)  $\mathcal{G} = \pi$ ,  $\mathcal{G}' = 0$  (the antineutrinos are emitted opposite to the magnetic field direction and the neutrinos are emitted along the magnetic field direction), where  $\mathcal{G}$  and  $\mathcal{G}'$  are the polar angles of the antineutrino momentum and the neutrino momentum, respectively. The straightforward calculations show that when the transversely polarized electrons lying on the first Landau level make transitions to the ground Landau level at the expense of neutrino-antineutrino pairs emission, the differential probability of the processes and the energy loss per unit time per unit volume are equal to zero in all cases except the third case:  $\mathcal{G} = 0$ ,  $\mathcal{G}' = \pi$ . It means that when the transversely polarized electrons lying on the first Landau level make transitions to the ground Landau level at the expense of neutrino-antineutrino pairs emission, the antineutrinos are emitted along the magnetic field direction and the neutrinos are emitted opposite to the magnetic field direction. For this case we obtain the following formula for the spectral and angular distribution of the energy loss

$$Q = (2\pi)^{-7} G_F^2 eH \omega^2 \omega'^2 (\omega + \omega') \frac{E}{p_z} R_0 f(1-f'). \quad (3)$$

The quantity  $R_0$  is determined by the expression

$$R_0 = 2 \left( 1 + \zeta \frac{m_e}{E_{\perp}} \right) \left[ g_+ - g_- \zeta \sqrt{1 - \left( \frac{p_z}{E} \right)^2} - 2g_{\perp} \frac{p_z}{E} \right], \quad (4)$$

where  $\zeta$  is the projection of the spin of the initial electron along the magnetic field direction ( $\zeta = +1$ ) or opposite to the magnetic field direction ( $\zeta = -1$ ),  $p_z = \omega - \omega'$  is the third component of the initial electron momentum,  $m_e$  is the electron mass,  $E$  is the energy of the initial electron occupying the first Landau level

$$E = \sqrt{m_e^2 + 2eH} + (\omega - \omega')^2, \quad (5)$$

$$E_{\perp} = \sqrt{m_e^2 + 2eH}, \quad (6)$$

$$g_{\nu} = \pm \frac{1}{2} + 2 \sin^2 \mathcal{G}_{\nu}, \quad (7)$$

$$g_A = \pm \frac{1}{2}. \quad (8)$$

The notation “ $\pm$ ” in the expressions (7) and (8) has the following meanings: the sign “ $+$ ” corresponds to the processes (1) proceeding via both the neutral and charged currents, the sign “ $-$ ” corresponds to the processes (1) proceeding via only the neutral currents.

Participation of the spin quantum number  $\zeta$  in the expression (4) indicates that the spectral and angular distribution of the energy loss transported from the unit volume of the medium per unit time depends on the polarizations of the spins of the initial electrons. When the energies of the emitted neutrinos and antineutrinos are extremely close to each other, the neutrino synchrotron radiation by the electrons is amplified and the processes possess the resonance character. When the initial electrons have superhigh energies and the energies of the emitted

neutrinos and antineutrinos are enough close to each other but their difference is not equal to zero, we can write the following relation

$$\frac{p_z}{E} = \frac{\omega - \omega'}{E} \ll 1 \quad (9)$$

and neglect the terms proportional to  $p_z/E$  in the expression (4). So, we obtain the following simple expression for  $R_0$ :

$$R_0 = 2 \left( 1 + \zeta \frac{m_e}{E_\perp} \right) (g_+ - g_- \zeta). \quad (10)$$

Hereafter we are interested in the case when the spins of the initial electrons are oriented along the magnetic field direction ( $\zeta = +1$ ). Using the expression (3) and (10) we obtain the following formula for the spectral and angular distribution of the energy loss transported from the unit volume of the medium per unit time when the spins of the initial electrons are oriented along the magnetic field direction ( $\zeta = +1$ ):

$$Q = \frac{G_F^2}{32\pi^7} g_A^2 e H \omega^2 \omega'^2 \frac{\omega + \omega'}{\omega - \omega'} \left( \sqrt{m_e^2 + 2eH} + m_e \right) f(1 - f'), \quad (11)$$

where the multiplier  $f(1 - f')$  constructed from the Fermi-Dirac distribution functions of the initial electrons and final electrons is determined as follows

$$f(1 - f') = \left\{ \exp \left[ \left( \sqrt{m_e^2 + 2eH} - \mu \right) / T \right] + 1 \right\}^{-1} \left\{ \exp \left[ (m_e - \mu) / T' \right] + 1 \right\}^{-1} \exp \left[ (m_e - \mu) / T' \right], \quad (12)$$

$\mu$  is the chemical potential of the electron gas,  $T$  is the temperature of the gas consisting of the electrons occupying the first Landau level (the temperature of the electron gas before the neutrino pairs radiation) and  $T'$  is the temperature of the gas consisting of the electrons occupying the ground Landau level (the temperature of the electron gas after the neutrino pairs radiation).

Presence of the multiplier  $g_A^2$  in the formula (11) and the definition (8) enable us to come to the conclusion that when the spins of the initial electrons are oriented along the magnetic field direction, the spectral and angular distribution of the energy loss transported from the unit volume of the medium per unit time does not depend on neutrino flavour and each of the processes  $e^- \rightarrow e^- \nu_e \tilde{\nu}_e$ ,  $e^- \rightarrow e^- \nu_\mu \tilde{\nu}_\mu$  and  $e^- \rightarrow e^- \nu_\tau \tilde{\nu}_\tau$  contributes to the

cooling of the strongly magnetized hot stars equally.

## CONCLUSIONS

We determined that when the energies of the emitted neutrinos and antineutrinos are extremely close to each other, the neutrino synchrotron radiation by the transversely polarized electrons is amplified and the processes possess the resonance character. When the spins of the initial electrons are oriented along the magnetic field direction, the spectral and angular distribution of the energy loss transported from the unit volume of the medium per unit time does not depend on neutrino flavour and each of the processes  $e^- \rightarrow e^- \nu_e \tilde{\nu}_e$ ,  $e^- \rightarrow e^- \nu_\mu \tilde{\nu}_\mu$  and  $e^- \rightarrow e^- \nu_\tau \tilde{\nu}_\tau$  contributes to the cooling of the strongly magnetized hot stars equally.

- 
- [1] V.M. Lipunov. *Astrofizika neytronnix zvezd*. M.: Nauka, (1987) 296.
  - [2] P. Meszaros. *High-energy radiation from magnetized neutron stars*, Chicago: University of Chicago Press, (1992).
  - [3] R.C. Duncan, C. Thompson. *Astrophys. J. Lett.*, 392 (1992) L9-L13.
  - [4] C. Thompson, R.C. Duncan. *Mon. Not. R. Astron. Soc.*, 275 (1995) 255-300.
  - [5] C. Kouveliotou, R.C. Duncan, C. Thompson. *Scientific American*, 288, No2 (2003) 24-31.
  - [6] J.S. Heyl, S.R. Kulkarni. *Astrophys. J.*, 506 (1998) L61-L64.
  - [7] R.N. Manchester, G. B. Hobbs, A. Teoh, M. Hobbs. *Astron. J.*, 129 (2005) 1993-2006.
  - [8] G.S. Bisnovatyi-Kogan, Yu.P. Popov, A.A. Samochin. *Astrophys. and Space Sciences*, 41 (1976) 287-320.
  - [9] G.S. Bisnovatyi-Kogan. *Workshop on Frontier Objects in Astrophysics and Particle Physics (Vulcano Workshop, 23-28 May 1994)*, Vulcano, Italy, (1994) 443-449.
  - [10] S.W. Bruenn. *Astrophys. J. Suppl. Ser.*, 58 (1985) 771-841.
  - [11] J. LeBlanc, J.R. Wilson. *Astrophys. J.*, 161 (1970) 541-551.
  - [12] A. Mezzacappa, S.W. Bruenn. *Astrophys. J.*, 405 (1993) 669-684.
  - [13] M. Rampp, H.T. Janka. *Astrophys. J.*, 539 (2000) L33-L36.
  - [14] V.V. Usov. *Nature (London)*, 357 (1992) 472-474.
  - [15] J.I. Katz. *Astrophys. J.*, 490 (1997) 633-641.
  - [16] M.A. Ruderman, L. Tao, W. Kluzniak. *Astrophys. J.*, 542 (2000) 243-250.
  - [17] V. Skokov, A.Y. Illarionov, V. Toneev. *Int. J. Mod. Phys. A*, 24 (2009) 5925.

- [18] W. -T. Deng, X. -G. Huang. Phys. Rev. C, 85 (2012) 044907.
- [19] A. Bzdak, V. Skokov. Phys. Lett. B, 710 (2012) 171-174.
- [20] D.E. Kharzeev, L.D. McLerran, H.J. Warringa. Nucl. Phys. A, 803 (2008) 227-253.
- [21] M.N. Chernodub. Phys. Rev. D, 82 (2010) 085011.
- [22] M.N. Chernodub. Phys. Rev. Lett., 106 (2011) 142003.
- [23] M.N. Chernodub. Lect. Notes Phys., 871 (2013) 143-180.
- [24] M. Bander, H. Rubinstein. Phys. Lett. B, 280 (1992) 121-123.
- [25] M. Bander, H. Rubinstein. Phys. Lett. B, 289 (1992) 385.
- [26] E. Witten. Nucl. Phys. B, 249 (1985) 557.
- [27] E.M. Chudnovsky, G.B. Field, D.N. Spergel, A. Vilenkin. Phys. Rev. D, 34 (1986) 944.
- [28] S. Kawati, A. Kokado. Phys. Rev. D, 39 (1989) 3612.
- [29] D. Grasso, H. Rubinstein. Phys. Report, 348 (2001) 163.
- [30] A. Shabad, V. Usov. Phys. Rev. Lett., 96 (2006) 180401.
- [31] A. Shabad, V. Usov. Phys. Rev. D, 73 (2006) 125021.
- [32] A. Shabad, V. Usov. Phys. Rev. Lett., 98 (2007) 180403.
- [33] A. Shabad, V. Usov. Phys. Rev. Lett., 99 (2007) 228902.
- [34] S. Chakrabarty *et al.* Phys. Rev. Lett., 78 (1997) 2898.
- [35] A.A. Kaminker, D.Q. Yakovlev. JETP, 1993, t. 103, s.438-454. (In Russian)
- [36] R.E. Gasimova, V.A. Huseynov, Y.T. Shukurova. Proceedings of the XXIV International Symposium on Lepton Photon Interactions at High Energies. (Hamburg, Germany, 17-22 August 2009), Hamburg, 2010. Edited by T. Behnke and J. Mnich. Hamburg, Germany, DESY, pp.481-483.
- [37] Q.R. Ahmad *et al.* (SNO Collaboration). Phys. Rev. D, 2001, v.87, No7, p.071301.
- [38] Q.R. Ahmad *et al.* (SNO Collaboration). Phys. Rev. Lett., 2002, v.89, p.011301.
- [39] Y. Fukuda *et al.* (Super-Kamiokande Collaboration). Phys. Rev. Lett., 1998, v.81, pp.1562-1567.
- [40] K.A. Olive *et al.* (Particle Data Group), Chin. Phys. C, 38, 090001 (2014) and 2015 update.
- [41] A.A. Sokolov, I.M. Ternov, V.Ch. Jukovskiy, A.B. Borisov. Kalibrovocnie polya. M.: Izd-vo Moskovskoqo universiteta, 1986, 260 s. (In Russian).
- [42] A.A. Sokolov, I.M. Ternov. Relyativstkiy elektron. M.: Nauka, (1983) 304. (In Russian).

*Received: 18.11.2015*



## CONFORMATION PROPERTIES OF HIS1-ALA2-ILE3-TYR4-PRO5-ARG6-HIS7 MOLECULE

G.D. ABBASOVA, E.Z. ALIYEV

*Baku State University, Z. Khalilov str., 23, Baku, Az-1148*

The spatial structure, electron-conformation properties and molecular dynamics of T7 peptide being the linear sequence of seven aminoacid residuals His1-Ala2-Ile3-Tyr4-Pro5-Arg6-His7 (HAIYPRH) are investigated. The calculations of spatial structure is made by means of molecular mechanics method using force field of atom-atom potential functions. The investigations of electron and molecular-dynamic properties of main and side chains consisting in the molecule of aminoacid residuals is carried out under conditions modeling the real water surrounding of peptide molecule. It is established that low-energy states of T7 peptide are stabilized by stable hydrogen bonds within limits of tetra-peptide molecule fragments, which don't destroy in molecular dynamics process. The changes in electron structure with respect to hard fragments in low-energy conformation molecule states are revealed.

**Keywords:** T7 peptide, spatial structure, conformation, low-energy conformation**PACS:** 31.15; 33.15

## INTRODUCTION

Nowadays the investigations of complexes taking part in purposeful transport of medications used in tumor illnesses are actual ones. The works dedicated to study of peptide property, which consists of linear sequence of seven amino-acid residuals His1-Ala2-Ile3-Tyr4-Pro5-Arg6-His7 (HAIYPRH) known as T7 peptide [1] also belong to intensive investigations of last years. T7 peptide is ligand in system activating the transferrin-receptors (TfR) and carrying by the means of endocytosis the delivery of medicines inside the cells affected by cancer. The investigations show that complex including T7 peptide towards the polyamidoamine (PAMAM) and polyethylene glycol (PEG) and further loaded doxorubicin (DOX) are characterized by more high anticancer activity in experiments carried out with white mice under natural conditions [2-6]. On the base of these works, the conclusion is made that peptide T7 plays the key role in transport mechanisms of anticancer medicines inside cells. The spatial structure and dynamic properties of peptide T7 are investigated in present work by molecular mechanics methods based on force field of semiempirical potential functions. The limits of dihedral angle variations in main and side chains of amino-acid residuals forming the peptide structure are established. The values of partial charges on separate atoms and distribution of electron density on functional groups of amino-acid residuals in different molecule conformation states are calculated.

## CALCULATION METHOD

The spatial structure and T7 peptide conformation properties (HAIYPRH) are investigated by the way of search of local minimums of total conformation energy according to technique and calculations described in works [7,8]. To calculate the energy the non-valence ( $E_{nv}$ ) and electrostatic ( $E_{el}$ ) atom interaction, hydrogen ( $E_h$ ) bonds and torsion ( $E_t$ ) contributions are taken under consideration. For description of these interactions the semiempirical potential functions given in work [9] are used. The calculations are carried out in framework of stiff valence scheme, i.e. at fixed values of valence bond lengths and valence angle of aminoacid residuals including in T7

peptide chemical structure. The applied system of potential functions and calculated programs are approved on big number of peptides and proteins by authors of given work and other investigators [10-11]. The minimal values of conformation energy, interresidual interaction contributions and also hydrogen bond system stabilizing the low-energy peptide conformation states are the criterions of stable structure selection. The search of low-energy conformations of molecular system is carried out with help of numerical methods of extremum search of functions of several variables. Moreover it is supposed that molecule native conformation is in region of potential energy global minimum.

The parameterization supposed in work [9] of is used for modeling of water surrounding. The hydrogen bond energy is estimated with help of Morse potential at energy value of hydrogen bond dissociation equal to 1,5kcal/mol corresponding to bond distance  $NH...OC$   $r=1.8\text{\AA}$  for water solutions. The value of dielectric constant equal to 10 is taken. The conventional classification of peptide structures is used at discussion of calculation results [8]. The choice of structural variants at conformation calculation of separate peptides is carried out on the base of known values of dihedral angles ( $\varphi$  and  $\psi$ ) corresponding to low-energy regions of conformation cart R,B,L and P for each single peptide. The counting out of dihedral angles is carried out according to international nomenclature [12].

The molecular dynamics method described in work authors [13-15] is used for study of T7 peptide conformation mobility. The classical motion trajectories of macromolecule atoms are calculated by method using the force field of atom-atom potential functions, i.e. the detail macroscopic picture of molecule internal heat mobility in sub-nano-second time intervals is modeled. The peptide electronic structure, partial charges of atoms, electric density distribution, electric dipole moment and other parameters are investigated by semiempirical method of quantum chemistry RM3. The cutoff radius 12 $\text{\AA}$  is used for calculation speedup of Van-der-Waals, hydrogen and electrostatic interactions. To avoid the undesirable edge effects the peptide chain is added by acetyl residuals in its starting and N-methylamine in its side.

## RESULTS AND THEIR DISCUSSION

According to investigation results of low-energy T7 peptide conformation states belong to structural types of its main chain and are characterized by total conformation energy values varying in interval  $-19,0 \div -25,7$  kcal/mol. They differ by contributions of separate energy components, dihedral rotation angle values in main and side chains of peptide and also hydrogen bond systems stabilizing the stable conformation peptide states (table 1-3). According to investigation results the semi-convoluted structure types

which are approximately on 7 kcal/mol preferable ones than fully unfolded structure types, are the energetically preferable ones. The atom non-valent interactions within the tetra-peptide fragments make the main contributions in stabilization. The hydrogen bonds between peptide chain atoms of His1 and Tyr4, Tyr4 и His7 residuals confirm about this fact. Though the contributions of hydrogen bond energy aren't essential ones (from 0,2 up to 1,2 kcal/mol), so they play the important role in stabilization of stable conformation peptide states.

Table 1.  
Low-energy conformation states of T7 peptide on [7] work data

№	Shape	Form	E <sub>n-v</sub>	E <sub>el</sub>	E <sub>tors</sub>	E <sub>tot</sub>	E <sub>rel</sub>
1	efeefe	B <sub>2</sub> RB <sub>2</sub> B <sub>3</sub> RB <sub>3</sub> B <sub>3</sub>	-34.6	2.2	6.8	-25.7	0.0
2	efeef	B <sub>2</sub> RB <sub>2</sub> B <sub>3</sub> RR <sub>3</sub> R <sub>3</sub>	-33.4	2.5	5.9	-25.0	0.7
3	efeeeee	B <sub>2</sub> RB <sub>2</sub> B <sub>3</sub> BB <sub>3</sub> R <sub>3</sub>	-31.5	2.3	6.1	-23.1	2.6
4	effefe	B <sub>2</sub> RRB <sub>3</sub> RB <sub>3</sub> R <sub>3</sub>	-32.6	3.3	6.5	-22.8	2.9
5	eeefe	B <sub>2</sub> BRB <sub>3</sub> RB <sub>3</sub> R <sub>3</sub>	-29.2	2.8	4.6	-21.9	3.8
6	eeefe	B <sub>2</sub> BB <sub>3</sub> B <sub>3</sub> RB <sub>3</sub> R <sub>3</sub>	-30.0	2.3	6.4	-21.6	4.1
7	fffefe	R <sub>3</sub> RRB <sub>3</sub> RB <sub>3</sub> B <sub>3</sub>	-30.6	3.8	5.9	-20.9	4.8
8	ffefe	R <sub>2</sub> RB <sub>3</sub> B <sub>1</sub> RB <sub>3</sub> B <sub>3</sub>	-30.3	3.4	6.7	-20.2	5.5
9	ffeeef	R <sub>2</sub> RB <sub>3</sub> B <sub>3</sub> BR <sub>3</sub> R <sub>3</sub>	-29.9	3.6	6.2	-20.2	5.6
10	ffeff	R <sub>3</sub> RRB <sub>3</sub> RR <sub>3</sub> R <sub>3</sub>	-29.5	4.3	5.0	-20.1	5.7
11	efeef	B <sub>2</sub> BRB <sub>3</sub> RR <sub>3</sub> R <sub>3</sub>	-27.1	3.3	4.2	-19.6	6.1
12	eeefe	R <sub>2</sub> RB <sub>3</sub> B <sub>3</sub> BR <sub>3</sub> R <sub>2</sub>	-29.5	3.6	6.4	-19.4	6.3
13	ffeff	R <sub>2</sub> RB <sub>3</sub> B <sub>1</sub> RR <sub>3</sub> R <sub>3</sub>	-29.1	3.9	6.1	-19.1	6.5
14	eeefe	B <sub>2</sub> BB <sub>3</sub> B <sub>1</sub> BR <sub>2</sub> B <sub>2</sub>	-28.1	3.1	6.0	-19.0	6.6

The molecular dynamics of T7 peptide in aqueous medium is investigated for investigation of stability separate fragments and whole molecule in conditions modeling the real surrounding water. The calculations with taking under consideration of different low-energy conformation states given in table 1, are carried out in following stages. Firstly, the molecule relaxation is carried out using the force field AMBER during 30 psec. The found energy minimum allows us to put the molecule in volume containing 180 water molecules. Further, the relaxation of molecules is carried out with taking under consideration the real surrounding water of molecules. The atom collision rate  $50\text{psec}^{-1}$  with water molecules is given for imitation of surrounding water.

The structure stability of separate fragments is also confirmed by dihedral angle values in molecule main chain. In peptide molecular dynamics process the  $\phi$  angle inclination values (torsion rotation angle round bond N-C $^{\alpha}$ ) in comparison of its optimal value for His1 vary in interval from  $-40^{\circ}$  to  $+40^{\circ}$ . The maximum inclinations for rotation torsion angle  $\psi$  around bond C $^{\alpha}$ -C' achieve to  $\pm 16^{\circ}$  values. As T7 peptide takes part in fixation with

transferrin-receptors, it is important to reveal not only stable elements of spatial structure but to analyze the change character in atom charges with respect of hard fragments in molecule structure. The values of partial charges of atoms and distances between oxygen atoms of peptide groups of spatially connivent amino-acid residuals in different peptide conformation states calculated by means of quantum chemistry semiempirical method RM3 are given in tables 4 and 5.

As it is followed from calculation results the partial charge values practically don't change except only of oxygen atoms of peptide groups Ala2 and Pro5 whereas the charges of peptide chain atoms of other amino-acid residuals vary in  $\pm 0,5$  charge units.

According to carried out investigations it has been concluded that stable conformation states of T7 peptide consist in the relatively hard fragments which form the cavity with negatively charged oxygen atoms taking part in complex formation processes with transferrin-receptors. Hys1(O)-Ile3(O) oxygen atoms are the more connivent, the distances between which vary in  $4,5 \div 6,3$  Å and Tyr4(O)-Arg6(O) where these distances between them are  $5,5 \div 6,4$  Å.

Table 2.

The dihedral angles (grad) in low-energy conformation states of T7 peptide

Residual	Form and shape of peptide chain				
	B <sub>2</sub> RB <sub>2</sub> B <sub>3</sub> RB <sub>3</sub> B <sub>3</sub> (efeeffe)	B <sub>2</sub> RB <sub>2</sub> B <sub>3</sub> RR <sub>3</sub> R <sub>3</sub> (efeeff)	B <sub>2</sub> RB <sub>2</sub> B <sub>3</sub> BB <sub>3</sub> R <sub>3</sub> (efeeeee)	B <sub>2</sub> RRB <sub>3</sub> RB <sub>3</sub> R <sub>3</sub> (effefe)	B <sub>2</sub> BRB <sub>3</sub> RB <sub>3</sub> R <sub>3</sub> (eefefe)
His1	*-113,105,180 177,197	-113,104,181 176,196	-113,105,180 177,197	-114,118,180 190,195	-115,115,181 179,199
Ala2	-93,-60,171 177	-94,-60,170 177	-93,-61,171 177	-78,-45,190 180	-108,126,173 160
Ile3	-161,143,178 183, 167,173,188	-162,144,178 183, 187, 173,188	-162,143,178 183,187,173,188	-69,-56,192 -57,188,175,187	-92,-53,180 -58,187,172,188
Tyr4	-131,158,167 -63,96,180	-131,160,166 -63,96,179	-130,157,158 -61,96,180	-115,159,179 -63,95,180	-116,163,179 -57,98,180
Pro5	-61,157	-65,159	-61,158	-61,159	-65,159
Arg6	-118,100,180 -60,177,182,180	-115,-60,180 -61,178,182,179	-117,100,181 60,178,182,179	-116,100,182 -64,175,181,180	-114,100,181 -62,176,181,180
His7	-117,140,186 -68,177	-113,-60,183 -62,178,	-116,-60,180 -61,179	-108,-60,182 -66,176	-107,-60,183 -66,177
Residual	Form and shape of peptide chain				
	B <sub>2</sub> BB <sub>3</sub> B <sub>3</sub> RB <sub>3</sub> R <sub>3</sub> (eeeffe)	R <sub>3</sub> RRB <sub>3</sub> RB <sub>3</sub> B <sub>3</sub> (fffeffe)	R <sub>2</sub> RB <sub>3</sub> B <sub>1</sub> RB <sub>3</sub> B <sub>3</sub> (ffeeffe)	R <sub>2</sub> RB <sub>3</sub> B <sub>3</sub> BR <sub>3</sub> R <sub>3</sub> (ffeeff)	R <sub>3</sub> RRB <sub>3</sub> RR <sub>3</sub> R <sub>3</sub> (fffeff)
His1	*-115,115,180 180,199	-97,-45,178 -61,171	-99,-59,179 179,200	-97,-56,182 179,208	-97,-45,178 -61,171
Ala2	-106,126,175 58	-78,-38,176 180	-84,-53,177 180	-84,-47,177 180	-78,-39,177 180
Ile3	-97,120,185 -61,185,170,188	-77,-52,187 -59,186,173,189	-98,105,179 -57,185,173,189	-93,130,178 -60,185,172,189	-77,-51,186 -59,185,173,189
Tyr4	-127,162,171 -57,98,180	-113,162,157 -57,95,179	-133,157,180 57,89,180	-112,161,184 -59,97,181	-113,159,184 -56,94,180
Pro5	-66, 154	-61,157	-61,152	-81,154	-64,158
Arg6	-117,99,178 -60,178,181,179	-114,100,180 -62,177,180,180	-121,99,176 -61,181,179,180	-131,-62,175 -61,180,180,180	-111,-60,180 -62,178,180,180
His7	-110,-60,180 -67,177	-116,140,186 -69,176	-116,140,186 -69,176	-110,-59,184 -63,177	-112,-60,183 -62,178
Residual	Form and shape of peptide chain				
	B <sub>2</sub> BRB <sub>3</sub> RR <sub>3</sub> R <sub>3</sub> (eeffeff)	R <sub>2</sub> RB <sub>3</sub> B <sub>3</sub> BR <sub>3</sub> R <sub>2</sub> (efeeff)	R <sub>2</sub> RB <sub>3</sub> B <sub>1</sub> RR <sub>3</sub> R <sub>3</sub> (ffeeff)	B <sub>2</sub> BB <sub>3</sub> B <sub>1</sub> BR <sub>2</sub> B <sub>2</sub> (eeeff)	
His1	-115,115,180 179,200	-97,-56,182 179,207	-99,-59,179 178,201	-115,115,180 180,199	
Ala2	-106,127,173 60	-84,-47,176 180	-84,-53,178 179	-105,125,176 58	
Ile3	-92,-53,180 -58,187,172,188	-93,131,179 -60,185,172,189	-98,106,179 -58,185,172,189	-99,130,180 -57,188,172,188	
Tyr4	-115,160,179 -56,97,180	-110,162,186 -59,96,181	-134,159,180 57,89,180	-119,162,184 -60,95,180	
Pro5	-66,159	-83,153	-63,153	75,154	
Arg6	-110,-60,180 -61,178,181,180	-129,-62,175 -61,180,180,180	-117,-60,175 -61,182,178,180	-117,-65,177 182,179,180,180	
His7	-108,-60,185 -63,178	-122,-61,179 183,182	-111,-60,183 63,177	-121,132,180 193,190	

\*The angles are given in constituency: the main chain is  $\phi$ ,  $\psi$ ,  $\omega$  (upper line), side chain is  $\chi_1$ ,  $\chi_2$ ,  $\chi_3$ ,  $\chi_4$  (low line).

Table 3.

Conformation reconstructions in spatial structure of T7 peptide in MD process

Conformation 1, $E_{\text{tot}}=-25,7$ kcal/mol		→	
Conformation 3, $E_{\text{tot}}=-23.1$ kcal/mol		→	
Conformation 4, $E_{\text{tot}}=-22.8$ kcal/mol		→	
Conformation 6, $E_{\text{tot}}=-21.6$ kcal/mol		→	
Conformation 7, $E_{\text{tot}}=-20.9$ kcal/mol		→	
Conformation 11, $E_{\text{tot}}=-19.6$ kcal/mol		→	

Table 4.

The values of partial charges of functional group atoms of amino-acid residuals in peptide structure before and after molecular dynamics

Atoms	Before MD	Conformation state after MD					
		№ 1	№ 3	№ 4	№ 6	№ 7	№ 11
HIS 1							
N	-0.356	0.394	0.340	0.353	0.448	0.262	-0.031
CA	-0.064	-0.251	-0.231	-0.220	-0.263	-0.207	-0.592
CB	-0.075	0.055	0.057	0.037	0.038	0.019	0.104
CG	0.100	-0.486	-0.455	-0.453	-0.487	-0.352	-0.127
ND	-0.230	0.396	-0.414	0.360	0.341	-0.280	0.332
CE1	0.182	-0.418	0.566	-0.617	-0.596	0.547	-0.388
NE2	-0.255	0.594	-0.553	0.568	0.590	-0.664	0.425
CD2	0.054	-0.562	0.427	-0.399	-0.397	0.403	-0.305
C	0.450	0.218	0.178	0.141	0.188	0.164	0.270
O	-0.384	-0.406	-0.427	-0.465	-0.476	-0.453	-0.617
ALA 2							
N	-0.356	-0.048	-0.055	-0.067	-0.041	-0.076	-0.034
CA	0.064	-0.088	-0.074	-0.071	-0.069	-0.071	-0.070
CB	-0.090	-0.131	-0.127	-0.114	-0.103	-0.118	-0.115
C	0.450	0.228	0.227	0.234	0.222	0.249	0.231
O	-0.384	-0.375	-0.377	-0.382	-0.410	-0.372	-0.388
ILE 3							
N	-0.356	-0.022	-0.036	-0.061	-0.050	-0.062	-0.134
CA	0.064	-0.089	-0.077	-0.080	-0.076	-0.081	-0.049
CB	-0.050	-0.087	-0.090	-0.071	-0.059	-0.071	-0.080
CG2	-0.075	-0.101	-0.099	-0.104	-0.133	-0.138	-0.110
CG1	-0.020	-0.112	-0.099	-0.111	-0.111	-0.105	-0.140
CD	-0.075	-0.122	-0.113	-0.143	-0.116	-0.111	-0.113
C	0.450	0.240	0.233	0.229	0.238	0.230	0.231
O	-0.384	-0.397	-0.389	-0.378	-0.396	-0.380	-0.355
TYR 4							
N	-0.356	-0.042	-0.044	-0.066	-0.057	-0.038	-0.060
CA	-0.064	-0.064	-0.068	-0.067	-0.073	-0.061	-0.076
CB	-0.040	-0.024	-0.023	-0.046	-0.040	-0.058	-0.065
CG	0.020	-0.148	-0.145	-0.125	-0.122	-0.135	-0.133
CD1	-0.010	-0.148	-0.044	-0.069	-0.081	-0.053	-0.062
CE1	-0.060	-0.196	-0.193	-0.155	-0.158	-0.201	-0.204
CQ	0.225	0.148	0.158	0.151	0.146	0.126	0.102
CE2	-0.060	-0.151	-0.152	-0.201	0.179	-0.152	-0.141
CD2	-0.010	-0.069	-0.074	-0.048	-0.053	-0.074	-0.062
OG	-0.330	-0.249	-0.231	-0.250	-0.249	-0.255	-0.225
C	0.450	0.223	0.221	0.246	0.253	0.220	0.268
O	-0.385	-0.397	-0.393	-0.409	-0.225	-0.390	-0.413
PRO 5							
N	-0.285	-0.037	-0.034	-0.016	-0.036	-0.014	-0.051
CD	0.100	-0.071	-0.072	-0.066	-0.042	-0.067	-0.060
CG	-0.050	-0.105	-0.104	-0.125	-0.069	0.231	-0.096
CB	-0.025	-0.124	-0.124	-0.102	-0.112	-0.125	-0.123
CA	0.050	-0.062	-0.060	-0.072	-0.122	-0.108	-0.067
C	0.455	0.226	0.232	0.234	0.241	0.256	0.238
O	-0.385	-0.354	-0.368	-0.376	-0.358	-0.409	-0.344

**CONFORMATION PROPERTIES OF HIS1-ALA2-ILE3-TYR4-PRO5-ARG6-HIS7 MOLECULE**

<b>ARG 6</b>							
N	-0.356	-0.039	-0.036	-0.043	-0.026	-0.032	-0.046
CA	0.064	-0.095	-0.098	-0.090	-0.097	-0.098	-0.066
CB	-0.030	-0.087	-0.089	-0.090	-0.088	-0.087	-0.112
CG	-0.030	-0.141	-0.143	-0.140	0.141	-0.144	-0.136
CD	0.120	-0.061	-0.058	-0.056	-0.055	-0.051	-0.101
NE	-0.300	0.009	0.004	0.001	-0.008	-0.006	0.077
CQ	0.580	-0.478	-0.452	-0.384	-0.398	-0.411	-0.495
NZ1	-0.390	0.127	0.133	0.137	0.132	0.143	0.138
NZ2	-0.390	0.112	0.118	0.156	0.143	0.129	0.153
C	0.450	0.219	0.228	0.225	0.231	0.228	0.231
O	-0.384	-0.421	-0.401	-0.424	-0.406	-0.404	-0.403

Atoms	Before MD	Conformation state after MD					
		№ 1	№ 3	№ 4	№ 6	№ 7	№ 11
HIS 7							
N	-0.356	0.031	0.028	-0.023	0.026	0.024	-0.060
CA	-0.064	-0.071	-0.064	-0.073	-0.060	-0.067	-0.065
CB	-0.075	-0.060	-0.054	-0.052	-0.052	-0.043	-0.052
CG	0.100	-0.206	-0.207	-0.166	-0.172	-0.208	-0.207
ND	-0.230	-0.525	-0.260	-0.305	-0.541	-0.473	-0.260
CE1	0.182	-0.569	0.514	0.508	-0.558	-0.585	0.202
NE2	-0.255	-0.520	-0.567	-0.570	-0.524	-0.517	-0.504
CD2	0.054	-0.254	0.521	0.562	-0.305	-0.269	-0.225
C	0.450	0.309	0.306	0.341	0.298	0.303	0.260
O	-0.384	-0.570	-0.570	-0.631	-0.578	-0.577	-0.570

Table 5.  
The distances (in Å) between oxygen atoms of peptide groups space-connivent  
of amino-acid residuals in different conformation states of T7 peptide.

Distances between oxygen atoms	Conformation					
	№1	№3	№4	№6	№7	№11
Hys1(O)-Ile3(O)	5.8	5.8	4.6	6.3	4.5	6.0
Hys1(O)-Tyr4(O)	9.3	9.4	6.5	9.9	6.6	8.2
Ala2(O)-Tyr4(O)	7.0	7.0	5.9	7.1	6.0	5.9
Tyr4(O)-Arg6(O)	6.1	6.1	6.4	5.7	5.7	5.5
Tyr4(O)-Hys7(O)	10.4	9.7	9.4	9.3	10.3	9.3
Pro5(O)-Hys7(O)	7.5	6.9	6.9	5.8	7.5	5.9

- 
- [1] L. Han, R. Huang, S. Liu, S. Huang, C. Jiang. Peptide-conjugated PAMAM for targeted doxorubicin delivery to transferrin-receptor over expressed tumors. *Mol. Pharm.*, 2010, vol. 7(6), p. 2156-2165.
- [2] L. Han, J. Li, S. Huang, R. Huang, S. Liu, X. Hu, P. Yi, D. Shan, X. Wang, H. Lei, C. Jiang. Peptide-conjugated polyamidoamine dendrimer as a nanoscale tumor-targeted T1 magnetic resonance imaging contrast agent. *Biomaterials*, 2011, vol. 32(11), p.2989-2998.
- [3] L. Han, R. Huang, J. Li, S. Liu, S. Huang, C. Jiang. Plasmid pORF-hTRAIL and doxorubicin co-delivery targeting to tumor using peptide-conjugated polyamidoamine dendrimer. *Biomaterials*, 2011, vol. 32(4), p.1242-1252.
- [4] S. Oh, B.J. Kim, N.P. Singh, H. Lai, T. Sasaki. Synthesis and anti-cancer activity of covalent conjugates of artemisinin and a transferrin-receptor targeting peptide. *Cancer Lett.*, 2009, vol. 274(1), p.33-39.
- [5] L.A. Brammer, B. Bolduc, J.L. Kass, K.M. Felice, C.J. Noren, M.F. Hall. A target-unrelated peptide in an

- M13 phage display library traced to an advantageous mutation in the gene II ribosome-binding site. *Anal Biochem.*, 2008, vol. 373(1), p.88-98.
- [6] *J.H. Lee, J.A. Engler, J.F. Collawn, B.A. Moore.* Receptor mediated uptake of peptides that bind the human transferrin-receptor. *Eur J Biochem.*, 2001, vol. 268(7), p.2004-2012.
- [7] *E.M. Popov.* Quantitative approach to conformations of proteins. *Int. J. Quant. Chem.*, 1979, v.16, p.707-737.
- [8] *E.M. Popov.* Strukturnaya organizatsiya belkov. M., Nauka, 1989, 352s. (in Russian)
- [9] *F.A. Momany, R.F. McGuire, A.W. Burgess, H.A. Scheraga.* Energy parameters in polypeptides: geometric parameters, partial atomic charges, nonbonded interaction for naturally occurring amino acid. *J. Phys. Chem.*, 1975, v.79, p.2361-2381.
- [10] *G.D. Abbasova, I.N. Aliyeva, A.I. Omarova, N.M. Gojayev.* Prostranstvennaya struktura i konformatsionnie svoystva analogov peptida CREKA. *Isvestiya NANA (seriya fiz.-mat. i tekhnicheskikh nauk)*, 2010, v. XXX, n.5, s.112-120. (in Russian)
- [11] *G.D. Abbasova, I.N. Aliyeva, A.I. Omarova.* Modelirovanie prostranstvennoy strukturi i konformatsionnie svoystva peptida T7. "Fizikanın müasir problemləri" V Respublika Elmi Konfransı, 16-17 dekabr, 2011, s.175-177. (In Russian).
- [12] *IUPAC-IUB Quantity, Units and Symbols in Physical Chemistry,* Blackwell Scientific Publications, Oxford, v. 39, 1988.
- [13] *E.E. Shnol, A.G. Grivtsov i dr.* Metod molekulyarnoy dinamiki v fizicheskoy khimii. M.:Nauka, 1996. (In Russian).
- [14] *K.V. Shaytan.* "Energeticheskaya poverkhnost i konformatsionnaya dinamika molekul. *Elektrokhimiya*, 2003, t.39(2), s.212-219. (in Russian).
- [15] *K.V. Shaytan. S.S. Saraykin.* Metod molekulyarnoy dinamiki. 1999. (In Russian).

*Received: 06.10.2015*



## DIELECTRIC RELAXATION IN THE BaTiO<sub>3</sub> PARTICLES –LIQUID CRYSTAL COLLOIDS

T.D. IBRAGIMOV<sup>a</sup>, A.R. IMAMALIYEV<sup>a</sup>, E.A. ALLAHVERDIYEV<sup>a</sup>,  
S.T. AZIZOV<sup>a</sup>, O.A. ALIEV<sup>a</sup>, G.M. BAYRAMOV<sup>a,b</sup>

<sup>a</sup>*Institute of Physics of Azerbaijan National Academy of Sciences,*

*G.Javid av.131, Baku, AZ1143, Azerbaijan*

*E-mail:tdibragimov@mail.ru*

<sup>b</sup>*Baku State University. 23 Z.Khalilov Street, AZ1148. Baku, Azerbaijan*

Influence of ferroelectric BaTiO<sub>3</sub> particles on dielectric properties of liquid crystals (LC) 5CB and H37 has been investigated. It has been shown that the presence of particles increases dielectric permittivity and losses and shifts a maximum of dielectric absorption to lower frequencies.

Experimental results are explained by interaction of LC molecules with the polarized ferroelectric particles at application of external electric field.

**Keywords:** BaTiO<sub>3</sub>, oleic acid, particles, liquid crystal, electro-optics, dielectric permittivity.

**PACS:** 64.70.mj; 64.70.pv; 78.15.e; 82.70.d.

### 1. INTRODUCTION

One of directions of modern technology and physics of liquid crystals (LC) is development of hybrid systems, in particular, consisting of small particles embedded in a LC matrix. There appears additional attention if the particle substance is ferromagnetic or ferroelectric. It was shown in one of the first works [1] that the presence of ferromagnetic particles in a LC matrix at low concentration leads to an increase of LC sensitivity to magnetic fields. Authors of the work [2] have obtained stable colloids based on iron oxide particles in the liquid crystal 5CB and showed that their electro-optic properties slightly differed from the pure LC but possessed properties of a magnetic liquid. In recent years such researches have started with a system of ferroelectric particles in LC. It has been shown that the presence of ferroelectric particles increases dielectric response of LC and changes its conductivity [3, 4], and also produces the photorefractive effect [5]. Besides, the memory effect in the isotropic phase of the liquid crystal 5CB by doping with barium titanate particles was discovered [6].

The aim of this work is to study the influence of embedded small ferroelectric BaTiO<sub>3</sub> particles on dielectric properties of the liquid crystal 5CB and the LC mixture H37 with positive and negative dielectric anisotropies, respectively.

### 2. EXPERIMENTAL

We used the liquid crystal 4-cyano-4'-pentylbiphenyl (5CB) and the liquid crystalline mixture consisting of 4-methoxybenzylidene-4'-butylaniline (MBBA) and 4-ethoxybenzylidene-4'-butylaniline (EBBA) with a molar ratio of 1:1 (H37) as matrices. A dielectric anisotropy of 5CB is positive and one of H37 is negative. The temperature range of the nematic phase of 5CB is located between 21.5°C and 35.2°C while the corresponding interval of H37 is from -10.1°C to 61.2°C.

The barium titanate particles with the sizes of 600 ± 10 nm (U.S. Research Nanomaterials, Inc.) was first

mixed with oleic acid and heptane in a weight ratio of 1:2:10 and was shaken on a vortex mixer for 1 hour, followed by sonication for 3 hours. Then, the obtained mixture was added into the liquid crystal and kept at temperature 60°C for 5 days till finished evaporation of heptane. The completed evaporation of heptane was controlled by weighing in the analytic balance (model PW, Adam Equipment, Co Ltd, UK) with an accuracy of 10<sup>-7</sup> kg. The final composition was also ultrasonically mixed for 3 hours. As a result, the colloid with weight percent 1% of particles was obtained.

The cell had a sandwich structure and consisted of two plane-parallel glass plates whose inner surfaces were coated with thin transparent and conductive indium-tin-oxide (ITO) layer. The cell thickness was fixed with calibrated 60µm polymer spacers for dielectric measurements. Both the colloid and the pure LC were injected into the empty cell by capillary action at the isotropic state. The filled cell was kept in the special heater in which the copper-constantan thermocouple was used for temperature measurements. Accuracy of temperature determination was 0.1°C.

Dielectric measurements were carried out by the Precision LCR Meter 1920 (IET Labs. Inc., USA) in the frequency range of 20 Hz -1 MHz. Dielectric parameters were recorded at temperature 24°C.

### RESULTS

Observation under the polarization microscope has shown that the presence of BaTiO<sub>3</sub> particles in 5CB and H37 decreases the clearing temperature from 35.2°C to 32.4°C and from 61.2°C to 60.1°C, respectively.

Dependences of real and imaginary parts of dielectric permittivity for the pure LCs and the colloids at homeotropic and planar orientations of LC molecules are presented in fig.1 and fig.2, accordingly. As one can see, the additive of BaTiO<sub>3</sub> particles increases both dielectric permittivity and losses in all studied frequency range. Particularly, dielectric permittivity of the BaTiO<sub>3</sub>-5CB colloid and the pure 5CB are equal to 19.3 and 18.2,

respectively, in the homeotropic cell. While, corresponding values equal to 7.8 and 6.6 for the planar cells. The additive of particles in H37 increases dielectric permittivity from 4.6 to 5.1 at the homeotropic orientation and from 5.2 to 6.1 in the planar cell. Dielectric permittivity of investigated samples decreases at high frequencies. At this case, it starts to decrease at higher frequencies for the planar cells and also in samples based on H37 than for the others. The dielectric absorption band is observed only in the homeotropic cells with the pure 5CB and the corresponding colloid in the studied frequency range. Meanwhile, a maximum of this band is shifted from 350 kHz to 300 kHz at the additive of particles.

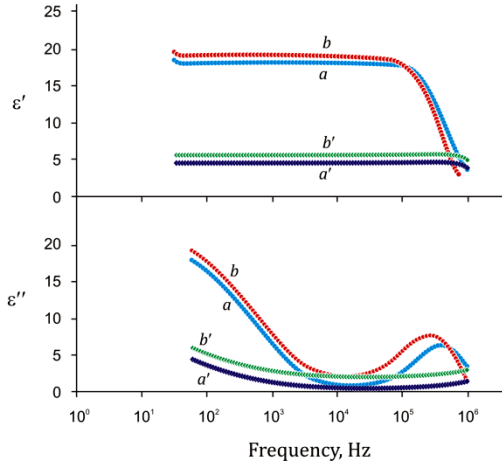


Fig.1. The frequency dependence of the parallel component of dielectric permittivity and losses: (a) pure 5CB; (b) BaTiO<sub>3</sub>-5CB; (a') pure H37 and (b') BaTiO<sub>3</sub>-H37.

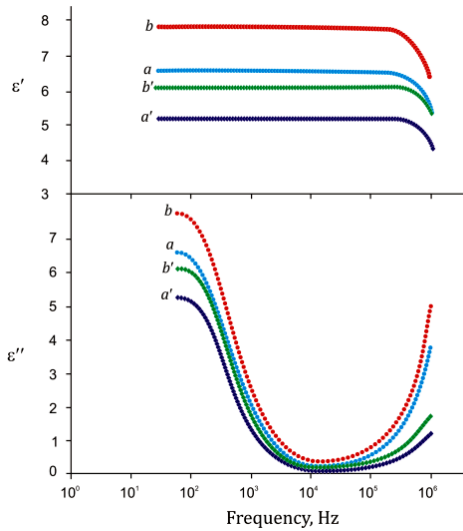


Fig.2. The frequency dependence of the perpendicular component of dielectric permittivity and losses: (a) pure 5CB; (b) BaTiO<sub>3</sub>-5CB; (a') pure H37 and (b') BaTiO<sub>3</sub>-H37.

The voltage dependences of dielectric permittivity at the frequency of 1 kHz are shown in fig.3. At this case, the initial orientation of the cells based on 5CB and H37 are planar and homeotropic, correspondingly. Apparently, dielectric permittivity starts to increase at certain voltage corresponding to the Freedericksz effect voltage.

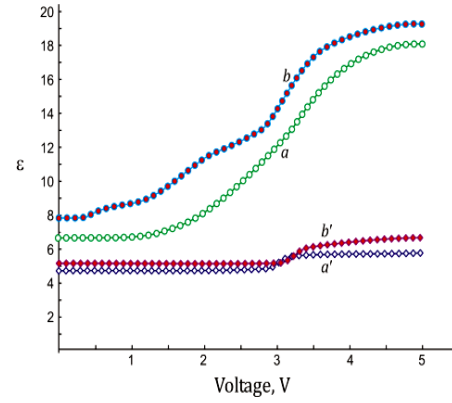


Fig.3. The voltage dependence of dielectric permittivity: (a) pure 5CB; (b) BaTiO<sub>3</sub>-5CB; (a') pure H37 and (b') BaTiO<sub>3</sub>-H37.

### 3. DISCUSSION

According to [7], particles do not disturb the director field of a LC, if the anchoring parameter  $\zeta = WR/K$  is much smaller than 1, where  $W$  is the anchoring energy of LC molecules with particle surfaces;  $2R$  is particle size;  $K$  is the LC elastic constant. The value of anchoring energy is within  $10^{-4}$ - $10^{-6}$  J/m<sup>2</sup>, the elastic constant of LC has an order of  $10^{-12}$  N, and the particles have sizes of 600 nm. Using oleic acid, we reduce anchoring energy and simultaneously stabilize the colloid. Besides, taking into account the given concentration of particles, particle sizes, and the particle density, one can calculate that the average distance between particles equals to 7.5 μm, which is much more than their size. Thus, the overall disturbance of the director field by particles appears negligibly. Hence, the obtained colloids can be considered as a homogeneous media and they should behave as pure LCs but with the modified parameters.

For the spherical form and low concentration of particles, the clearing temperature  $T_c$  of a colloid is defined by the expression [8]:

$$T_c = (1-f_v) T_{cp},$$

where  $f_v$  is the volume fraction of particles,  $T_{cp}$  is the clearing temperature of the pure LC. The volume fraction of barium titanate particles equals to 0.002 but the total fraction of the filler including the oleic acid amounts to 0.024. One can see, the calculations fairly well agree with the experimental values of clearing temperatures of the colloids.

According to Maxwell-Garnett theory for composites with spherical ferroelectric particles, the effective dielectric permittivity  $\epsilon_{ef}$  for the has the following form [5]:

$$\epsilon_{ef} \approx \epsilon^{LC} (1 + 3f_v),$$

where  $\epsilon^{LC}$  is dielectric permittivity of LC,  $f$  is volume fraction of the particles. Simple calculations show that the experimental values are much more than the theoretical ones. It is evident that such difference is connected by coupling of the LC molecules with spontaneous polarization of the particles giving additional contribution in dielectric permittivity.

There is a dispersion of the parallel component of dielectric permittivity at lower frequency because of the LC molecules have no enough time to turn about a short axis at fast changes of the direction of the applied field, while perpendicular component does not almost vary as it corresponds to the turn of LC molecules around their long axis. At this case, the dispersion of the samples based on H37 starts at higher frequencies because its molecules have weak polar groups which turn around the axes easier than ones of 5CB.

The shift of absorption band to lower frequencies for the BaTiO<sub>3</sub>-5CB colloid indicates an increase in the relaxation times for corresponding molecules reorientation:  $\tau \sim 1/2\pi f$ . The additive of particles in 5CB increases relaxation time from  $4.5 \cdot 10^{-7}$  sec to  $5.3 \cdot 10^{-7}$  sec. The increase in the relaxation time of the colloid suggests a strong interaction existing between the LC molecules and the BaTiO<sub>3</sub> particles. The LC molecules interact with spontaneous dipole moments of the ferroelectric particles. These factors obstruct the rotation of the LC molecules in the vicinity of the particles and result in a decrease of the absorption band frequency. The broadening of the absorption band is explained by dissipation of the energy at the reorientation of the LC molecules in the vicinity of the particles. The increase of dielectric losses is connected with an increase in the conductivity of the composite.

The threshold voltage of the Freedericksz effect for a pure LC, and also a low-concentrated colloid is defined by the expression [9]:

$$U_{th} = \pi (K_{ii}/\epsilon_0 \Delta\epsilon)^{1/2},$$

where  $i = 1$  and  $3$  for LC with positive and negative dielectric anisotropy, respectively;  $K_{11}$  and  $K_{33}$  are the

splay and bend elastic constants, respectively;  $\epsilon_0$  is the electric constant;  $\Delta\epsilon$  is the dielectric anisotropy.

The changed value of the Freedericksz effect voltage for the colloid in comparison with the pure LC is connected with two competitive factors: the presence of particles, increasing the order parameter [10] and oleic acid molecules decreasing this parameter which affects on the dielectric anisotropy of the colloid. As a result, the threshold voltage varies.

## CONCLUSIONS

The presence of BaTiO<sub>3</sub> particles in 5CB and H37 decreases the clearing temperature from 35.2°C to 32.4°C and from 61.2°C to 60.1°C, respectively.

The additive of particles in H37 increases dielectric permittivity and losses. The dielectric absorption band is observed only in the homeotropic cells with the pure 5CB and the corresponding colloid in the studied frequency range. Meanwhile, a maximum of this band is shifted to lower frequencies at the additive of particles.

The threshold voltage of the Freedericksz effect equals to 0.3 V for the BaTiO<sub>3</sub>-5CB colloid while the beginning of this effect for the pure 5CB is observed at 2.1 V. The threshold voltage of the Freedericksz effect increases from 2.8 V to up 3.1 V at additive of particles in H37. Experimental results are explained by interaction of LC molecules with the polarized ferroelectric particles at application of external electric field.

## ACKNOWLEDGMENTS

This work was done with the support of the Science and Technology Center in Ukraine (grant no. 5821).

- 
- [1] F. Brochard, P.G.de Gennes, Theory of magnetic suspensions in liquid crystals, J. de Physique **31** (1970) 691-706.
  - [2] O. Buy, E. Guskova, Yu. Reznikov, P. Litvin. Preparation and properties of a ferromagnetic nematic suspension, Ukr. J. Phys. **49** (2004) A48-A50.
  - [3] O. Buchnev, E. Ouskova, and Yu. Reznikov, V. Reshetnyak, H. Kresse. Enhanced dielectric response of liquid crystal ferroelectric suspension, Mol. Cryst. Liq. Cryst., **422** (2004) 47–55.
  - [4] E. Quskova, O. Buchnev, V. Reshetnyak, Yu. Reznikov, H. Kresse. Dielectric relaxation spectroscopy of nematic liquid crystal doped with Sn<sub>2</sub>P<sub>2</sub>S<sub>6</sub> nanoparticles, Liquid Crystals, **30** (2003) 1235–1239.
  - [5] O. Buchnev, A. Dyadyusha, M. Kaczmarek, V. Reshetnyak, Yu. Reznikov. Enhanced two-beam ferroelectric nanoparticles in liquid crystals, J. Opt. Soc. Am. B, **24** (2007) 1512-1516.
  - [6] R. Basu. Soft memory in a ferroelectric nanoparticle-doped liquid crystal, Phys. Rev. E **89** (2014) 022508-1- 022508-5.
  - [7] Yu. Reznikov. Ferroelectric colloids in liquid crystals, Liquid Crystals beyond Displays: Chemistry, Physics, and Applications. Li Q., eds., New Jersey, Hoboken: John Wiley and Sons, (2012) 403-427.
  - [8] F. Haragushi, K. Inoue, N. Toshima, S. Kobayashi, and K. Tukato. Reduction of the threshold voltages of nematic liquid crystal electrooptical devices by doping inorganic nanoparticles. Japanese Journal Applied Physics, **46** (2007) L796-L797.
  - [9] S.V. Pasechnik, V.G. Chigrinov, D.V. Shmeliova. Liquid Crystals: Viscous and Elastic Properties, (2009) Wiley-VCH Verlag GmbH and Co. KGaA, Weinheim, 438, p.181.
  - [10] J.-F. Blach, S. Saitzek, C. Legrand, L. Dupont, J.-F. Henninot, M. Warenghem. BaTiO<sub>3</sub> ferroelectric nanoparticles dispersed in 5CB nematic liquid crystal: Synthesis and electro-optical characterization, Journal Appl. Phys. **107** (2010) 074102-1 -7.

Received: 07.10.2015

# OPTICAL SPECTRA OF AMORPHOUS SELENIUM OBTAINED UNDER DIFFERENT CONDITIONS (PART I)

N.Z. JALILOV

*Institute of Physics of Azerbaijan NAS,  
G. Javid av., 131, Baku AZ-1143, Azerbaijan*

Reflection coefficients  $R(E)$  of amorphous (massive) film and polycrystalline selenium in beam energy interval 1-6eV normally falling on surface are investigated and the spectral dependences of their optical constants and dielectric functions are calculated by Kramers-Kronig methods. It is shown that the character of selenium change character of their optical parameters changes in dependence on selenium sample obtaining conditions.

**Keywords:** dispersion, optical parameters, binary compounds.

**PACS:** 535.3; 539.2/6; 539./04

## INTRODUCTION

Reflection coefficients  $R(E)$  of material series (amorphous and single crystal  $\text{InSnTe}_2$ ,  $\text{TlIn}_{0.9}\text{Ce}_{0.1}\text{Se}_2$ ,  $\text{TlInSe}_2\text{Ce}_{0.04}$ ,  $\text{TlInSe}_2$ ,  $\text{Cu}_3\text{GdTe}_3$ ,  $\text{Cu}_5\text{GdTe}_4$ ,  $\text{CuGdTe}_2$ ,  $\text{Se}_{95}\text{As}_5$  (with impurity Sm),  $\text{Bi}_2\text{Te}_3(\text{Ni}, \text{Cu}, \text{Zn})$ ,  $\text{Bi}_2\text{Te}_3$ ,  $\text{Bi}_2\text{Se}_3$  are measured. Reflected light phase  $\theta$ , index of absorption  $\kappa$  and index of refraction  $n$ , real  $\varepsilon_1$  and imaginary  $\varepsilon_2$  parts of dielectric constant,  $\alpha$  absorption coefficient, function of characteristic  $-\text{Im}g \varepsilon^{-1}$  volume and  $-\text{Im}g(\varepsilon+1)^{-1}$  surface electron losses,  $(\alpha, \beta)$  electrooptical differential functions,  $\varepsilon_2 E$  optical conduction,  $\varepsilon_2 E^2$  integral function of bound state density,  $\varepsilon_0(E)$  effective static electric constant,  $n_{ef}(E)$  effective number of valent electrons taking part in transitions up to the given energy, are calculated.

The results on optical spectra of amorphous selenium obtained at different conditions are given in the given paper.

The selenium as elementary semiconductor in polycrystalline states and amorphous ones are widely applied in electro-optical transformers [1]. The many fundamental works are dedicated to this investigation. However, the supposed separate models used for explanation of electron processes taking place in it nowadays are needed in new data. This is connected with the fact that it has the different structural peculiarities. Being the inorganic polymer, selenium has the amorphous,  $\alpha$  and  $\beta$  monoclinic, hexagonal modifications with ring-shaped, chain molecules, which have the different number of atoms. All its modifications in wide temperature interval can exist in the sample simultaneously in different quantities. Indeed, selenium many properties are defined by ratio of these modification in the sample in dependence on condition of their preparation.

The formation conditions and peculiarities of this or that selenium layer structure prepared by molecular steam condensation in vacuum are revealed and established in [2]. It is shown that selenium layer structure prepared by evaporation in vacuum is defined by temperature of condensed molecular steam, near-surface layer structure and substrate temperature. Moreover, the layer structure can present itself the super cooled state, first, second amorphous forms or intermediate amorphous state. In the given work it is confirmed that the structure of first amorphous form consists on ring-shaped molecules of  $\text{Se}_8$  type polymerized in accumulations the sizes of which are the order of several hundred meters. The structure of

second amorphous form consists on continuous polymerized chain molecules of selenium lattice hexagonal modification structural unit type. Such amorphous state presents itself the long-chain polymer of homogeneous density with initial softening temperature near 299K. Such structure in comparison with structure of first amorphous selenium form is more stable one. The intermediate amorphous state, which is constructed from structural elements of first and second amorphous forms and is enriched by atomic selenium is formed in process of transition from first amorphous form to the second one.

The samples prepared at different conditions that gives the opportunity of selenium obtaining with different structures in order to investigate its optical properties with the help of  $R(E)$  reflection coefficient measurements and calculations of optical parameters on Kramers-Kronig ratio are investigated in the given work. These parameters are directly connected with its electron structure. The material electron structure depends on its crystal structure, chemical composition and atom properties. As it is known the crystal selenium has the chain structure, the bond between the atoms in chain has the covalent character, and between chain atoms has the Van-der-Waals one. It has the complex electron structure. Its electron structure depends also on sample structural changes.

In amorphous or glass-forming systems the study of their properties with structure change is of specific interest because the possibility to study of correlation between structure and material properties (molar volume, viscosity, vitrification temperature, thermal expansion coefficient and others) appears.

The material energy level defining the many physicochemical properties is one of its main parameters. The knowing of the material dispersion allows us to forecast the principal possibilities of its definite property carrying out and application in semiconductor electronics.

The measurement of selenium reflection coefficient  $R(E)$  with different structure and definition of optical parameters is the aim of the given work.

## INVESTIGATION TECHNIQUE

For obtaining of amorphous sample  $\text{B}_5$  selenium, which is melted and kept at temperature 280°C during 3 hours, is taken and further, the ampoule with selenium is strongly put in cool water. The samples for measurements are prepared from this amorphous selenium mass. The

amorphous films of thickness  $2\div 8\mu\text{m}$  are obtained by thermal evaporation in vacuum and by hot wall epitaxy method from cover glass. The selenium polycrystalline samples are obtained by slowly cooling of melted selenium.

$R(E)$  reflection coefficients of amorphous massive, film and polycrystalline selenium are measured by method of double-beam spectroscopy at room temperature in radiation energy interval  $1\text{--}6\text{eV}$  normally falling on surface.

As it is indicated in [3] the semiconductor optical functions in wide region of fundamental absorption is more effectively studied by method of almost normal mirror reflection. The other pure optical methods have the essentially principal or methodic limits and give the information in limited spectral regions. They only add the results of normal reflection at definition of optic transition values. The optical functions are defined with help of reflection measurements by method of normal mirror reflection. The influence on reflected light phase and  $R(E)$  unmeasured spectrum region are necessary to take under the consideration for the definition of  $\theta(E)$  reflected light phase from measurements of reflection coefficient. That's why we use the extrapolation method  $R(E)$  on whole unmeasured region.

According to Maxwell equation, all optical parameters are interconnected ones that is seen from the following relation:

$$\frac{\omega^2}{v^2} = \frac{\mu}{c^2} 4\pi\sigma(i\omega) + \frac{\mu\varepsilon}{c^2} \omega^2,$$

where  $\omega$  is cyclic frequency,  $c$  is velocity of light in vacuum.

The interaction of light with the substance is described by  $n$  index of refraction and  $k$  index of absorption which characterize the phase and damping of plane wave in substance.

These values can be obtained from measurements of  $R(E)$  reflection coefficient and calculation of phase of reflected light using Kramers-Kronig formulae:

$$\theta(E_0) = \frac{E_0}{\pi} \int_0^\infty \frac{\ln R(E)}{E_0^2 - E^2} d\omega.$$

$n$  and  $k$  indexes are defined after calculation  $\theta$ , by formulas:

$$n = \frac{1 - R}{1 + R - 2\sqrt{R\cos\theta}}, \quad k = \frac{-2\sqrt{R\sin\theta}}{1 + R - 2\sqrt{R\sin\theta}}$$

The residual optical parameters are calculated by  $n$  and  $k$  values by corresponding formulas. For calculations of optical parameters the computer program which is applied in works [4-13] is written by us on the base of experimental data by  $R(E)$ .

## RESULTS AND DISCUSSIONS

$R(E)$  is measured in the work and the optical functions are defined on its base. Such parameters as  $\theta$  reflected light

phase, indexes of  $\kappa$  absorption and  $n$  refraction,  $\varepsilon_1$  real and  $\varepsilon_2$  imaginary parts of dielectric constant,  $\alpha$  absorption coefficient, the function of characteristic  $-\text{Im}g \varepsilon^{-1}$  volume and  $-\text{Im}g(\varepsilon+1)^{-1}$  surface electron losses,  $(\alpha, \beta)$  electrooptic differential functions,  $\varepsilon_2 E$  optical conduction,  $\varepsilon_2 E^2$  integral function of bound density of states,  $\varepsilon_0(E)$  effective static dielectric constant,  $n_{\text{ef}}(E)$  effective number of valent electrons taking part in transitions up to the given  $E$  energy are defined.

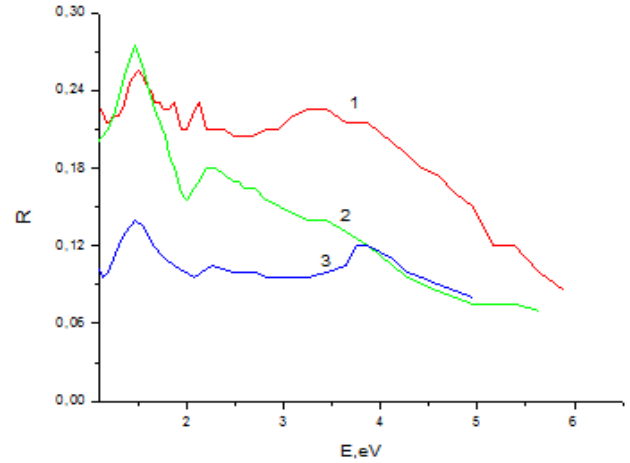


Fig.1. The reflection spectra  $R(E)$ : amorphous massive (curve 1), film (curve 2) and polycrystalline selenium (curve 3).

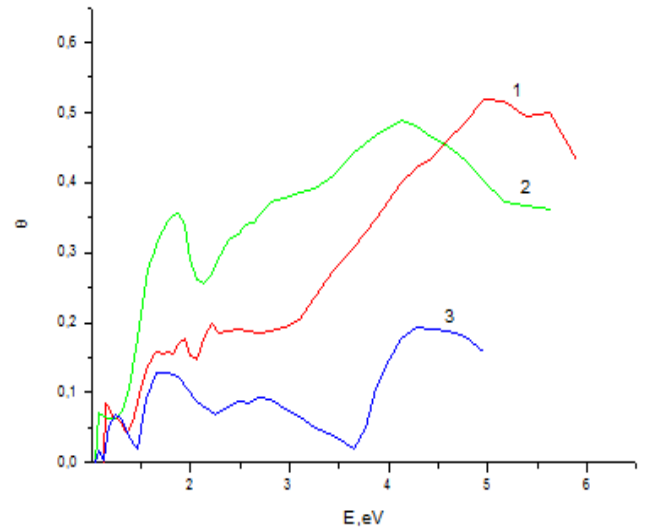


Fig.2. The reflection phase spectra  $\theta(E)$ : amorphous massive (curve 1), film (curve 2) and polycrystalline selenium (curve 3).

$R$  reflection coefficient,  $\theta$  reflected light phase, indexes of  $\kappa$  absorption and  $n$  refraction,  $\varepsilon_1$  real and  $\varepsilon_2$  imaginary parts of dielectric constant,  $\alpha$  absorption coefficient, the function of characteristic  $-\text{Im}g \varepsilon^{-1}$  volume and  $-\text{Im}g(\varepsilon+1)^{-1}$  surface electron losses are presented on fig.1-9 from the obtained results and the values of optical interband transitions defined on  $\varepsilon_2(E)$  base in photon energy region  $1\div 6\text{ eV}$  are given in the table.

As it is mentioned in [14] the study of absorbing transition on materials is impossible because of big value of absorption in region of  $E > E_g$  interband transition region ( $E_g$  is minimal energy of interband transitions called by forbidden band energy).

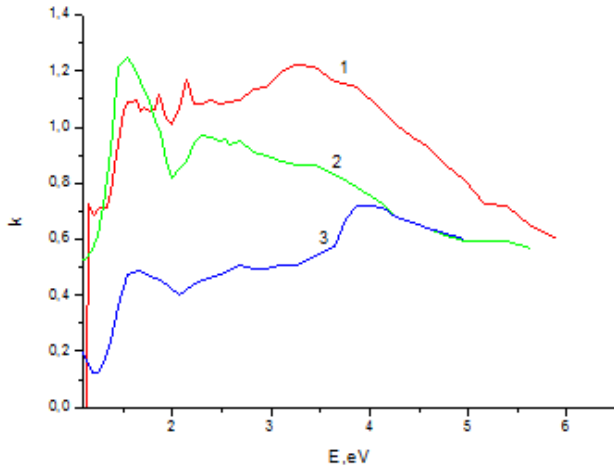


Fig.3. The absorption index spectra  $k(E)$ : amorphous massive (curve 1), film (curve 2) and polycrystalline selenium (curve 3).

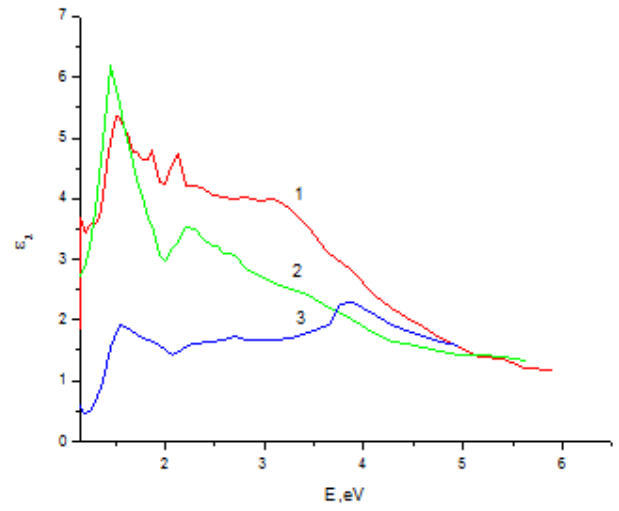


Fig.6. The spectra of imaginary part of dielectric constant  $\epsilon_2(E)$ : amorphous massive (curve 1), film (curve 2) and polycrystalline selenium (curve 3).

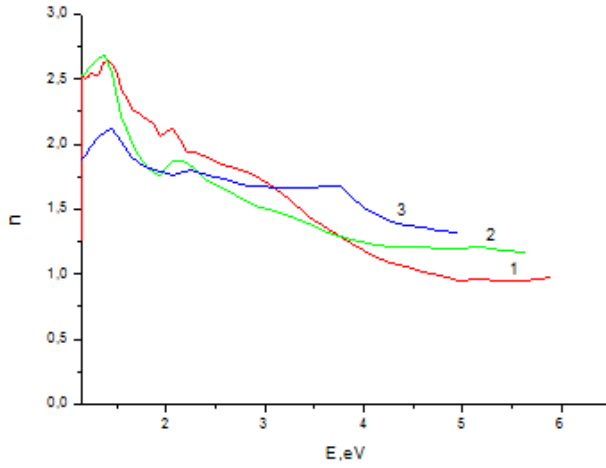


Fig.4. The refraction index spectra  $n(E)$ : amorphous massive (curve 1), film (curve 2) and polycrystalline selenium (curve 3).

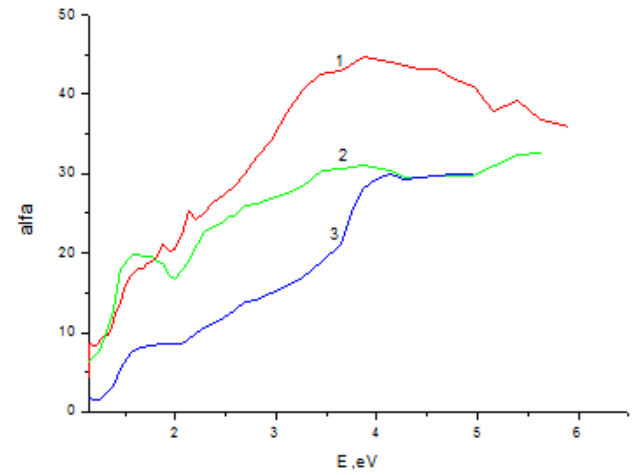


Fig.7. The absorption spectra  $\alpha(E)$ : amorphous massive (curve 1), film (curve 2) and polycrystalline selenium (curve 3).

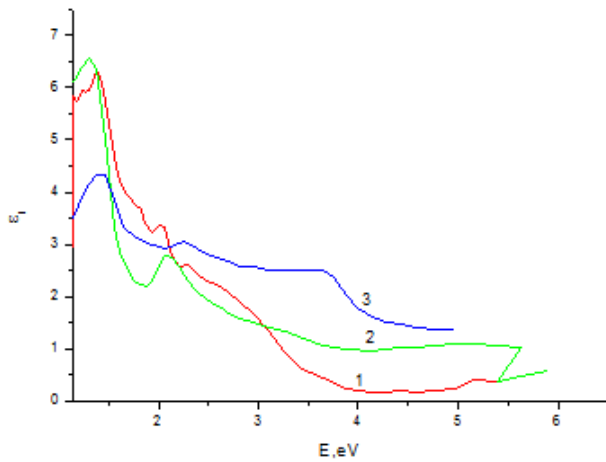


Fig.5. The spectra of real part of dielectric constant  $\epsilon_1(E)$ : amorphous massive (curve 1), film (curve 2) and polycrystalline selenium (curve 3).

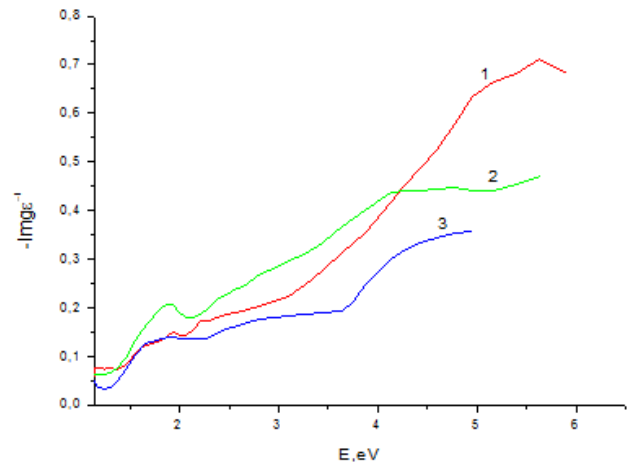


Fig.8. The electron volume loss spectra  $-\text{Im}g \epsilon^{-1}(E)$ : amorphous massive (curve 1), film (curve 2) and polycrystalline selenium (curve 3).



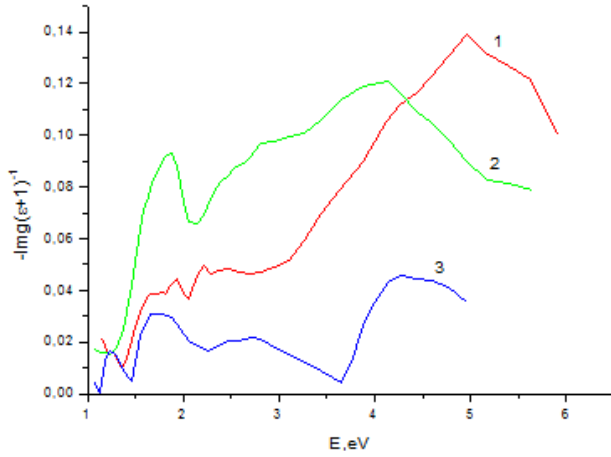


Fig.9. The electron surface volume loss spectra  $-Img(\epsilon+1)^{-1}(E)$ : amorphous massive (curve 1), film (curve 2) and polycrystalline selenium (curve 3).

The reflection is unique effective method. The analytical singularities of imaginary part of  $\epsilon_2(E)$  complex dielectric constant and functions bound by  $dN/dE$  state densities are almost coincide. The interband state gradient makes the main contribution into analytical singularity of  $dN/dE$  function:

$$\frac{dN_{ij}}{dE} \sim \int \frac{dS_k}{|\nabla_k E_{ij}|},$$

where  $E_{ij}(k) = E_j(k) - E_i(k)$  is the distance between conduction and valent bands.  $dN/dE$  values near critical points in  $k$ -space defined by  $|\nabla_k E_{ij}| = 0$  expression and also the positions of critical points and transition type can be theoretically calculated from band structure.

The analysis of  $\epsilon_2(E)$  function,  $dN/dE$  and  $R(E)$  reflection coefficient show that the disposition in energy spectrum and peak character are similar ones or very close ones for these parameters. That's why the values of corresponding interband gaps and band nature can be defined with the help of direct coincidence of experimental data on curves, crystal reflection in region with theoretical calculations of  $dN/dE$  function.

It is known that the least energy  $E_g$  between occupied and free states is the one of the important semiconductor parameters. The high transparency in  $E < E_g$  energy wide region is character for non-crystal materials. The several methods of its definition and evaluation by the level of  $\alpha(E)$  absorption coefficient of long-wave edge are known. The exact value of  $E_g$  for non-crystalline semiconductors is debatable one and usually the discussion of spectrum character in Urbach and Tauc models of is carried out

without  $E_g$  evaluations [15].  $E_g$  is defined from Tauc model by the value of absorption coefficient  $\alpha(E) = 10^3 \text{cm}^{-1}$ .

As it is mentioned in [15]  $N(E)$  state density is the similar useful settlement for crystalline and non-crystalline substances. According to existing results of experimental data the motion of state density in non-crystalline substance not strongly differ from corresponding motion of state density in crystal. In first case the thin structure can be smoothed and the local states can appear in forbidden state, the band structure is saved generally, i.e. it is defined by atom short-range order in materials.

The hexagonal crystalline selenium consists of helical chains put parallel to each other. The chemical bond inside the chains has the covalent character and is very strong one and the bond between the chains is the weak one by Van-der-Waals type. One can consider that in liquid phase the chains are oriented occasionally. The viscosity becomes the very high one before the chains become reoriented ones and glass-like state appears at rapid melt cooling.

The decomposition of ideal structure of non-crystalline solid state takes place in systems including the albums with non-divided electron couples. The electron couple is on one of the fragments at bond breaking, i.e. the heterolytic bond breaking takes place. Moreover one positive charged defect center and one negative one in short-order regions appear. The energy necessary for the bond breaking is partly compensated because of existing of non-divided electron couple of atoms being in nearest surrounding and the number of chemical bonds as a whole doesn't change. Thus, the structural disorder exists in homogenous glasses of stoichiometric composition along with density oscillations and existing topological disorder of different types. The last one is revealed in the form of positive and negative charged defect centers as in the case of point defects in crystals. As the reaction defects the formation of which is characterized by the least change of free energy dominate.

As it is mentioned in [16] there is no the principal boundary between monocrystalline, polycrystalline and amorphous states of substances. The presence of band structure that are forbidden and conduction bands can be taken from the fact of existing of atom short-range order and their no necessity to require the atom periodic position. These questions for amorphous and crystalline selenium are studied in [17-24], defined and their electron structures are compared.

Thus, one can conclude that the selenium electron structure will change in dependence on change character of atom short-range order with change of selenium structure. This is revealed on the change character of optical parameters of investigated samples that is seen from fig. 1-9 and from the table. The obtained data allows us to follow the selenium electron structure change with change of atom short-range order in it.

Table.

Sample	Optical transitions defined by $\epsilon_2(E)$ maximums in energy interval 1-6eV									
Amorphous massive	1,24	1,3	1,55	1,88	1,99	2,21	2,29	2,26	3,64	4,77
Film	1,13	1,46	1,55	2,21	2,29	2,38	2,53	2,69	3,44	5,19
Polycrystalline	1,24	1,55	1,65	1,88	2,48	2,69	4	4,13	-	-



- [1] *G.B. Abdullayev, D.Sh. Abdinov.* Fizika selen. Izd. Elm, 1975, Baku, 403. (in Russian).
- [2] *I.D. Nabitovich.* Dis. dokt. fiz.-mat. nauk. Lvov. 1970, 328. (in Russian).
- [3] *V.V. Sobolev, V.V. Nemoshkalenko.* Elektronnaya struktura poluprovodnikov. Kiev, nauk. Dumka, 1988. (in Russian).
- [4] *N.Z. Jalilov, S.I. Mekhtiyeva, N.M. Abdullayev.* Azerbaijan National Academy of sciences, Series of physical-mathematical and technical sciences physics and astronomy, 2007, XXVII, n.5, 114.
- [5] *N.Z. Jalilov, S.I. Mekhtiyeva, N.M. Abdullayev.* Fizika, 2007, XIII, n.4, 89.
- [6] *N.Z. Jalilov, G.M. Damirov.* Azerbaijan National Academy of sciences, Series of physical-mathematical and technical sciences physics and astronomy, 2009, XXVII, №5, 125.
- [7] *N.Z. Jalilov, S.I. Mekhtiyeva, N.M. Abdullayev, M.I. Veliyev.* II Ukrainskaya nauch. kon. po poluprovod., 2004, 140. (in Russian).
- [8] *N.Z. Jalilov, S.I. Mekhtiyeva, N.M. Abdullayev, M.I. Veliyev.* Azerbaijan National Academy of sciences, Series of physical-mathematical and technical sciences physics and astronomy, 2004, XXIV №5(I).
- [9] *S.I. Mekhtiyeva, N.Z. Jalilov, N.M. Abdullayev, N.R. Mamedov.* Dokladi NAN Azerb., 2007, LXIII, n.4, 48. (in Russian).
- [10] *N.Z. Jalilov, N.M. Abdullayev, N.R. Mamedov.* Amorfnie i Mikrokristallicheskie Poluprovodniki, Sb.trudov VI Mejd. Konf., Sankt-Peterburq, 2008, 238. (in Russian).
- [11] *N.Z. Jalilov, N.M. Abdullayev, N.R. Mamedov, G.M. Askerov.* Fizika, 2008, XIV, n.3, 144.
- [12] *N.Z. Jalilov, G.M. Damirov.* Trudi X Mejd. Konf. «Opto–nanoelektronika, nanotexnologii i mikro–sistemi», Ulyanovsk, 2008, 45. (in Russian).
- [13] *N.Z. Jalilov, G.M. Damirov.* Azerbaijan National Academy of sciences, Series of physical-mathematical and technical sciences physics and astronomy, 2008, XXVIII, №5, 134.
- [14] *J.C.Phillips.* Phys. Rev. 125 (1962) 1931; 133 (1964) A452.
- [15] *N. Mott, E. Devis.* Elektronnie proçhessi v nekristallicheskix veshestvax. Moskva «Mir» (1982). (in Russian).
- [16] *A. Rouz.* Osnovi teorii fotoprovodimosti. Izd., Mir, Moskva, (1966). (in Russian).
- [17] *N.J. Shevchik, M. Cardona and J. Tejeda.* Physical Review B, **8** №6 (1973) 2833-2841.
- [18] *J.D. Joannopoulos, M. Schlüter and L. Cohen Marvin.* Physical Review B, **11** №6 (1975) 2186-2199.
- [19] *A.Vaidyanathan, S.S. Mitra and Y.F. Tsay.* Physical Review B, **21** №6 (1980) 2475-2481.
- [20] *R.H. Williams and J.I. Polanco.* J. Phys C: Solid State Phys., **7** (1974) 2745-2759.
- [21] *L.D. Laude and Fitton, B. Kramer and K. Maschke.* Physical Review Letters, **27** №16 (1971) 1053-1056.
- [22] *B. Kramer.* Phys. Stat. sol., **41** (1960) 725-733.
- [23] *J.L. Hartke and Paul J. Regensburger.* Physical Review, **139** №3A (1965) A970-A980.
- [24] *G. Weiser and J. Stuke.* Phys. Stat. sol., **35** (1969) 747-753.

Received: 08.09.2015

## ELECTRONIC TREATMENT OF THE WATER MEDIUMS BY HIGH-VOLTAGE NANOSECOND PULSES

E.J. GURBANOV

*“Azersu” Open Joint Stock Company, Baku, Moscow av.67, Azerbaijan,  
KurbanovEJ\_mpei@mail.ru*

The present article to electronic treatment of the water medium (fluid foodstuff) in technological process by high-voltage pulses of nanosecond range is devoted. It is shown, that depending on electrophysical parameters of the treated medium and pathogenic microorganisms containing there the pulsed generator by electric parameters providing the effective application of its energy on loading for reaching full and irreversible inactivation of microorganisms is developed. Dependence ratios of the main power source parameters and electrophysical characteristics of the treated medium with microorganisms are given. It is revealed, that for full inactivation of water medium and stay of further reproduction of microorganisms there expediently impact by high-voltage pulses of nanosecond range. These calculation methods can form a basis at elaboration of high-voltage installations of technological appointment for disinfecting of water containing mediums (fluid foodstuff) from pathogenic microorganisms.

**Keywords:** water medium, treatment, microorganism, nanosecond pulse, front of pulse, high-voltage installation, inactivation, membrane, cell, electrophysical properties, electric field

**PACS:** 52.80.Wq

### INTRODUCTION

Pulsed treatment methods of various mediums and materials for improvement their properties and quality get more and more wide distribution owing to efficiency of strong electromagnetic fields impact on explored object with formation the big concentrations of chemically active discharge products [1-3]. In comparison with existing classical mechanical, chemical, temperature and electronic treatment methods of materials on AC and DC [4, 5] the pulsed treatment methods are very effective as with maximum application of source energy on loading, high-speed physical and chemical processes with formation of chemically active discharge components, high-frequency radiation, perniciously influencing on medium toxicity and on the commensurability of influence parameters with duration of physical processes in treated medium [6-8]. In this context researches, directed on electronic and ion treatment of the water containing mediums for inactivation of microorganisms, cause a great interest [9-12]. Depending on medium characteristics, its appointment and parameters of biological organisms, the main electric parameters of high-voltage installation and its components are defined.

The present article to electronic treatment of water containing mediums (fluid foodstuff) with various electrophysical properties by strong pulsed electric fields of nanosecond duration for inactivation of microorganisms containing there and extension of their storage terms is devoted.

### EXPERIMENTS AND CALCULATION METHODS

At elaboration of the high-voltage pulsed installations for electronic treatment of the water containing mediums it is necessary to decide with design of electrode system and the treatment mode. Depending on treated medium, its electrophysical properties, geometrical sizes of biological cells containing there an influencing high-voltage pulse parameters (amplitude, pulse front and duration) for ensuring efficiency of strong pulse electric fields impact on

treated medium for its full inactivation and prevention of their secondary appearance are defined. Account and coordination of all mutually influencing parameters of the high voltage installation is necessary for more effective application of the source energy (with minimum losses) on loading and more effective treatment of explored medium. A basic element of any high-voltage installation is the power source – the generator of pulsed tensions. In our researches it is executed on the basis of spark air rated sportsmen. In researches the high-voltage transformer on AC in combination with the high-voltage rectifier, as a high-voltage source, is used.

In researches as explored objects fluid foodstuff (juice, wine and milk products) were chosen.

For their disinfecting and extension of storage terms on condition of preservation of their initial nutrition and biological properties the electronic and ion treatment method in "plane – plane" electrode system for prevention of spark discharge in interelectrode distance by strong-pulsed electromagnetic fields of nanosecond range is considered. Pulse generator has the following parameters: amplitude at exit of generator - 80-100 kV, pulse duration - tens ns, frequency of following pulses – hundreds Hz.

It should be noted, that at choice of pulse duration, it is necessary to consider also the geometrical sizes of microorganisms containing in products. With reduction of the sizes of biological cells, it is expedient to apply short front pulses (nanosecond range) for full inactivation of microorganisms. This choice is based that high-frequency waves get directly into nucleus of cell and stop their further growth.

For carrying out researches of impact of high voltage pulsed electric fields on biological cells in fluid foodstuff, the nanosecond pulsed generator on capacitor energy stores was elaborated. The high-voltage installation was consisted from: high voltage transformer on 140 kV, generator of pulsed tensions with maximal amplitude - 100 kV and pulse parameters: front ~ 18 ns, duration on a half-height ~ 350 ns, frequency of following pulses ~ 1000 Hz and average power ~ 50 kW, working chamber with treated medium inside (an impedance

~10-1000 Ohms) and measuring equipment. For preservation of initial nutrition and biological properties of foodstuff and prevention of medium's spark breakdown the "plane-plane" electrode system was chosen.

Pulsed electric impact on biological cell, its reaction to this and mathematical description of the process is very difficult. Still there is no accurate description of this process [13]. The one-celled microorganisms, considered in article, have two-layer dielectric structure. Accounting of all main parameters of electric field, treated medium and obtained experimental data is necessary for modeling and description of processes of strong electric fields impact. The model of a two-layer biological cell is given in fig. 1.

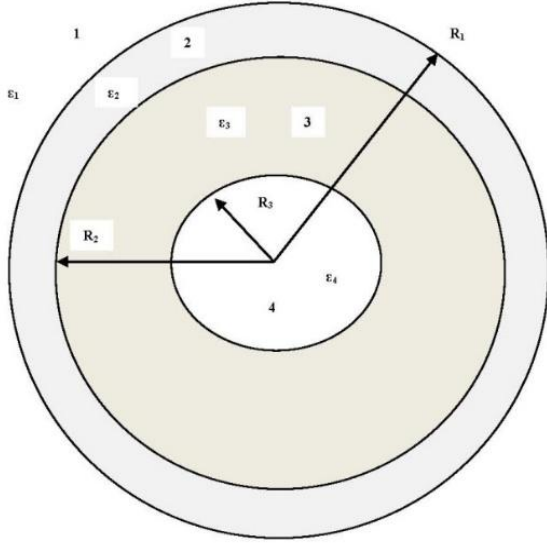


Fig. 1. Structure of a two-layer biological cell: 1 – the external medium of cell (the treated water medium); 2 – cell's membrane; 3 – cell's cytoplasm; 4 – cell's nucleus.

According to fig. 1, cell consists of the following elements: central nucleus - 4, external dielectric membrane - 2, inside and outside of which are the polarizable medium: cultural water medium - 1 and cell's cytoplasm - 3 [13]. Each of the specified areas has dielectric permeability, which value is considered at influence of high-frequency pulse electric fields. Owing to consideration of high-frequency pulsed fields we will neglect by cell's conduct properties.

It is known, that electric breakdown of membrane is one of death causes of cell [14]. Therefore, intensity of electric field and power failure on membrane are important characteristics of impact of strong electric field on cell. The vector of resultant electric field's intensity and its components can be defined by the known ratio [13].

$$\varphi^{(k)}(r, \theta) = \left( A_k r + \frac{B_k}{r^s} \right) \cos \theta, k = \overline{1, n}, \quad (1)$$

where  $\varphi$  is scalar potential of electromagnetic field;  $n$  is the number of mediums with various characteristics;  $k$  is the medium's index with characteristics;  $A_k, B_k$  is constants;  $r, \theta$  is radial and angular coordinates;  $s$  is the indicator, depending on a cover form of cell.

For spherical coordinates -  $s=2$ , for cylindrical -  $s=1$ . Power failure on membrane -  $U_m$  is determined by

integration of field intensity -  $E$  along radial coordinate -  $r$  by membrane thickness. For description of biological cell we will accept the following characteristics [13]: relative dielectric permeability of membrane from 2 up to 10; relative dielectric permeability of cytoplasm from 60 up to 81; internal radius of membrane -  $R_2=0,99 R_1$ .

We will find now, as an example, distribution of power lines of electric displacement vector -  $D$  and field's intensity -  $E$  in cell according to fig. 1.

In case of spherical cover form we can get formula for electric displacement stream:

$$\Phi_D^{(k)}(r, \theta) = -\varepsilon_k \pi r^2 \left( A_k - \frac{2B_k}{r^3} \right) \sin^2 \theta \quad (2)$$

Considering, that current -  $I$  and stream -  $\Phi_D$ , dielectric permeability -  $\varepsilon_k$  and specific conductivity -  $\gamma_k$  are similar, expression (2) with substitution of these values can be written down (in case of spherical cover) as follows:

$$I^{(k)}(r, \theta) = -\gamma_k \pi r^2 \left( A_k - \frac{2B_k}{r^3} \right) \sin^2 \theta \quad (3)$$

Induction stream  $\Phi_D$  of electric field satisfies to a ratio:

$$\Phi_D = \int_S D dS \quad (4)$$

where  $S$  is surface by which the induction stream is defined,  $dS$  is surface element.

For getting of the field power lines of vector  $\vec{E}$ , which are suffered on interphase borders between different mediums with various electrophysical characteristics [15-17], we use a stream of vector  $\vec{E}$ :

$$\Phi_E = \int_S \vec{E} dS \quad (5)$$

The last formula is connected with stream  $\Phi_D$  and  $I$  by following obvious ratios: for an electrostatic field  $\Phi_E^{(k)} = \frac{\Phi_D^{(k)}}{\varepsilon_k}$ , for electric field of current  $\Phi_E^{(k)} = \frac{I^{(k)}}{\gamma_k}$ .

## DISCUSSION OF RESULTS

So, depending on purpose of the treated medium, its electrophysical properties and geometrical sizes of microorganisms containing there, the range of influencing pulse tension is chosen.

At electronic treatment of fluid foodstuff for inactivation of pathogenic microorganisms containing there and extension of their storage terms an important criterion is observance of initial nutrition and biological properties of these products. For reaching this it was developed an electrode system "plane - plane" with uniform electric field in working chamber and the generator of nanosecond pulses.

Experiments showed, that for full inactivation of microorganisms it is more expedient to influence on treated medium by pulses of nanosecond range - with front ~ 20 ns and duration ~ hundreds ns. Thus, the high-frequency field gets directly into a nucleus of microorganisms, stopping its further reproduction.

## CONCLUSIONS

As a result of experiments and the analysis of physical processes, it is possible to draw the following conclusions:

1. At electronic and ion treatment of water mediums for inactivation of containing microorganisms depending on their geometrical parameters, as the influence instrument of high voltage pulses by various range are applied;
2. At treatment of fluid foodstuff for prevention of spark breakdown in interelectrode distance, secondary appearance of microorganisms in treated medium and preservation of its initial nutrition and biological properties application of nanosecond pulses is preferable.
3. Settlement formulas definitions of electric parameters of power source in dependence on electrophysical parameters of the treated medium with microorganisms which account is necessary at design of high-voltage installations of technological appointment are given.
4. Presented technology can form a basis at elaboration of technological high-voltage installations on electro pulse high frequency electronic and ion treatment of water mediums of special purpose.

- 
- [1] *G.I. Skanavi*. Physics of dielectrics (strong fields). M., 1958, p. 908.
  - [2] *K.A. Jeltov*. Picosecond electronic accelerators. M.: Energoftomizdat, 1991, p. 116. (In Russian).
  - [3] *P.N. Mathanov, L.Z. Gogolitsin*. Calculation of pulse transformers. - L.: Energy. Leningrad, 1980, p. 112. (In Russian).
  - [4] *Yu.V. Gorin, Ye.V. Dmitriev, Ch.M. Juvarli, F.H. Kulakhmetov, E.J. Gurbanov, R.N. Mekhtizadeh*. Method of electro discharge treatment of materials and the device for its implementation. Patent No. 5009479. 21. 1992.
  - [5] *Yu.V. Gorin, F.H. Kulakhmetov, E.J. Gurbanov*. Modification of composite materials surface in torch discharge. Electronic Treatment of Materials. Moldova, 1991, n. 3, p. 48.
  - [6] *V.G. Kuznetsov, A.M. Gashimov, E.J. Gurbanov*. Research of structure of nanosecond streamer discharge by elektrografiya method. Technical electrodynamics. Kiev, n. 6, 2009. p. 17-22.
  - [7] *E.J. Gurbanov*. Role of dielectric nozzles in formation of nanosecond pulse discharges in dense air. Electricity, n. 4, 2009, p. 60-65.
  - [8] *N.A. Mammadov, B.B. Davudov, K.M. Dashdamirov, G.M. Sadikhzadeh, Sh.Sh. Alekberov*. "Using of Ozone Technology during Biological and Chemical Processes and Polluted water Purification", International Journal on Technical and Physical Problems of Engineering (IJTPE), Issue 17, vol. 5, n. 4, p. 184-189, December 2013.
  - [9] *I.P. Kuzhekin, E.J. Gurbanov*. Strong electric fields and pulse discharges in water. Bulletin of MPEI, n. 2, Moscow, 2008, p. 33-36. (In Russian).
  - [10] *I.P. Kuzhekin, E.J. Gurbanov*. Pulsed discharge in water. Problems of Power Engineering, № 1, Baku, 2008, p. 103-105.
  - [11] *E.J. Gurbanov*. "Thermal and electric breakdown of water at crown and spark discharges". IJTPE, Issue 19, vol.6, n. 2, 2014, p.88-93.
  - [12] *A.M. Gashimov, E.J. Gurbanov*. The influence of high-voltage impulse treatments on biological cells. Surface Engineering and Applied Electrochemistry, v.45, n. 5, 2009. p.411-414.
  - [13] *M. Gashimov, E.J. Gurbanov*. The influence of high-voltage impulse treatments on biological cells. Surface Engineering and Applied Electrochemistry, USA, v.45, n. 5, 2009. p.411-414.
  - [14] *M.V. Volkenshteyn*. Biophysics. M.: Science, 1988, p. 592.
  - [15] *H. Hulsheger, J. Potel and E.G. Niemann*. Killing of bacteria with electric pulses of high field strength radiation and environmental biophysics. Radiation and Environmental Biophysics. 1981, vol. 20, p. 53-65.
  - [16] *A.J.H. Sale, W.A. Hamilton*. Effects of high electric fields on microorganism. III. Lysis of erythrocytes and protoplasts. Biochimica et Biophysica Acta. 1968. vol.163, n. 1, p.37-43.
  - [17] *K.M. Polyvanov*. Theoretical bases of electrical equipment, part 3. Theory of an electromagnetic field. M.: Energy, 1969. p. 352.

Received: 21.09.2015

# THERMAL CAPACITY, DEBYE TEMPERATURE AND PHASE TRANSITIONS IN $\text{TiCoS}_2$ CRYSTALS

E.M. KERIMOVA, A.M. ABDULLAYEV, M.A. ALDJANOV, M.D. NADJAFZADE,  
P.G. ISMAYLOVA, A.B. MAGERRAMOV, A.K. ZAMANOVA, G.M. AKHMEDOVA

*Institute of Physics, Azerbaijan National Academy of Sciences,  
G. Javid av., 131, Baku 1143, Azerbaijan*

This paper deals with the thermal capacity of  $\text{TiCoS}_2$  crystals abstract within 55-300K. Debye characteristic temperature is calculated. Dependence  $C_p(T)$  reveals clearly marked anomaly indicating presence of phase transition. Maximum value of anomaly is at temperature  $T_c = 111\text{K}$ . Changes of energy  $\Delta Q$  and entropy  $\Delta S$  of phase transition are defined. Small value  $\Delta S/R = 0.02$  shows that this transition belongs to ones of displacement type.

**Keywords:** Thermal capacity;  $\text{TiCoS}_2$ , Debye temperature, phase transition

**PACS:** 65.40.Ba, 65.40.Gr, 75.00

## INTRODUCTION

The compounds with general chemical formulae  $\text{TlMeX}_2$  ( $\text{Me}=\text{Co}, \text{Ni}, \text{Fe}, \text{Cr}, \text{Mn}$ ;  $\text{X}=\text{S}, \text{Se}, \text{Te}$ ) belong to class of low-dimensional magnets. The results on obtaining of such compounds and investigation of their physical properties are represented in [1-9]. Concerning to thallium-cobalt sulfide, its magnetic properties are described in [8]. In particular, the magnetization and paramagnetic susceptibility of  $\text{TiCoS}_2$  are investigated and it is shown that it is ferrimagnetics. Curie temperature and effective magnetic moment are  $\text{TiCoS}_2$  are 112K and  $4.6\mu_B$  correspondingly. The investigation of thermal capacity and thermodynamic characteristics of phase transition of given compound  $\text{TiCoS}_2$  is the aim of present work.

## EXPERIMENTAL RESULTS AND THEIR DISCUSSION

$\text{TiCoS}_2$  synthesis is carried out at interaction of initial components of high purity in quartz ampoules evacuated up to  $10^{-3}$  Pa. The technological mode of  $\text{TiCoS}_2$  synthesis is described in detail in [8]. On the basis of X-ray analysis it is established that given compound has the hexagonal structure with the following parameters of crystal lattice:  $a = 3,726 \text{ \AA}$ ;  $c = 22,510 \text{ \AA}$ ;  $z = 3$ ;

$\rho = 6,026 \text{ gr/cm}^3$ . One can suppose that  $\text{TiCoS}_2$  is quasi-two-dimensional magnet because of big ratio  $c/a$  ( $\sim 6$ ).

The investigation results of low-temperature thermal capacity of  $\text{TiCoS}_2$  anisotropic crystal in interval  $55 \div 300\text{K}$  are shown in fig.1 [10]. The thermal capacity error doesn't exceed 0.3% in whole interval of temperatures under consideration. The methodological specifics of experiments are described in details in [11].

As it is seen the thermal capacity anomaly with peak at  $T_c \approx 111\text{K}$  connected with magnetic phase transition is observed on  $C_p(T)$  dependence. The dashed line 1 in fig.1 shows the thermal capacity in Debye model  $C_D = 3nR F_D(T/\theta_D)$  where  $n$  is number per formula unit (in case  $\text{TiCoS}_2$   $n = 4$ ),  $R$  is gas constant and  $F_D(T/\theta_D)$  is Debye function [12]

$$F_D(T/\theta_D) = 3(T/\theta_D)^3 \int_0^{\theta_D/T} \frac{x^4 dx}{(e^x - 1)^2},$$

calculated for Debye characteristic temperature  $\theta_D \approx 262.5\text{K}$ . As it is seen we have the exact correspondence of thermal capacity values given by Debye theory with experimental once at temperature  $T \geq 55\text{K}$ .

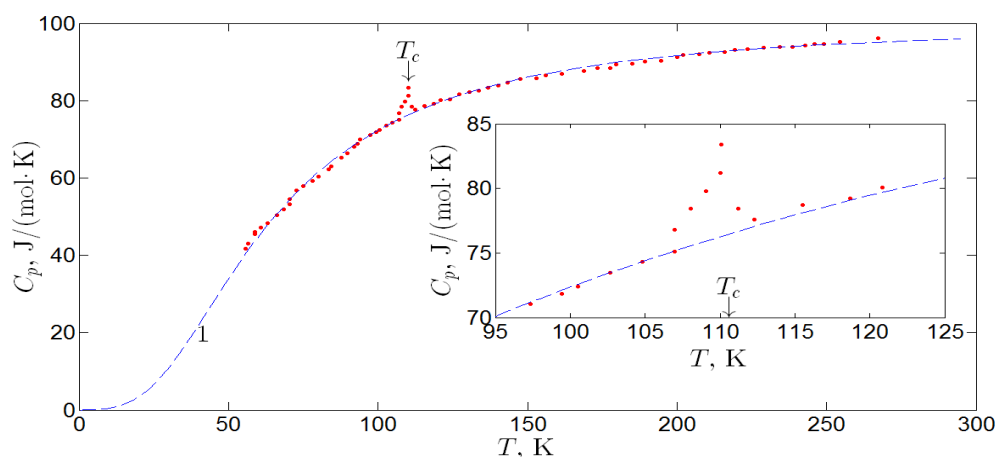


Fig. 1.  $C_p(T)$  dependence for  $\text{TiCoS}_2$ : points is experiment, 1 (dashed line) is Debye model.

The information on anomalous thermal capacity and entropy connected with is of interest at analysis of phase transition. The excess component of thermal capacity  $\Delta C_p$  is defined as difference between measured ( $C_p$ ) and calculated phonon thermal ( $C_D$  is Debye model) capacities  $\Delta C_p(T) = C_p(T) - C_D(T)$  that allows us to define and analyze the characteristics of phase transition of  $\text{TlCoS}_2$  crystal.

The peak of thermal capacity (see fig.1) at  $T_c$  is small and is about ~9% on lattice one ( $\frac{\Delta C_p(T_c)}{C_D(T_c)} \approx 9\%$ ). The series of character peculiarities: small jump at  $T_c$  and asymmetric anomaly with respect to transition temperature, is revealed on temperature dependence of  $\text{TlCoS}_2$  thermal capacity at temperatures near  $T_c$ . The phase transition at  $T_c$  can be considered as the phase transition of the second order.

The changes of ( $\Delta Q$ ) energy and ( $\Delta S$ ) entropy connected with phase transition at  $T_c$  are defined by the way of integration of cubic interpolated square splines under anomalous parts of  $\Delta C_p(T)$  and  $\Delta C_p(T)/T$  curves in interval 105 – 120K correspondingly.  $\Delta Q$  and  $\Delta S$  values are given in table. The small value of  $\Delta S/R = 0.02$  shows that the given transition belongs to transitions of displacement type.

$\Delta Q, \frac{\text{J}}{\text{mol}}$	$\Delta S, \frac{\text{J}}{\text{mol} \cdot \text{K}}$	$\frac{\Delta S}{R}$
$22.9 \pm 0.1$	$0.21 \pm 0.01$	0.02

For  $T < 55\text{K}$  temperatures there are no experimental data for thermal capacity values of  $\text{TlCoS}_2$  crystals. Debye model limitation by one characteristic temperature  $\theta_D$  is caused by the use of isotropic density of phonon state. It is obviously, that it is necessary to use the anisotropic phonon spectrum characterizing in particular by several Debye temperatures for anisotropic crystals, to which  $\text{TlCoS}_2$  belongs. Moreover, the lattice anisotropy is defined by the value, which is equal to ratio of lattice parameter in layer to parameter between layers and the difference of lattice hardness in relation to atom oscillation in layer planes and layer oscillations with respect to each other [13].

## CONCLUSION

Thus, the main influence lattice (phonon) component of  $\text{TlCoS}_2$  thermal capacity at temperature  $\geq 55\text{K}$  make the atom oscillations that can be considered in Debye approximation.

- 
- |   |   |
|---|---|
| <p>[1] M. Rosenberg, A. Knulle, H. Sabrowsky, and Chr. Platte. J. Phys. Chem. Solids 43, 87 (1982).</p> <p>[2] E.M. Kerimova, S.N. Mustafaeva, A.I. Jabbarly, G. Sultanov, A.I. Gasanov, R.N. Kerimov. New magnetic semiconductors on the base of <math>\text{TlB}^{\text{VI}} - \text{MeB}^{\text{VI}}</math> systems (Me – Fe, Co, Ni, Mn; B – S, Se, Te). Physics of Spin in Solids: Materials, Methods and Applications. NATO Science Series: II. Mathematics, Physics and Chemistry. 2004. V. 156. p. 195-206.</p> <p>[3] A.I. Djabbarli, E.M. Kerimova, F.M. Seidov, A.K. Zamanova. Neorqan. materiali 32, 118 (1996). (In Russian).</p> <p>[4] M.A. Aldjanov, M. Nadjafzade, Z. Seidov and M. Gasumov. Turkish J. Phys. 20, 1071 (1996).</p> <p>[5] E.M. Kerimova, F.M. Seidov, S.N. Mustafaeva, S.S. Abdinbekov. Neorqan. materiali 35, 157 (1999). (In Russian).</p> <p>[6] S.N. Mustafaeva, E.M. Kerimova, A.I. Djabbarli, FTT 42, 2132 (2000). (In Russian).</p> | <p>[7] S.N. Mustafaeva, E.M. Kerimova, F.M. Seidov and A.I. Jabbarly. Abstr. of 13th Inter. Conf. Ternary and Multinary Compounds–ICTMC 13. Paris, France, October 14-18 (2002) P. P2-1.</p> <p>[8] R.Z. Sadixov, E.M. Kerimova, Yu.G. Asadov, R.K. Veliev. FTT 42, 1449 (2000). (In Russian).</p> <p>[9] E.M. Kerimova, R.Z. Sadixov, R.K. Veliev. Neorqan. materiali 37, 180 (2001). (In Russian).</p> <p>[10] E.M. Kerimova, S.N. Mustafaeva, M.A. Aldjanov, A.I. Djabbarli. Fizika nizkix temperatur, 2004, t. 30, № 4, s. 395–397. (In Russian).</p> <p>[11] K.K. Mamedov, A.Yu. Yangirov, A.G. Useinov, A.M. Abdullaev. Phys. Stat. Sol. (a) 106, 315 (1988), P. 315–331.</p> <p>[12] Ch. Kittel. Vvedenie v fiziku tverdogo tela. M: Nauka, 1978. 791 S. (In Russian).</p> <p>[13] L.D. Landau, E.M. Lifshich. Teoreticheskaya fizika. T.V. Staticheskaya fizika. Ch. 1. M.: Nauka, 1976. 583 S. (In Russian).</p> |
|---|---|

Received: 14.10.2015

## THE PECULIARITY OF C ELECTRIC PROPERTIES MODIFIED BY ARGENTUM IONS

V.I. ORBUKH<sup>1</sup>, N.N. LEBEDEVA<sup>1</sup>, G.M. EYVAZOVA<sup>1</sup>, B.G. SALAMOV<sup>2,3</sup>

<sup>1</sup>*Baku State University, Az-1148, Z. Khalilov str., 23*

<sup>2</sup>*Department of Physics, Faculty of Sciences, Gazi University, 06500 Ankara, Turkey*

<sup>3</sup>*Institute of Physics of ANAS, G. Javid av.,131, Baku 1143, Azerbaijan*

*E-mail: orbukh@rambler.ru*

The conduction of clinoptilolite modified by argentums ions is investigated at room temperature. It is shown, that long-temporary (about 10 hours) kinetics of current increasing up to stationary value at constant voltage is observed, after which the stable volt-ampere characteristic takes place. It is revealed that the current doesn't decrease up to zero at air exhaust as it is observed for natural zeolite but essential residual conduction takes place. The explanation of these phenomena, based on supposition on two different argentum states in zeolite pores, is suggested.

**Keywords:** zeolite, argentum ions, volt-ampere characteristic, residual conduction.

**PACS :** 77.84.Lf; 72.80.Tm; 84.37+q

The zeolites are nano-porous materials having the developed regular system of channels and cavities of dimensions about 1 nm order, which differ by the big variety of forms and structures of zeolite different types.

The zeolites are the hydrated aluminosilicate minerals the infinite aluminosilicate frame of which forms by means of the joint of the common tops of tetrahedrons  $[\text{SiO}_4]^{4-}$  and  $[\text{AlO}_4]^{5-}$  having the interconnecting cavities, occupied by large ions and water molecules [1]. The weakly coupled cations and water molecules in zeolite porous are characterized by essential mobility that provides the possibility of ion exchange and dehydration reversibility. Moreover, it doesn't influence on aluminosilicate rigid frame. The zeolites are widely used in industry and agriculture because of above mentioned their property.

Nowadays more than 45 types of natural zeolites, from which clinoptilolite, heulandites, phyllipsite, lomonite, mordenite, erionite, chabasite, ferrierite and analcime are widely applied. The clinoptilolite is determined as series of zeolites minerals having the clear heulandite (HEU) structural topology and ratio  $\text{Si}/\text{Al} > 4.0$ .

HEU tetrahedral lattice structural topology having C2/m symmetry with flattened channels limited by to ten membered and eight membered tetrahedral rings (4.6x3.6 Å) parallel to C axis, are enough investigated. The additional eight-membered ring channels (4.7x2.8 Å) are parallel to [100] and [102] and cross with prior channels in [010] forming the system from two-dimensional parallel channels to [010] which are responsible for layered structure [1,2].

The analysis of structure and properties of zeolite allows us to consider it not only as perspective sorbent but as the object by means of which one can investigate dielectric and electric properties [4,5], the pore emission of electrons, electron multiplication and gas discharge in pores [3].

If zeolite sorption properties are defined by sizes and configurations of pores then its electric properties are defined by substance composition in pore space [6]. We have established that natural zeolite under consideration belongs to high-silica zeolites of clinoptilolite type [7] on the base of roentgenographic and spectral chemical analyses.

The channel composition presents itself the extra-frame subsystem. This is the positive charged cations  $\text{Na}^+$ ,  $\text{K}^+$ ,  $\text{Mg}^{2+}$ ,  $\text{Ca}^{2+}$  compensating the frame negative charge and the big number of  $\text{H}_2\text{O}$ -coordination water molecules also. The water plays the important role for providing of clinoptilolite frame stability and leads to increase of ion mobility in porous space as it is supposed in [8]. The weakly coupled cations and water molecules in zeolite pores lead to big values of dielectric constant on low frequencies and significant dependence of zeolite electro-physical properties on frequency and temperature. The water can be extracted at heating or evacuation of zeolite that insignificantly influence on aluminosilicate rigid frame and its structure practically doesn't change. Moreover, zeolite electric properties are defined by metal ions fully. The cation ability to diffuse through big open zeolite structure gives the possibility to obtain the high ion conduction in zeolites and to use zeolites as solid electrolytes. Last years there have been many attempts of investigations of factors, which control ion transport in external electric field [9]. These investigations are mainly focused on influence of temperature, hydration degree and metal cation nature on conduction, measured at alternating voltage. There are few investigations of zeolite electric conduction in constant voltage mode. Our work [3] on zeolite plate cut from monoblock of natural clinoptilolite; work [10] on single crystals of synthesized zeolites and work [11] on tablets of compacted power of natural zeolite belong to of these investigations. The either stationary current or continuously decaying current are observed in these works at current investigation at constant voltage. That's why the question on existing of zeolite through ion conduction at constant voltage is debatable one. In given paper we present the kinetics of stationary current establishment, which is unusual for ion conduction, in constant voltage mode in plate of clinoptilolite modified by argentums ions.

### EXPERIMENT

The clinoptilolite is chosen in the capacity of investigation object. Its syngony is the monoclinic one and space group symmetry is C2/m. The elementary cell



parameters on X-ray structural analysis data:  $a=1.761\text{nm}$ ,  $b=1.780\text{nm}$ ,  $c=0.741\text{nm}$ ,  $\beta=115.2^\circ$ . The planar plate from which the samples are cut in the form of tablets of following dimensions: thickness is  $2.3 \times 10^{-3}\text{ m}$ , big face square  $S=18.75 \times 10^{-6}\text{m}^2$ , is cut out from zeolite monoblock for experiment. The electrodes are brake polished metal discs. The anode is prepared from stainless steel and cathode from brass. The ion-exchange method when the plate is put in 1M solution of nitric-acid argentum, further is washed in deionized water and is dried at  $100^\circ\text{C}$  is applied for modification by argentum ions.

The constant voltage from stabilized power supply is applied to electrodes. The current in sandwich mode is measured at voltage across electrodes 50V in air with humidity 80% at room temperature

## RESULTS AND DISCUSSION

- The existence of argentum ions in modified zeolite reveals at comparison of resistances of modified and natural zeolites on low (500Hz) frequency. The resistance of modified sample is in 100 times less than natural one.
- The time dependence which is unusual for ion conduction in constant electric field is revealed. The current linearly increases with time and takes the saturation value ( $3 \times 10^{-4}\text{ A}$ ) in 10 hours
- The saturation current dependence on voltage across electrodes is close to linear one and is similar at voltage change from 50V up to 200V and from 200V up to 50V.
- The current dependence on pressure which is unusual for zeolite is observed. The residual conduction value remains constant ( $1 \times 10^{-5}\text{ A}$ ) at air exhaust from atmosphere pressure up to  $10^{-2}$  torus.

It is experimentally established that the zeolite modified by argentum has the long-term dynamics. The zeolite is kept 4 days in small electric field (50V) demonstrating the monotonous current increase from  $3.5 \times 10^{-5}\text{A}$  up to saturation value  $32 \times 10^{-5}\text{A}$  (fig.1). After such procedure, the current remains stationary one and the observable volt-ampere characteristic is non-inertial and reversible one at field change (fig.2). The sample returns to initial state after several days at the absence of electric field. The monotonous current increase is revealed at repetitive sample storage in the same field. The air exhaust from camera consisting of the sample begins at the moment when the current achieves its stationary value. The current decreases up to stationary value  $5 \times 10^{-5}\text{A}$  in the process of residual pressure decrease up to  $10^{-2}$  torus that is confirmed the existence of zeolite stable residual conduction at absence of water vapors in pores. Let's formulate the obtained results by the following way for their discussion.

It is established that zeolite (in pores of which the argentum ions locate) can be in two states. The first (ground) state is the state in which it transits after long time after electric field isolation. The second state is the state in which it transits from first one in electric field. If the monotonously increasing current is observed in electric field in first state, then current is stationary one and observable volt-ampere characteristic is stable one in the second state. The current increases on one order at

transition from the first state to the second one. It is also established that the transition from the second state to the first one can take place at once as the air is exhausted from the camera containing the sample. Note that this process takes about several days at atmosphere pressure.

First, for natural zeolite the air exhaustion from camera containing the zeolite always leads to collapse of conduction. It can be explained by the fact that the ion in zeolite pore can be in two states. Firstly, this ion is connected only with pore wall. In these states the ions don't have the mobility and that's why don't make the contribution in current. Secondly, this state when the ion connection with pore walls weakens and ions become mobile ones and give contribution in current because of interaction with water molecules.

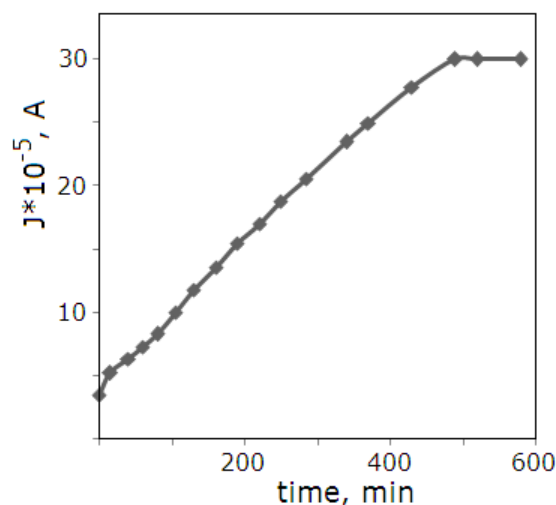


Fig. 1. The dependence of current on time.

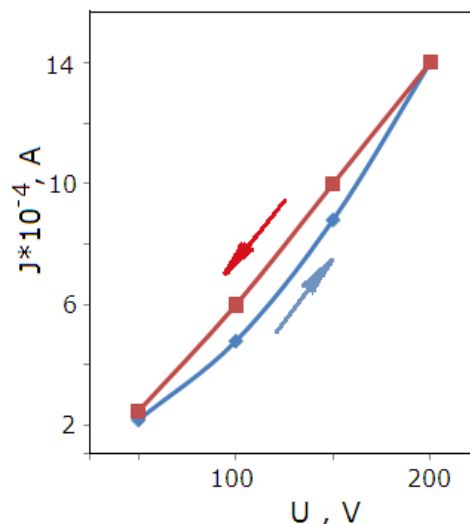


Fig. 2. Volt-ampere characteristic for saturation current.

Let's try to modify this standard scheme for our experiment. As the ion conduction decreases at air exhaust from camera but not disappears then we suppose that argentum ions connected with zeolite pore walls have the mobility even in absence of water (as opposed to natural zeolite ions). At atmosphere pressure the zeolite (with argentum ions in pores) transits to the state with the same

conduction which it has after air exhaust from camera containing the zeolite sample after collapse of the electric field. So we conclude that the argentine ions form the connection with pore walls without water in spite of its presence at atmosphere pressure in spite of presence of steams in zeolite pores. Thus, we supposed that argentine ions in zeolite pores (also as ions in natural zeolite) are in two states. The first state is the bound state of argentine ion with pore wall without water molecules. The second one is the bound state of argentine ion with pore walls with water molecules. If in natural zeolite the second state always forms when there is water in the pores then in zeolite with argentine ions is vice versa, the first state is the ground one (bound ion state without water molecules). The transition in second state is possible only after long storage in electric field (slowly increasing current with transition in saturation current fig.1). Moreover, this state isn't equilibrium one, it decays and ions goes to first state after long time (days) after field switching off. Thus, we explain the observable current dependence on time: the long-term increase of current with following transition to saturation one is

observed. In electric field the ions transit to state when the water molecules take part in ion bond with pore wall, i.e. it takes place for zeolite not modified by argentine without external field.

## CONCLUSION

In present paper it is established that the argentine ions in zeolite pores can be in two states. The first state is the bound state of argentine ions with pore surface without water molecules. In this state ions have the mobility enough for current restoracia after air exhaustion. The second state is that one in which the water molecules take part, in this state the mobility strongly increases. The transition from the first state in second one takes place in the result of long storage in electric field. The reverse transition from second state to first one can take place by two methods. The first method is rapid one (2-3 hours). It is air exhaustion from camera. The second method is slow (several days). It is isolation the field in long time.

- 
- [1] *G. Gottardi and E. Galli.* Natural Zeolites. Berlin: Springer-Verlag, 409 (1985)
  - [2] *Ch. Baerlocher, W.M. Meier, D.H. Olson.* Atlas of Zeolite framework Types, Revised. Amsterdam: Elsevier, (2001).
  - [3] *N.N. Lebedeva, V.I. Orbukh, Ch.A. Sultanov.* Gazorazryadnaya sistema s tseolitovim 'lektrodom. JTF, 2010, 80 (4) 134. (in Russian).
  - [4] *S.V. Barishnikov, S.V. Lankin, E.V. Sturkova, V.V. Yurkov.* Vliyanie tipa iona na dielektricheskie svoystva klinoptilolita. Sovremennye naukoymkie tekhnologii, 2004, 6, 26-27. (in Russian).
  - [5] *V.V. Yurkov, S.B. Lankin, S.B. Barishnikov, L.G. Kolesnikova, L.I. Roqulina, A.V. Serov.* Cheoliti Amurskoy oblasti, Vestnik DVO RAN, 1, 69-79 (2004). (in Russian).
  - [6] *V.N. Boqomolov.* Jidkosti v ultratonkix kanalex (nityanie i klasternie kristalli, UFN, 124 (1) 171-182 (1978). (in Russian).
  - [7] *T.Z. Guliyeva, N.N. Lebedeva, V.I. Orbukh, Ch.A. Sultanov,* Natural ztolite-rlinoptilolit Identification, Fizika, 15(3) 43-45 (2009).
  - [8] *V.G. Solovov.* «Eksperimentalnie issledovaniya fizicheskix svoystv reqluyarnix matrichnix kompozitov i sloistix sistem s nanostruktuirovannimi neorqanicheskimi I orqanicheskimi veshestvami», Avtoreferat dissertachii, Sankt-Peterburq, 37 (2005). (in Russian).
  - [9] *J.M. Kalogeras, A. Vasslicou-Dova.* Molecular Mibility in Microporous Architectures: Conductivity and Dielectric Relaxation Phenomena in Natural and Synthetic Zeolitas, Cryst. Res. Technol., 31, 693-726 (1996).
  - [10] *V.L. Veysman, V.N. Markov, L.V. Nikolaevna, S.V. Pankova, V.G. Solovov.* Provodimost monokristallov cheolitov, FTT, 35 (5) 1390-1393 (1993). (in Russian).
  - [11] *A.K. Jonscher, A.R. Haidar.* The Time-Domain Response of Humid Zeolites, J.Chem.Soc.Faraday. Trans. 1, 82 (12) 3553-3560 (1986).

*Received: 07.09.2015*

# OPTIMIZATION AND CHARACTERIZATION OF SEMIPOLAR MOVPE AND HVPE GROWTH (11-22) InGaN/(In)GaN QUANTUM WELL HETEROJUNCTIONS

S. ABDULLAYEVA<sup>1,2</sup>, G. GAHRAMANOVA<sup>1,2</sup>, R. JABBAROV<sup>1,2</sup>

<sup>1</sup>*Institute of Physics, Azerbaijan National Academy of Sciences, G. Javid av., 131, Baku 1143, Azerbaijan*

<sup>2</sup>*R&D Center for High Technologies Ministry of Communications and High Technologies of Azerbaijan*

Email: [gulnaz.qehremanova@hotmail.com](mailto:gulnaz.qehremanova@hotmail.com)

The optimization and characterization of the MOVPE (Metal Organic Vapour Phase Epitaxy) and HVPE (Hydride Vapour Phase Epitaxy) growth semi-polar (11-22) In<sub>0.15</sub>Ga<sub>0.85</sub>N/(In)GaN quantum well heterojunctions have been investigated. Two basically different approaches have been discussed, the epitaxial growth of (11-22) oriented semi-polar InGaN QWs with small indium flows during the growth of the barriers and without indium in the barriers have been explored.

**Keywords:** Quantum wells, III-N heterojunction, semipolar, InGaN, LED, MOVPE, HVPE.

**PACS:** 78.20.±e, 81.05.Ea, 81.10.±h

## 1. INTRODUCTION

III-Nitride semiconductors have significant applications for solid state lighting (SSL) [1, 2], laser diodes [3–9] and solar cells [10–12] over the last 2–3 decades. Light emitting diode (LED) has many features over the conventional light sources, such as high power efficiency and long lifetime. Currently, GaN based LED is the core technology for SSL. Possible, in the near future, GaN LEDs will significantly penetrate the general lighting market. For this purpose, high efficiency, high brightness, and low cost are the fundamental requirements for GaN-based solid state lighting.

The InGaN quantum wells (QWs) employed as active region for nitride LEDs cover the wide spectral regime from near ultraviolet to near infrared [3–9], where mainly the In content defines the emitted wavelength. Unfortunately, the optical performance of these devices typically degrades with increasing In content in these layers, leading to the so-called “green gap” [1]. In addition, the external quantum efficiency (EQE) in InGaN QWs LEDs decreases significantly in green wavelength range due to high dislocation density results from the lattice mismatch between the sapphire substrate and GaN / InGaN leading to large non-radiative recombination rate, and charge separation from the polarization fields in the QW leading to reduction of the electron-hole wave function overlap and radiative recombination rate in particular for green-emitting QWs.

Indeed, semipolar InGaN/GaN QWs are interesting compromise for achieving emission in the green–yellow region. The semipolar (11-2 2) plane, inclined by 60° with respect to the polar c-plane, has substantially reduced piezoelectric polarization compared to the c-plane, and indium incorporation efficiency on the (11-2 2) plane is reported to be comparable with c-plane [13]. These factors have enabled the demonstration of (11-2 2) LEDs at blue, green, and amber wavelengths [15]. Ultimately, nonpolar and semipolar nitrides may play a role in enabling both LEDs and laser diodes in the green–yellow region. Improvements in longer wavelength device efficiencies as well as sustained development of larger-area, high-quality

nonpolar substrates, will be more successful for commercial success.

In general, c-plane InGaN/GaN MQW structure is widely used in blue and green light emitting diodes (LEDs) [15]. However, in the c-plane polar structure of InGaN/GaN quantum wells (QWs), strong spontaneous and piezoelectric polarizations exist [16]. These polarizations lead to large electric fields separating electron and hole wave functions [17]. Therefore, the radiative recombination lifetime in the films increases, and raises the probability of non-radiative recombination and decreases the achievable internal quantum efficiency in InGaN/GaN quantum wells [18–19]. To solve these problems, same research groups have studied non-polar [20–21] and semipolar GaN and InGaN/GaN QWs [22–24].

## 2. EXPERIMENTAL

### 2.1 Substrate preparation

In the prepare process of the semipolar (11-22) structures, r-plane (10-12) sapphire substrate is used. The semi-polar (11-22) QWs orientation and related r-plane (10-12) sapphire substrate have a tilting angle with respect to the c-plane (0001), respectively 58,4° and 57,6°.

In the photolithography process, a negative nLOF2070 photoresist has been used and the substrate is rotated. By choosing a high speed of the rotation the thin photoresist was spread on the substrate the substrate was covered by photoresist. Then the sample was baked (2 min). In the next step the PR was exposed by UV light using MC-STRIPES-303 mask (exposure time was 3 sec). (Therefore, the exposed parts of the photoresist to the UV light become less soluble in chemical developer.) After exposing, the sample is baked (60sec) and then an unexposed parts of the photoresist to the UV light is removed by AZ-MIF-826 chemical developer (27sec). In the next step via Reactive Ion Etching an optimum for the pressure an etching time was found as a 15 min at 10mTor and 20 min at 20mTor. Hence, the desired angle of trench side –wall was achieved. After RIE, in order to remove the photoresist mask stripes on the substrate first oxygen plasma cleaning was done. Then in the chemical solutions

of KOH and H<sub>2</sub>O and then of H<sub>2</sub>SO<sub>4</sub> and H<sub>2</sub>O<sub>2</sub> with respectively 1 min and 4 min the sample was cleaned completely from residuals. Then the silicon dioxide (SiO<sub>2</sub>)

was sputtered on top of the sample (or c-plane facet) a mask to get covered with SiO<sub>2</sub> to avoid parasitic growth (Fig.1).

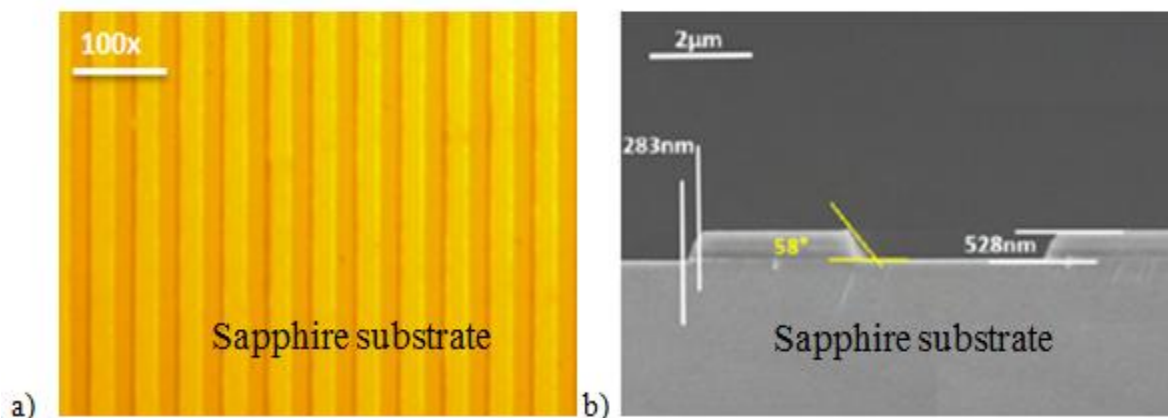


Fig. 1. Demonstration of patterning sapphire substrate with 6  $\mu\text{m}$  periodicity of trenches (3  $\mu\text{m}$  opening and 3  $\mu\text{m}$  grooves) by Optic microscope (a) and SEM investigation from the cross section of r-plane sapphire substrate after photolithography process for growing semipolar (11-22) GaN structures.

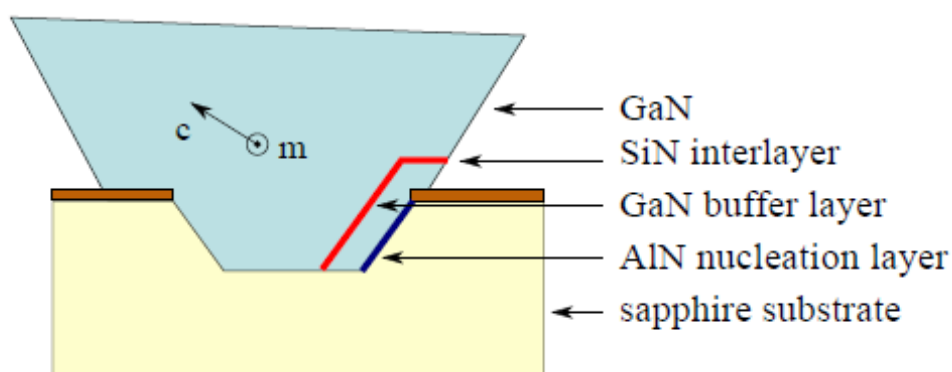


Fig. 2. Schematic structure of a single GaN on r-plane pre-structured sapphire wafers eventually coalesce to a closed layer with a (11-22) semipolar surface.

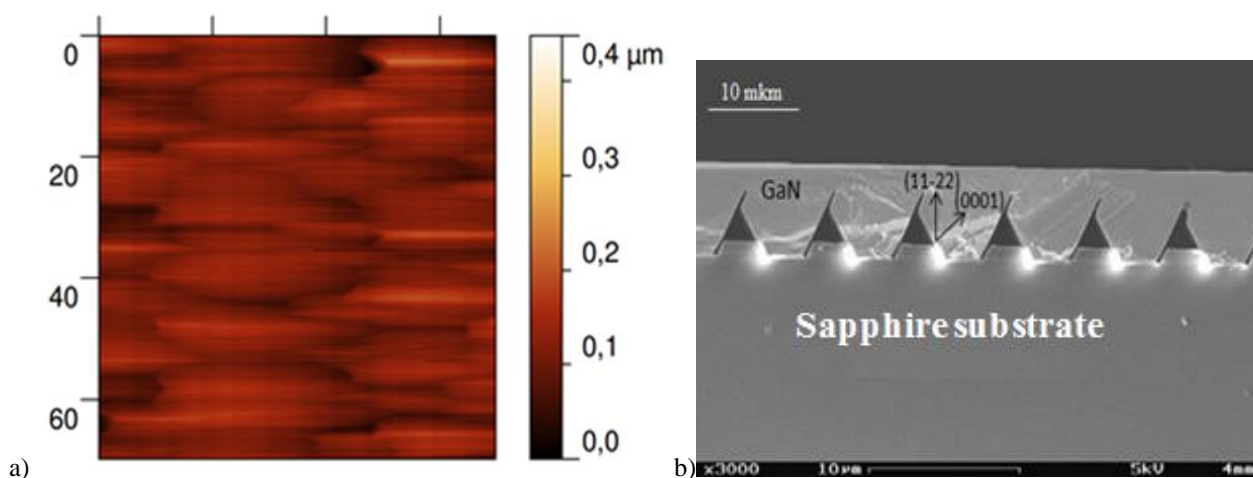


Fig. 3 Atomic force microscopy (AFM) measurement in an area of  $70\mu\text{m} \times 70\mu\text{m}$  and cross section SEM investigation of the (11-22) GaNgrown by MOVPE.

## 2.2 Structuring process and growth of (11-22)GaN.

The MOVPE growth was done in a commercial Aixtron-200/4 RF-S HT reactor using the standard precursors ammonia (NH<sub>3</sub>), trimethylgallium (TMGa), trimethylaluminum (TMAI), trimethylindium (TMIn) and Silan (SH<sub>4</sub>). The growth starts with our about 20nm thick standard AlN nucleation layer at relatively low temperature of about 950°C [25]. On such a typically 3μm thick GaN layer with a dislocation density of about  $5 \times 10^8 \text{cm}^{-3}$  [30] For the subsequent GaN growth, a reactor temperature of about 1020°C is chosen. The GaN gets pushed in c-direction and builds triangularly formed stripes, which coalesce after a suitable growth time to a planar, semipolar (11-22)-oriented surface. An in-situ deposited SiN interlayer helps to improve the crystal quality by stopping defects penetrating to the sample surface [13]. By decreasing the growth temperature of the topmost GaN layer to 970°C, the growth gets pushed further in c direction and the coalescence of the stripes gets improved. The total thickness of the GaN layer is about 2μm (Fig 2). X-ray rocking curve measurements give a FWHM of about 200arcsec for the (11-22) reflection indicating a suitable crystal quality. Atomic force microscopy (AFM) measurements show a surface roughness of 25 nm in an area of 70μm × 70μm and cross section SEM investigations have done (Fig.3a,b).

The growth of GaN substrates by HVPE was performed in a commercial Aixtron single-wafer HVPE system with a horizontal quartz-tube [28, 29]. 2μm thick GaN layer has been deposited at a fairly low growth temperature of 900 - 970°C. In<sub>0.15</sub>Ga<sub>0.85</sub>N/GaN and In<sub>0.15</sub>Ga<sub>0.85</sub>N/ In<sub>0.01</sub>Ga<sub>0.99</sub>N QWs have been deposited on top of the MOVPE and HVPE growth template by MOVPE. The deposition of the InGaN/GaN QWs was done at the same time for both 2 quarter MOVPE and HVPE growth samples.

## 2. RESULTS AND DISCUSSIONS

In order to achieve fairly long wavelength above 500 nm, the QWs were grown at a temperature of typically 720°C, while the temperature was increased by about 35°C for the barrier growth. Using the same growth conditions InGaN QWs were investigated by adding a small In flow of about 2 μmole/min to the barrier growth. In figure 4, the low temperature PL spectra of the four different samples are described. As shown, PL emission intensity was significantly increased (3-6 times) with using small In flow (1%) in barrier. However, for HVPE growth QWs the emission wavelength is longer compared to the MOVPE growth samples.

Top view cathodoluminescence (CL) investigations at 10 K show a dominating emission at about 500 nm for MOVPE growth samples (Fig 5c,d) and about 520nm for HVPE growth samples (Fig 5a,b). In the range of CL measurement, the MOVPE growth samples seems fairly homogeneous to compare with HVPE growth samples (Fig 5) and the emission intensity increases rapidly of the QWs using small In flow in the barrier. (Fig. 6).

## 3. CONCLUSION

Using r-plane (10-12) patterned sapphire substrates, we were able to grow suitable planar semipolar (11-22) 5 period InGaN/(In)GaN quantum wells on the top HVPE and MOVPE growth (11-22) GaN templates. Using an InGaN barrier in the active region investigations show a factor of 6 more intense QW emission at 500 nm at low temperature PL measurements using an optimized In flow of 53 μmole/min in the QW and 2 μmole/min (1%) in the barrier. Low temperature CL measurements show the emission intensity increases rapidly of the QWs for MOVPE growth 5 period InGaN/(In)GaN QWs. SEM and AFM measurements were done for the samples.

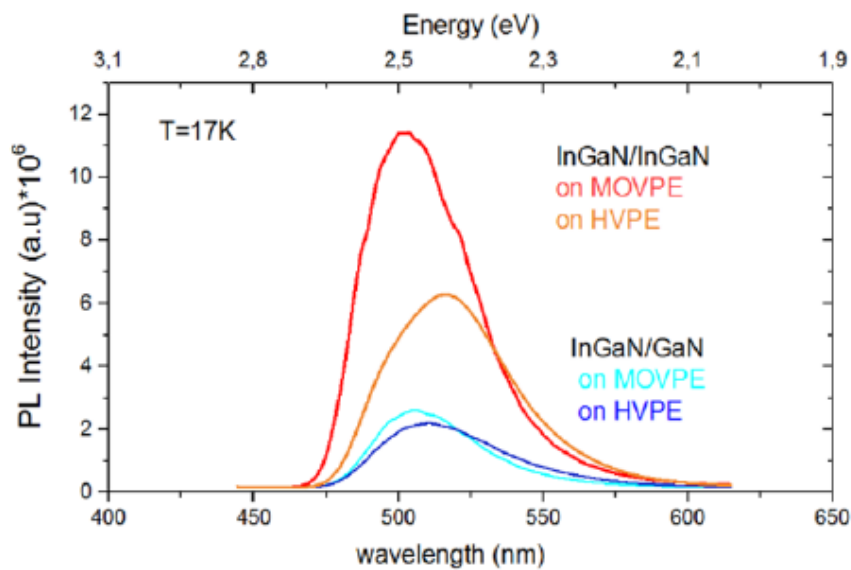


Fig. 4. Low temperature PL measurements of 5period semipolar (11-22) InGaN/(In)GaN QWs which, have been deposited on top of the MOVPE and HVPE growth template.



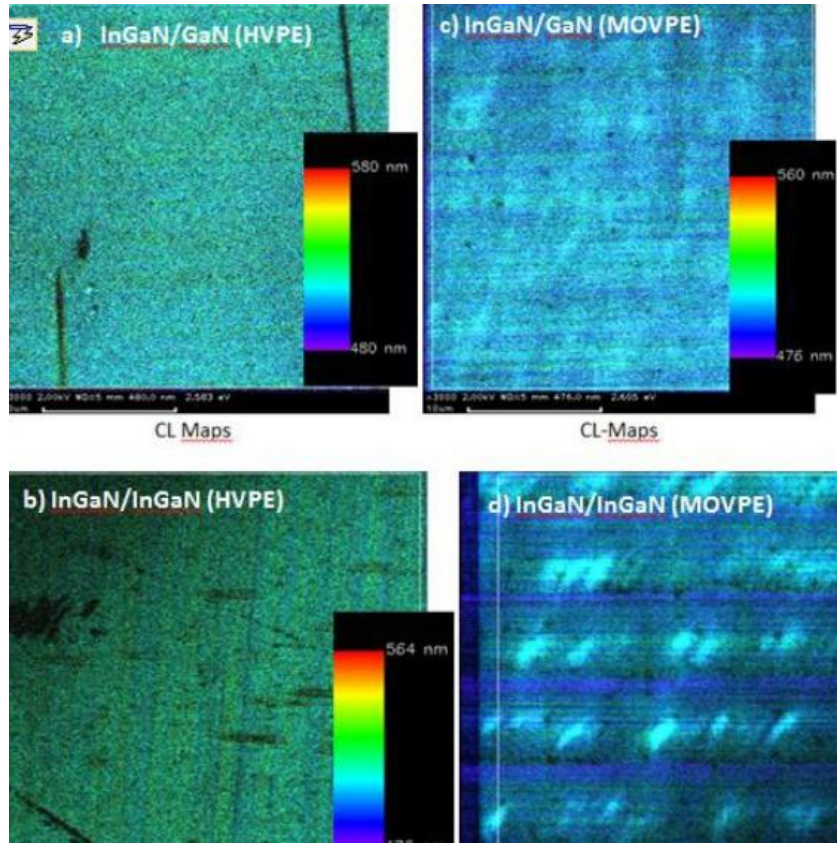


Fig. 5. Top-view SEM-CL measurements at low temperatures (10 K): a) HVPE growth  $\text{In}_{0.15}\text{Ga}_{0.85}\text{N}/\text{GaN}$ , b) HVPE growth  $\text{In}_{0.15}\text{Ga}_{0.85}\text{N}/\text{In}_{0.01}\text{Ga}_{0.99}\text{N}$ , c) MOVPE growth  $\text{In}_{0.15}\text{Ga}_{0.85}\text{N}/\text{GaN}$ , d) MOVPE growth  $\text{In}_{0.15}\text{Ga}_{0.85}\text{N}/\text{In}_{0.01}\text{Ga}_{0.99}\text{N}$ .

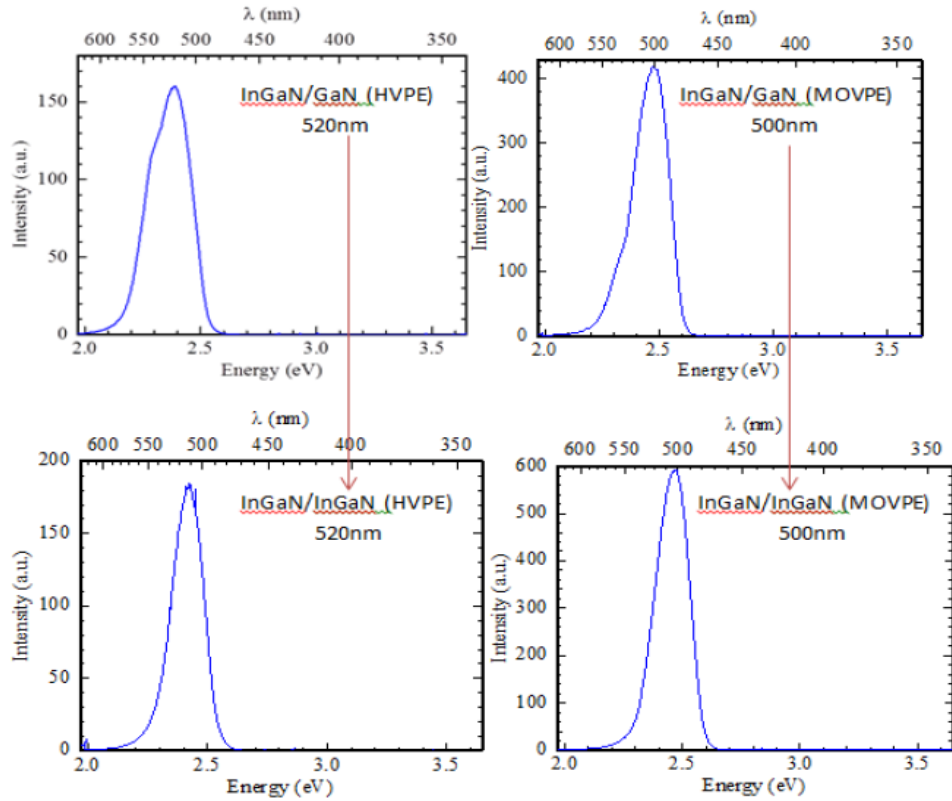


Fig. 6. The low temperature (10K) CL intensity of the semipolar (11-22)  $\text{InGaN}/(\text{In})\text{GaN}$  QWs.

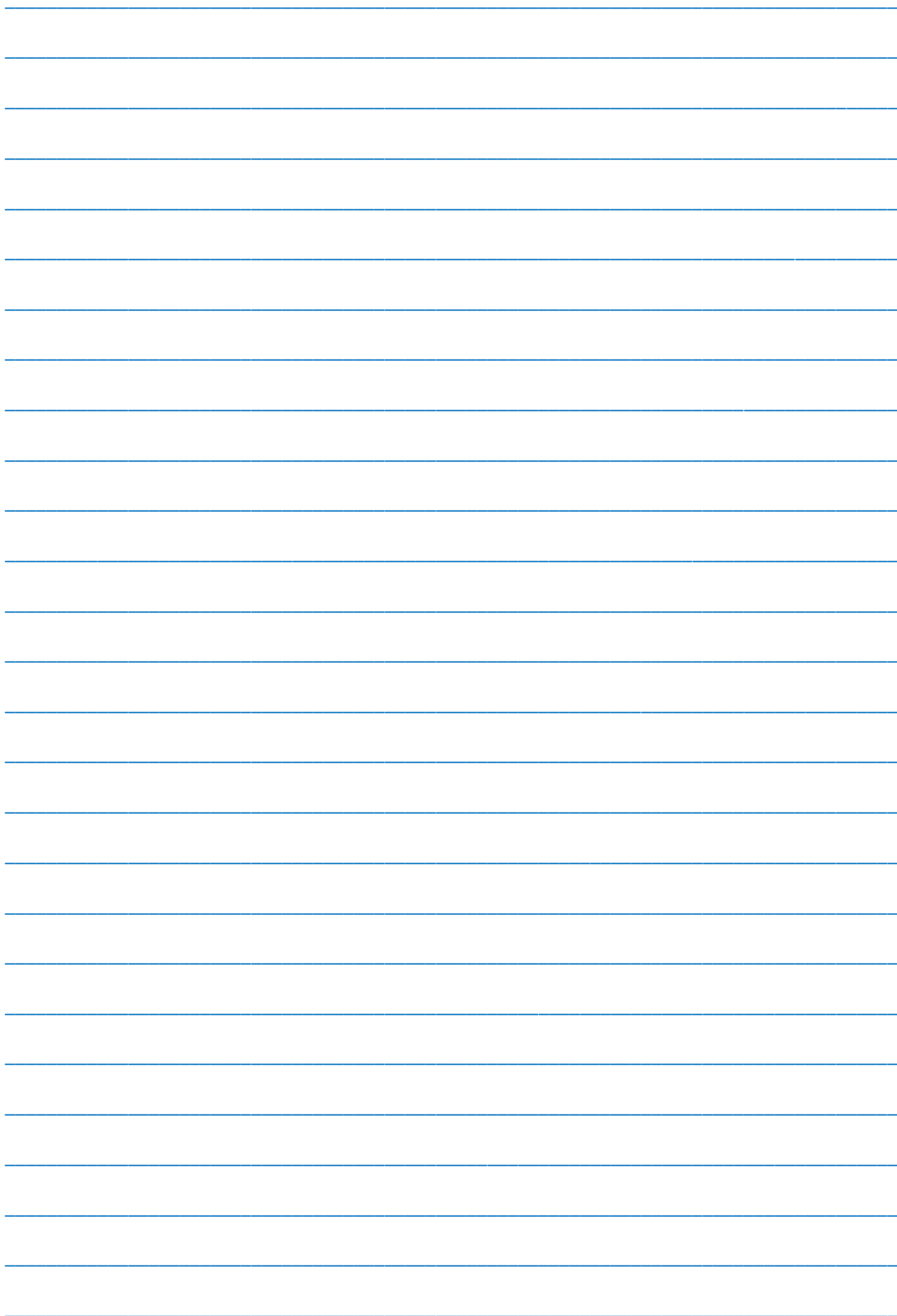
## ACKNOWLEDGMENT.

This work has been financially supported by the German Academic Exchange Service (DAAD). The authors gratefully acknowledge the frequently helpful

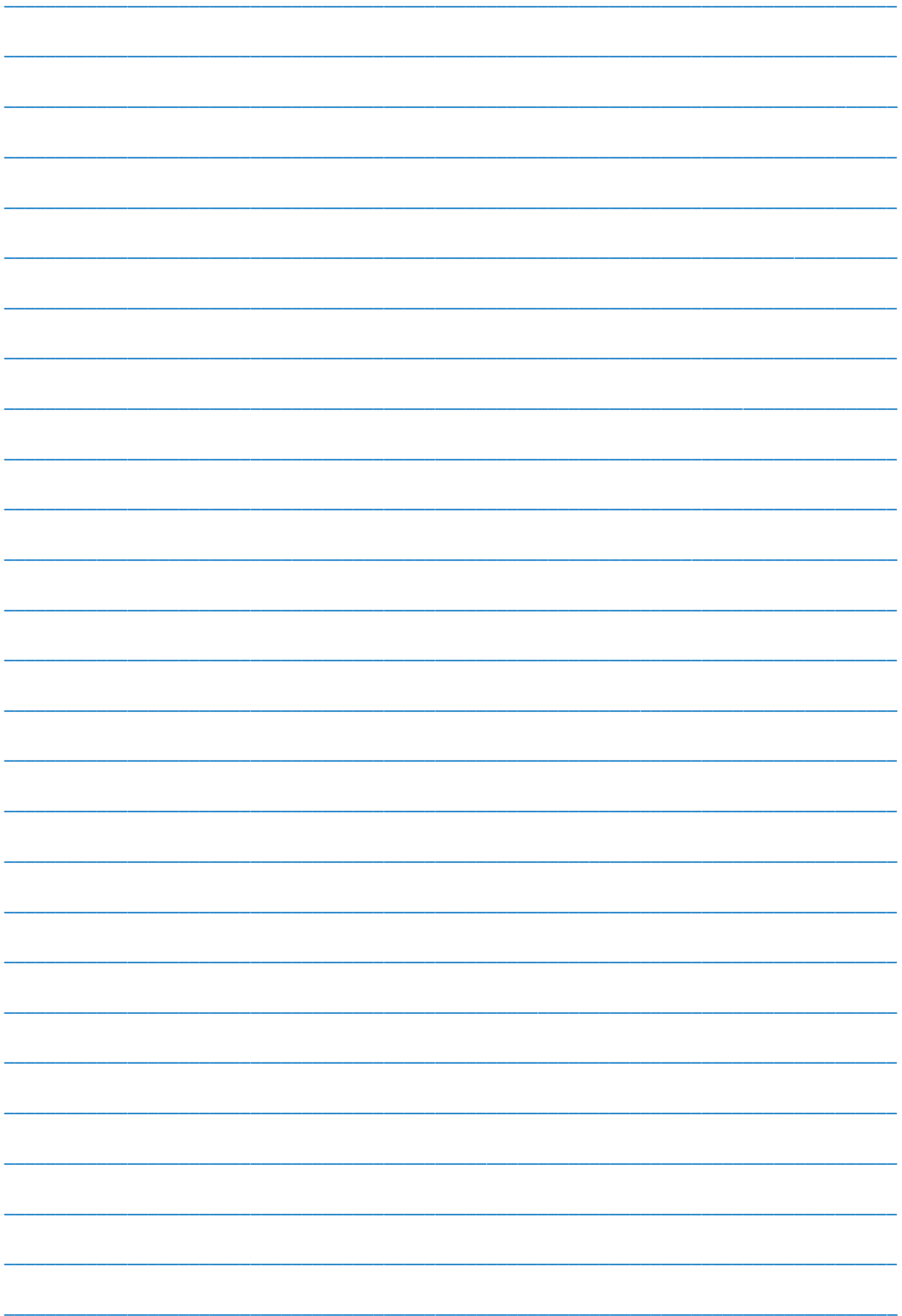
discussions with prof. Dr. F. Scholz, the discussion and the technical support from T. Meisch from Institute of Optoelectronics, Ulm University, Germany, the CL measurement by Dipl. Phys. M. Hocker from Institute of Quantum Matter, Ulm University.

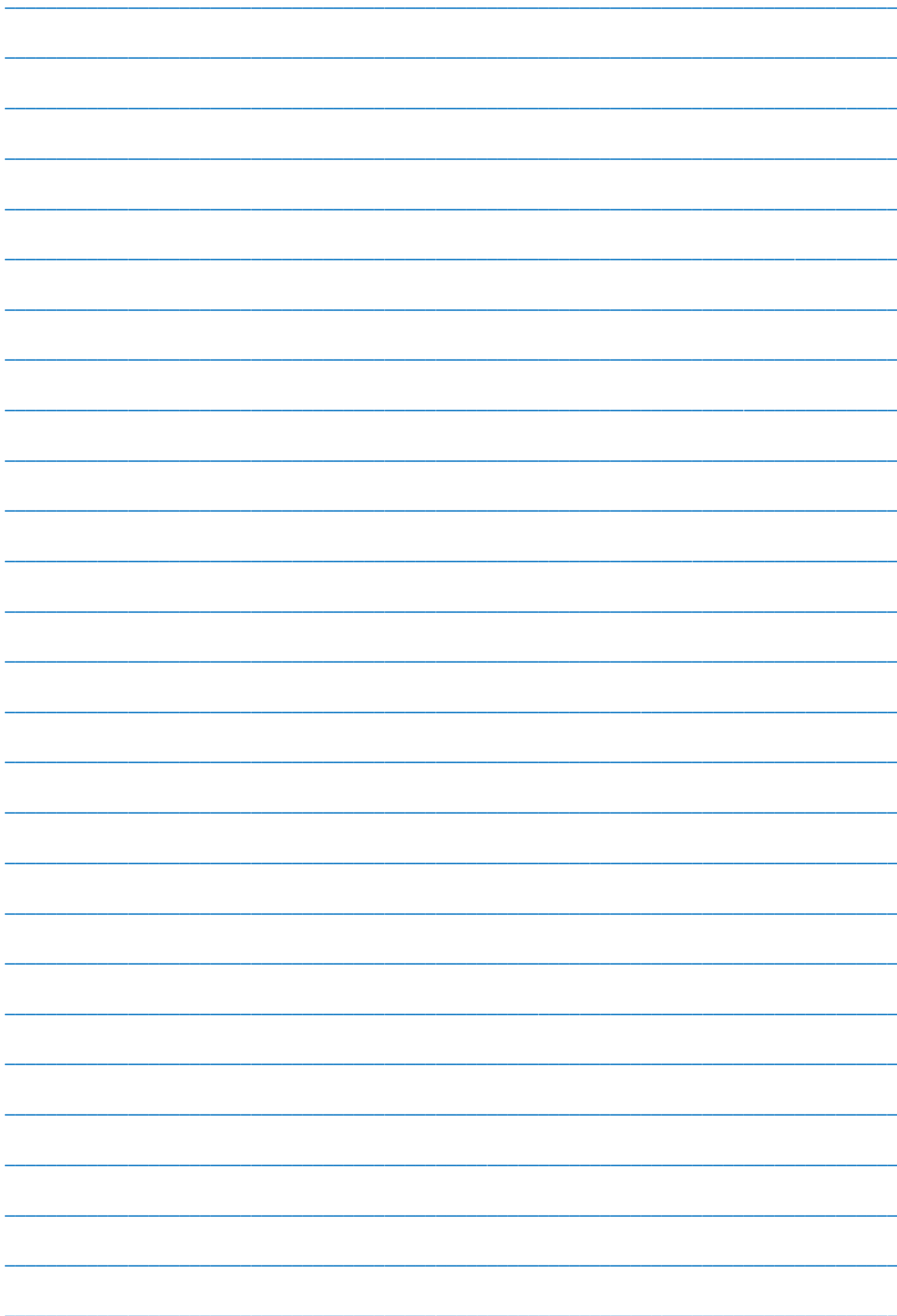
- [1] S. Nakamura. MRS Bull. 34, 101–107 (2009).
- [2] I. Ho and G.B. Stringfellow. Appl. Phys. Lett. 69, 2701–2703 (1996).
- [3] S.J. Chang, W.C. Lai, Y.K. Su, J.F. Chen, C.H. Liu, and U.H. Liaw. IEEE J. on Selected Topics in Quantum Electronics. 8 (2002) 2.2. T. Mukai, M. Yamada and S. Nakamura, Jpn. J. Appl Phys. 38 (1999) 3976-3981.
- [4] D. Queren, A. Avramescu, G. Brüderl, A. Breidenassel, M. Schillgalies, S. Lutgen, and U. Strauß. “500 nm electrically driven InGa<sub>N</sub> based laser diodes,” Appl. Phys. Lett. 94(8), 081119 (2009).
- [5] K. Okamoto and Y. Kawakami. “High-efficiency InGa<sub>N</sub>/Ga<sub>N</sub> light emitters based on nanophotonics and plasmonics,” IEEE J. Sel. Top. Quantum Electron. 15(4), 1199–1209 (2009).
- [6] T. Jung, L.K. Lee, and P.-C.Ku. “Novel epitaxial nanostructures for the improvement of InGa<sub>N</sub> LEDs efficiency,” IEEE J. Sel. Top. Quantum Electron. 15(4), 1073–1079 (2009).
- [7] X. Li, S.G. Bishop, and J.J. Coleman. “Ga<sub>N</sub> epitaxial lateral overgrowth and optical characterization,” Appl. Phys. Lett. 73(9), 1179–1181 (1998).
- [8] J. Liu, J. Limb, Z. Lochner, D. Yoo, J.-H. Ryou, and R.D. Dupuis. “Green light-emitting diodes with p-InGa<sub>N</sub>:Mg grown on C-plane sapphire and Ga<sub>N</sub> substrates,” Phys. Status Solidi., A Appl. Mater. Sci. 206(4), 750–753 (2009).
- [9] G.R. Mutta, P. Ruterana, J.L. Doualan, M.P. Chauvat, F. Ivaldi, S. Kret, N.A.K. Kaufmann, A. Dussaigne, D. Martin, and N. Grandjean. “Investigation of the In composition in InGa<sub>N</sub>/Ga<sub>N</sub> quantum wells deposited by MOVPE and/or MBE with emission from violet to green,” Phys. Status Solidi, B Basic Res. 248(5), 1187–119 (2011).
- [10] R. Dahal, B. Pantha, J. Li, J. Y. Lin, and H. X. Jiang. “InGa<sub>N</sub>/Ga<sub>N</sub> multiple quantum well solar cells with long operating wavelengths,” Appl. Phys. Lett. 94(6), 063505 (2009).
- [11] C.J. Neufeld, N.G. Toledo, S.C. Cruz, M. Iza, S.P. DenBaars, and U.K. Mishra. “High quantum efficiency InGa<sub>N</sub>/Ga<sub>N</sub> solar cells with 2.95 eV band gap,” Appl. Phys. Lett. 93(14), 143502 (2008).
- [12] O. Jani, I. Ferguson, C. Honsberg, and S. Kurtz. “Design and characterization of Ga<sub>N</sub>/InGa<sub>N</sub> solar cells,” Appl. Phys. Lett. 91(13), 132117 (2007).
- [13] H. Sato, A. Tyagi, H. Zhong, N. Fellows, R.B. Chung, M. Saito, K. Fujito, J.S. Speck, S.P. DenBaars, and S. Nakamura. “High power and high efficiency green light emitting diode on free-standing semipolar (1 1  $\bar{1}22$ ) bulk Ga<sub>N</sub> substrate,” Phys. Status Solidi (RRL), vol. 1, no. 4, pp. 162–164, 2007.
- [14] M. Funato, M. Ueda, Y. Kawakami, Y. Narukawa, T. Kosugi, M. Takahashi, and T. Mukai. “Blue, green and amber InGa<sub>N</sub>/Ga<sub>N</sub> light-emitting diodes on semipolar {11 $\bar{1}2$  2} Ga<sub>N</sub> bulk substrates,” Jpn. J. Appl. Phys., vol. 45, pp. L659–L662, 2006
- [15] T. Mukai, M. Yamada and S. Nakamura. Jpn. J. Appl. Phys. 38 (1999) 3976-3981.
- [16] O. Ambacher, R. Dimitrov, M. Stutzmann, B.E. Foutz, M.J. Murphy, J.A. Smart, J.R. Shealy, N.G. Weiman, K. Chu, M. Chumbes, B. Green, A.J. Sierakowski, W.J. Schaff, and L.F. Eastman. Phys. Stat. Sol. (b) 216 (1999) 381.
- [17] M.B. Nardelli, K. Rapcewicz, and J. Bernholc. Appl. Phys. Lett. 71 (1997) 21.
- [18] P. Waltereit, O. Brandt, A. Trampert, H.T. Grahn, J. Menniger, M. Ramsteiner, M. Reiche & K.H. Ploog. Nature. 406 (2000) 24.
- [19] A.E. Romanov, T.J. Baker, S. Nakamura, and J.S. Speck. J. Appl. Phys. 100 (2006) 023-522.
- [20] S.M. Hwang, Y.G. Seo, K.H. Baik, I.S. Cho, J.H. Baek, S.K. Jung, T.G. Kim, and M.W. Cho. Appl. Phys. Lett. 95 (2009) 071-101.
- [21] K. Iso, H. Yamada, H. Hirasawa, N. Fellows, M. Saito, K. Fujito, S. P. Denbaars, J.S. Speck, and S. Nakamura. Jpn. J. Appl. Phys. 46 (2007) L960-L962.
- [22] R. Sharma, P.M. Pattison, and H. Masui. Appl. Phys. Lett. 87 (2005) 231-110.
- [23] D.S. Oh, J.J. Jang, O.H. Nam, K.M. Song, S.N. Lee. J. Cryst. Growth. 326 (2011) 33-36.
- [24] F. Scholz, S. Schwaigery, J. Daublerz, I. Tischer, K. Thonke, S. Neugebauer, S. Metzner, F. Bertram, J. Christen, H. Lengner, J. Thalmair, and J. Zweck. Phys. Status Solidi B 249, No. 3, 464–467, 2012
- [25] J. Hertkorn, P. Brückner, S. Thapa, T. Wunderer, F. Scholz, M. Feneberg, K. Thonke, R. Sauer, M. Beer, and J. Zweck. J. Cryst. Growth 308, 30–36 (2007).
- [26] Aisaka, T. Tanikawa, T. Kimura, K. Shojiki, T. Hanada, R. Katayama, and T. Matsuoka. Jpn. J. Appl. Phys. 53, 0855011–4 (2014).
- [27] J. Wang, T. Meisch, and F. Scholz. Phys. Status Solidi B, DOI 10.1002/pssb.201552187 (2015), submitted.
- [28] Caliebe, T. Meisch, B. Neuschl, S. Bauer, J. Helbing, D. Beck, K. Thonke, M. Klein, D. Heinz, and F. Scholz. Phys. Status Solidi C 11, 525–529 (2014).
- [29] T. Meisch, M. Alimoradi-Jazi, M. Klein, and F. Scholz. Phys. Status Solidi C 11, 537–540.
- [30] F. Scholz, M. Caliebe, G. Gahramanova, D. Heinz, M. Klein, R.A. Leute, T. Meisch, J. Wang, M. Hocker, and K. Thonke. Semipolar Ga<sub>N</sub>-based heterostructures on foreign substrates, Phys. Status Solidi B 253, n.1, 13–22, 2015.

Received: 10.12.2015









## CONTENTS

1.	Polarization properties of TlGaSe <sub>2</sub> layered semiconductor originated from electrically active native deep level defects <b>Mirhasan Yu. Seyidov, Faik A. Mikailzade, Talip Uzun, Andrei P. Odrinsky, Vafa B. Aliyeva, Tofiq G. Mammadov, Sardar S. Babayev</b>	3
2.	Effect of 2,4 kgray electron irradiation on electrical characteristics of the Au/P3HT/n-Si Schottky diode <b>A. Asimov, A. Kirsoy</b>	15
3.	Neutrino-antineutrino pairs radiation by transversely polarized electrons in strongly magnetized medium <b>Rasmiyya E. Gasimova</b>	20
4.	Conformation properties of his1-ala2-ile3-tyr4-pro5-arg6-his7 molecule <b>G.D. Abbasova, E.Z. Aliyev</b>	24
5.	Dielectric relaxation in the BaTiO <sub>3</sub> particles-liquid crystal colloids <b>T.D. Ibragimov, A.R. Imamaliyev, E.A. Allahverdiyev, S.T. Azizov, O.A. Aliev, G.M. Bayramov</b>	31
6.	Optical spectra of amorphous selenium obtained under different conditions (part I) <b>N.Z. Jalilov</b>	34
7.	Electronic treatment of the water mediums by high-voltage nanosecond pulses <b>E.J. Gurbanov</b>	39
8.	Thermal capacity, Debye temperature and phase transitions in TlCoS <sub>2</sub> crystals <b>E.M. Kerimova, A.M. Abdullayev, M.A. Aldjanov, M.D. Nadjafzade, P.G. Ismaylova, A.B. Magerramov, A.K. Zamanova, G.M. Akhmedova</b>	42
9.	The peculiarity of C electric properties modified by argentine ions <b>V.I. Orbukh, N.N. Lebedeva, G.M. Eyvazova, B.G. Salamov</b>	44
10.	Optimization and characterization of semipolar MOVPE and HVPE growth (11-22) InGaN/ (In)GaN quantum well heterojunctions <b>S. Abdullayeva, G. Gahramanova, R. Jabbarov</b>	47



[www.physics.gov.az](http://www.physics.gov.az)